Power flow analysis and inverse source characterisation of an elastic fluid-filled cylindrical shell

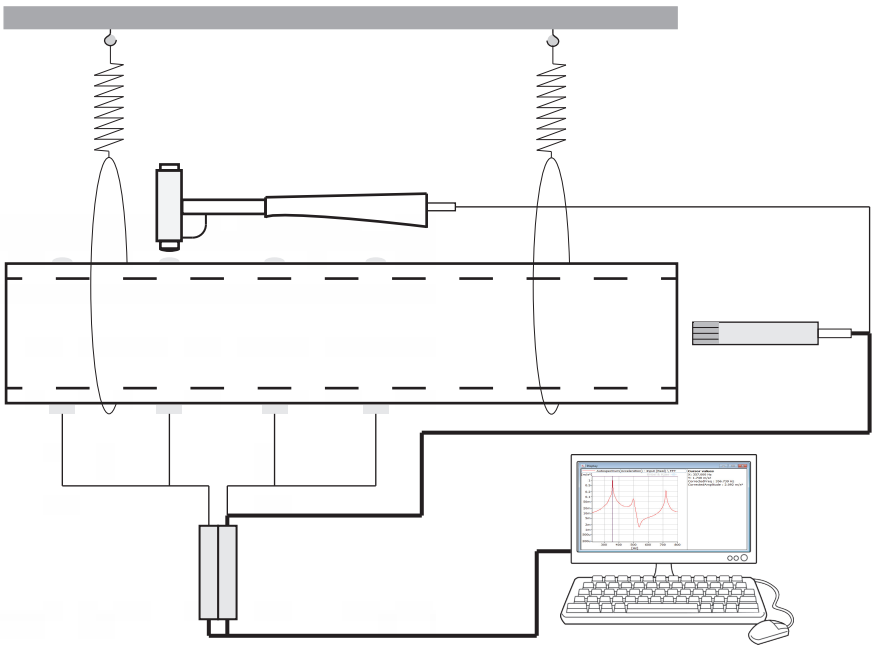

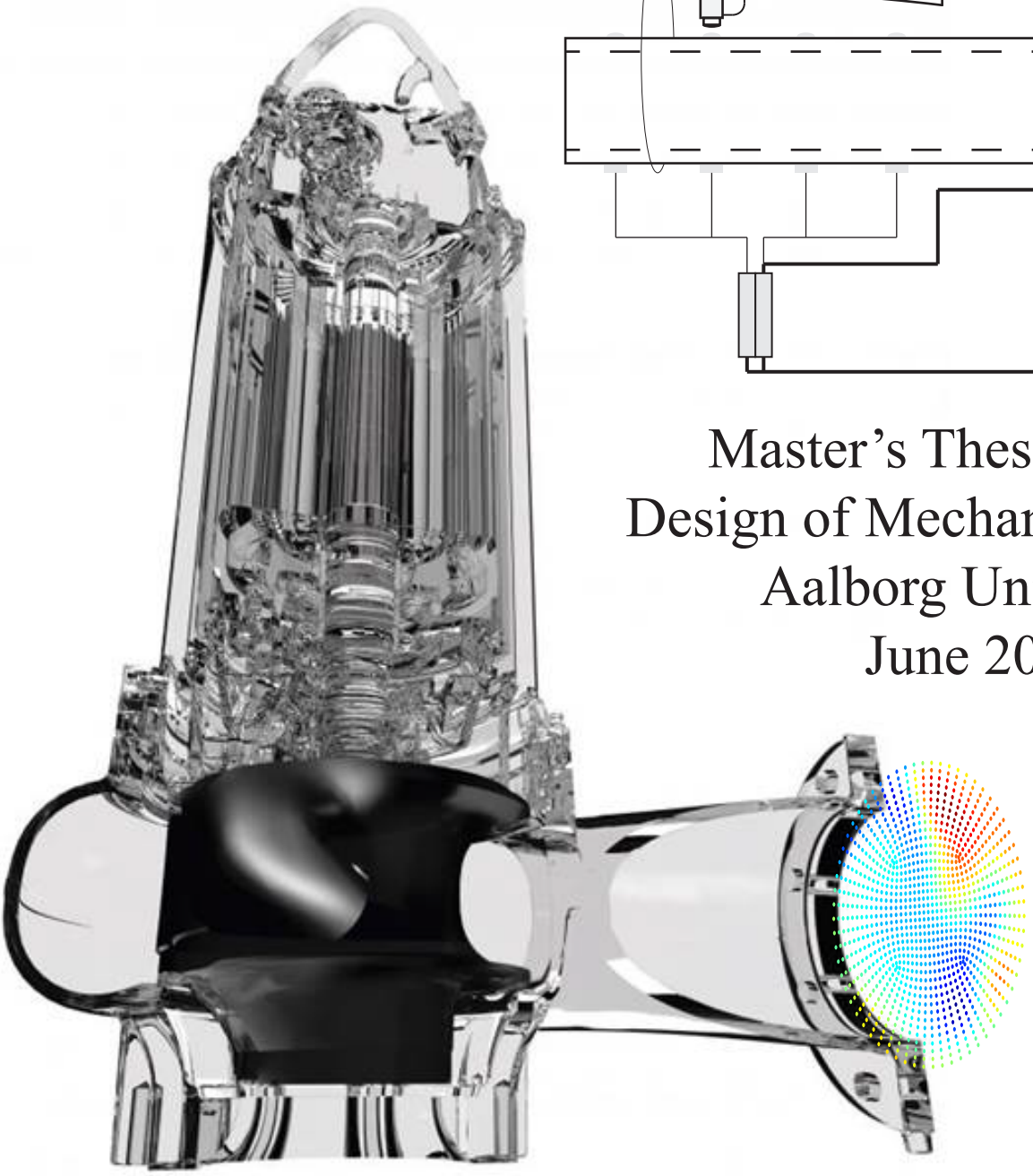

Master's Thesis - M.Sc.
Design of Mechanical Systems
Aalborg University
June 2015

GRUNDFOS®

Title:
Power flow analysis and inverse source characterisation of an elastic fluid-filled cylindrical shell

Semester:
Master's Thesis (MSc) in Design of Mechanical Systems

Project period:
02-02-2015 to 03-06-2015

ECTS:
30

Supervisor:
Sergey V. Sorokin

Project group:
DMS 2-209

Lasse Søgaard Ledet

Number printed: 3 pcs.
Number of pages: 80
Number of appendix: 4
Appendix CD

Frontpage reference:
www.temppress.com
Grundfos A/S

Department of Mechanical and Manufacturing Engineering
Fibigerstræde 16
DK - 9220 Aalborg Øst
Phone +45 99 40 71 17
info@m-tech.aau.dk
www.m-tech.aau.dk/

Synopsis:
This thesis can be considered as a continuation of the work done on 9th semester and in particular on the significant progress in the theory of cylindrical shells on the solution of the governing equations of the vibro-acoustic model derived here. The novelty of this method and the possibilities this has lead to are described and discussed in the paper, [Ledet et al., 2015], associated with this thesis. In addition to the 9th semester work the paper also includes a thorough convergence study and comparison to existing models used to validate and benchmark the method.
In the following the model is initially improved by means of convenient reformulations of equations, proposed methods for approximating roots and extension of the model to include both infinite and finite shells. Then the acoustic sources are derived from CFD-data provided by Grundfos and used in the vibro-acoustic model to analyse the waveguide performance. Subsequently, the model is validated through experiments conducted on finite pipes and the coherence between model and measured data is found to be good. In addition, observed issues related to modal decomposition and scaling between the model and experiments are investigated and discussed in detail. Finally, an inverse method is applied with the purpose of characterising the source by correcting the model according to the experiments.

Preface

This thesis is written at the *Department of Mechanical and Manufacturing Engineering* at *Aalborg University (AAU)* by *Lasse Søgaard Ledet* on the final semester of the master-program: *Design of Mechanical Systems (DMS)*. The thesis takes interest in the developments achieved through the authors 9^{th} semester project titled: *Power flow analysis of an elastic fluid-filled cylindrical shell* which was conducted in collaboration with the *Sound and Vibration centre* at *Grundfos A/S*.

The collaboration with Grundfos has been successfully continued through the thesis and in relation to this the author would like to acknowledge Grundfos for devoting their time, shelter and necessary remedies for conducting the desired experiments. Furthermore, the author would also like to personally acknowledge the contact persons at Grundfos; Senior Specialist *Jan Balle Larsen* and Test Engineer *Martin Mathiasen Lauridsen* for their indispensable help both in- and outside the lab, in discussions and for their devotion to the project.

In addition to this report the thesis also includes the conference paper, [Ledet et al., 2015], which outlines the governing equation and necessary theory for understanding this thesis. Further it includes a thorough description of the novelties derived on 9^{th} semester together with a verification and extensive convergence study of the method and finally a discussion including several interesting observations.

Further, the thesis includes an appendix compendium separated from the thesis itself in favor of the reader as several chapters involve extended discussions in appendix which are usually convenient to study in parallel. This compendium also includes an appendix CD where the reader can find i.a. Ansys animations of modeshapes, data sheets for components used throughout the experiments, documentation from the experiments etc. For a complete overview of the content on the CD see the outline in appendix A.

Formal guideline
In this thesis the references follow the Harvard-style thus in-line text references are given as [Ledet et al., 2015], where et al. indicates more than two authors. The complete reference is listed in the bibliography in the following sequence: author, title, publisher, ISBN/article number (if any) and year.

Internal references to chapters, sections, figures, equations and tables are numbered according to the chapters in which they are placed e.g. section/figure/table 4.2 and equations in brackets e.g. equation (4.2). Appendix references are given with capital letters e.g. appendix B.1.

Abstract

Vibrationer og støjemission fra rørsystemer er i mange industrier en realitet, og det er ofte en realitet, som ikke kan negligeres. Eksempelvis anses dette ved Grundfos for at være et af de største problemer indenfor pumpedesign, mens det samtidig er et af de områder, som optager mest tid. For virksomheder som Grundfos, der producerer high-end produkter, hvor kvalitet udgør en central del af virksomhedens værdikæde, er reduktion af vibrationer og hørbar støj en essentiel del i udviklingen af virksomhedens produkter. Foruden de umiddelbare gener forbundet med strukturelle og akustiske vibrationer, forekommer gener som udmattelse også hyppigt i systemer med ukontrollerede vibrationer. Grundet trykpulsationerne, som opstår ved pumpning af blandt andet spildevand, hvor pumpens løber, af åbenlyse årsager, ofte kun har en skovl, er disse trykpulsationer voldsomme og medfører i de fleste tilfælde kavitation af højere eller lavere grad. For at minimere disse pulsationer, er det således nødvendigt at opsætte en detaljeret model for bølgeudbredelsen, så man kan analysere waveguide-egenskaberne i sådanne rør. Dette definerer således det overordnede formål med denne thesis, nemlig at opsætte en detaljeret model, der inkluderer de koblede effekter mellem det akustiske og det strukturelle domæne, der er at betragte som de mest essentielle for rørsystemer, der transporterer et akustisk medie.

I denne thesis tages der udgangspunkt i den vibro-akustiske model, som er udledt på 9. semester. Denne metode benytter de netop udledte bi-ortogonalitetsligninger som betingelser til at løse ligningssystemet i modellen analytisk, således løsningen kan udtrykkes gennem en simpel, elegant eksplicit formel og altså ikke som en numerisk løsning til et koblet ligningssystem. Dette anses for at være et stort fremskridt indenfor den klassiske teori vedrørende elastiske væskefyldte cylindriske skaller, som således muliggør en lang række nye tiltag og undersøgelser for rørsystemer.

Formålet med denne thesis er således indledningsvis at benchmarke denne metode op mod eksisterende metoder, mens det ligeledes valideres gennem en konvergens analyse, så metodens evidens sikres. Metoden, samt de tilhørende evidensundersøgelser med mere, er dokumenteret i den medfølgende artikel. I den videre del af denne thesis udbedres modellen indledningsvist, herunder med udvidelse til at inkludere arbitrære akustiske og strukturelle kilder. Ligeledes udvides det resterende ligningssystem til at inkludere cylindriske skaller med finite længder foruden de infinite skaller, som den klassiske teori begrænses af. Dette gøres ved at benytte de hertil udledte Boundary Integral Equations. Ydermere undersøges forskellige approksimationer til rødderne af de såkaldte dispersion curves, og power flow ligningerne for fluid-delen omformuleres således intergalet udtrykkes via en summation af Lommel integraler, som derved substitueres med deres respektive analytiske ækvivalenter.

Efterfølgende udledes de akustiske kilder fra CFD-dataen, udleveret af Grundfos, ved at dekomponere dataene i dens indeholdte frekvenser og modes, således disse matcher antagelserne fra modellen. Med udgangspunkt i foregående dekomponering, kan den vibro-akutsiske waveguide performance analyseres og vurderes på baggrund af den energiudveksling, der forekommer mellem de forskellige transmissionsveje i nærheden af kilden, og ligeledes på

baggrund af den energi som udbredes gennem røret. Dernæst foretages der forsøg på to forskellige rør med finite længder uden væske, så modellen kan valideres i forhold til de eksperimentelle resultater. Her indledes der med en beskrivelse af forsøgene, hvilket efterfølges af en præsentation af forsøgsdataene. Afslutningsvis dekomponeres dataene med udgangspunkt i metoden benyttet for CFD-dataene, og det dekomponerede modalrespons sammenholdes således med modellen. Gennem denne sammenligning er der opnået yderst tilfredsstillende overensstemmelse mellem model og forsøgsdata. Afslutningsvis diskuteres forskellige problemstillinger observeret gennem dekomponering af både de eksperimentelle samt CFD-dataene.

Som afslutning på den undersøgende del af denne thesis, introduceres en invers metode til kildekarakterisering. Denne metode bygger på at korrigere modellen i sammenhold med forsøgsdataene, således det er muligt at bestemme kildens form, intensitet og placering i rørsystemet. Formålet er her at påvise metoden, som senere kan generaliseres til mere komplekse kilder og systemer, hvilket for eksempel kan være når væske introduceres og føres gennem røret via en pumpe.

I den afsluttende del af denne thesis konkluderes der indledningsvis på indhold i forhold til de opstillede problemer, hvorefter der perspektiveres til enkelte af de muligheder, denne model åbner for ved at introducere bi-ortogonalitetsbetingelserne i løsningen af de styrende ligninger.

Contents

1 Introduction

In many industries around the world piping systems of various types, dimensions and complexity are seen and e.g. in the oil and gas industry figure 1.1 greatly illustrates the complexity of a piping system transporting gas, oil, cooling water etc. around the facility. In addition figure 1.2 illustrates a simple but extensive straight pipeline transporting petroleum across large distances in the northern part of US.

Figure 1.1. Complex piping system in the oil and gas industry, [Omaspec Global Ltd., 2015].

Figure 1.2. Pipeline transporting petroleum in the northern part of US, [Huffington Post, 2015].

As can be imagined breakdown or leakage in such piping systems may have fatal consequences for personal, production, environment and the company's turnover etc. Thus it is essential to ensure high reliability by a proper static strength but even more pronounced by a proper dynamic strength in systems conveying an acoustic medium at either high/low pressure and/or high/low volumetric flow.

When conveying an acoustic medium, typically heavy fluids such as water, oil, waste water etc., dynamic loadings in terms of structural and acoustical vibrations will occur in the piping system due to the presence of pulsations caused by viscosity, turbulence or cavitation. This is typically seen as vigorously vibrating pipes and/or pulsations in the acoustic medium but can also be perceived as extensive audible noise as part of the vibration energy is radiated from the piping system as sound.

For the structural vibrations it may be obvious that these contribute to both the fatigue properties of the pipe and the sound emission. The acoustic vibrations in terms of pressure and velocity pulsations may on the other hand seem more remote from both the fatigue properties and sound emission. However, when large pulsations are present in the pressure and flow cavitation are introduced, meaning that when the pressure drops, air bubbles (or cavities) are created in the acoustic medium and when the pressure increases again the bubbles implode. During the bubble implosion unintentional loadings occur on the pipe wall and causes erosion and possible corrosion on the inner shell wall. Furthermore it contributes to additional

structural vibrations and extensive noise issues in the collapse of a cavity.

In many industries the audible noise radiated from the structure is of equally high interest e.g. in high-end products where quality is an essential part of the company's vision. Among companies providing high-end products in the piping and pumping industry is the collaborator Grundfos A/S who are considered one of the leading companies within the field of high quality pumps and complete pumping solutions. Grundfos' vision is to provide the best solutions within the field and they are therefore keen to resolve the aforementioned problems. Thus it is of highest interest to reduce both structural vibrations to improve the fatigue durability but likewise to reduce the sound radiated from fluid conveying systems to cope with the customers expectations to high quality products. With this in mind the ambitious scope for Grundfos is to:

Design a revolutionary pulsation dampener to reduce the pressure pulsations originating from pumping heavy fluid e.g. waste water, sewage etc. such that the remaining pulsations does not affect the piping system in which it is installed.

The scope originates from several cases where unfortunate installation of the piping system has lead to aggravated vibrations in the system terminating in fatigue failure or excessive noise. This lead to customers questioning the integrity of the pump despite the actual problem is found in poor installation such as poor utilisation of the surrounding suppressors or poor attachments to solid structures. In this case the waveguide properties of the complete piping system is jeopardized and even weakly pulsations may resonate in the system. Thus it is desirable to suppress the pulsations such that piping system is unaffected independent of the installation.

To achieve this a detailed model that predicts the vibrations and wave propagation in such piping systems is needed to fully understand the waveguide properties of the existing pipes and further to evaluate the response of the pipe when attached to an operating pump. As briefly discussed many aspects affect the wave propagation and vibrations in these piping systems and e.g. to describe the complete behaviour of the acoustic medium the model needs to account for viscosity effects causing decreased velocity at the pipe wall and cavitation caused by pressure drops. This leads, under certain conditions, to a turbulent flow in the boundary layer which reduce the sound speed in the fluid. Effectively, the model may also need to include the effects of a boundary layer encapsulating the aforementioned phenomenons. Likewise the model should enclose the static pressure and mean flow through the pipe and furthermore the compressibility of the fluid.

For the pipe wall the deformation pattern needs to be incorporated and likewise any pretension or residual stresses in the pipe. This also includes an advanced formulation of the constitutive properties of the pipe accounting for the effects of brittle/ductile material and different yield strength properties etc. Furthermore the piping systems are usually not straight and infinite, why bends and composed pipe segments may also be important for the analysis.

Finally, what is considered the most essential part is not the detailed individual properties of the structural nor of the acoustical domain but rather the interaction and exchange of energy between the two domains. This leads us towards this thesis' scope and limitations to achieve useful results within the given time frame of the project.

1.1 Thesis scope and limitations

In the project proposal from Grundfos the focus is confined to pumps used for sewage, waste water etc. which allows for reduced complexity in relation to the model parameters discussed previously. The initial scope of the project consist of three interconnected tasks:

1) Derive a vibro-acoutic model that accounts for the energy exchange between the structural and acoustical domain i.e. a fully coupled model is necessary.

This immediately suggest an analytical model in the sense of the classical time-harmonic forced vibration approach for elastic fluid-filled cylindrical shells considered as multi-modal waveguides carrying infinitely many waves. The vibro-acoustic model facilitated throughout the thesis is presented in the associated paper, [Ledet et al., 2015], and is based on Novozhilov Gol'denveiser's thin shell theory. In this model only the most essential waveguide properties are included as the aforementioned phenomenons affecting the waveguide properties can be neglected for the pumps considered in this thesis due to a generally low pressure and flow. Thus the fluid is considered as an inviscid compressible fluid with no mean flow and the pipe as an elastic homogeneous thin shell. The fluid-structure interaction is incorporated as a velocity continuity between the radial components at the fluid-structure interface where the interface is referred to the undeformed geometry i.e. small deformations are assumed.

From this approach it is immediately possible to analyse the waveguide properties in terms of cut-on of the energy carrying waves (propagating) and energy conversion waves (decaying and attenuating) and moreover analyse the far field power flow and exchange of energy between the different transmission path in the near field.

2) Validate the model through experiments.

To obtain high quality measurements from experiments it is advantageous to conduct experiments without fluid and for finite pipes to significantly reduce the sources of error related to cavities in the fluid, anechoic terminations in experimental set-ups etc. Consequently, the theory of the classical vibro-acoustic model needs to be further improved by extending it to the finite domain by means of the Boundary Integral Equation Method (BIEM). Furthermore testing of different pipes with different thickness-to-radii ratio are relevant to extend the validity range of the model. Finally, to ensure the validity of the fluid-filled shell this is studied mathematically in [Ledet et al., 2015].

3) Derive acoustic sources from CFD output data provided by Grundfos and analyse the vibro-acoustic performance of the pipe when subjected to the derived acoustic sources.

The provided CFD-data is derived from CFD analysis of Grundfos' newest prototype-pump called S-tube. The S-tube is a 75kW waste water pump with an outlet radii of $75mm$, an estimated nominal static pressure of 6.5 bar and a volumetric flow of $350\frac{\mathrm{m}^3}{\mathrm{h}}$ corresponding to a mean velocity of approximately $5.5\frac{\mathrm{m}}{\mathrm{s}}$.

The acoustic sources can be deduced by modal decomposition of the time varying CFD-data from which the vibro-acoustic performance is available if the derived acoustic sources are

applied in the model. Through the classical approach arbitrary sources are analysed by a time consuming convolution integral, however, due to the recent advances described in [Ledet et al., 2015] the convolution can be implemented in the governing equation and the associated amplitudes calculated directly.

In extension to the milestones proposed by Grundfos and due to the initial work done on 9^{th} semester it has been decided in collaboration with Grundfos to extent the work and also consider:

5) Validation of the novelties derived for solving the equation system of the vibro-acoustic model analytically i.e. validation by a convergence study and benchmarking against existing models.

As the experiments are confined to only consider finite hollow shells it is necessary to validate and benchmark the proposed method from 9^{th} semester against existing models including heavy fluid to ensure that the method does not contain pitfalls or typos in the program which makes the model deviate from the conventional method. Further the new method is validated outside the range to which the conventional method is confined and therefore its validity should be studied through a convergence study.

6) Source characterisation based on correcting the vibro-acoustic model according to the experimental data i.e. Inverse Source Characterisation (ISC).

For experiments in acoustics one of the major issues in the comparison between model and measured data is that when the acoustic medium is excited it is strictly speaking impossible to accurately predict the characteristics of the applied source i.e. shape, intensity and in some cases the location. In these experiments the typical source is a hydrophone used in reverse mode and even though the intensity and source distribution is known by this source it is still with some uncertainties. This can obviously be considered a significant source of error in the comparison between experiments and model.

The idea of the ISC is in this thesis a prove-of-concept to investigate if it is possible by inverse methods and experimental data to accurately predict the source characteristics in the experiments. If this is possible we are optimistic that this will also be possible for acoustical sources as well and in that case significant advance in the area of acoustic source characterisation for cylindrical shells is achieved. Notice here that the possibility of applying inverse techniques for source characterisation is only possible due to the novelties presented in the associated paper, [Ledet et al., 2015].

1.2 Thesis outline

In the conference paper, [Ledet et al., 2015], the governing equations for the vibro-acoustic model are presented followed by a detailed derivation of the novelties developed on 9^{th} semester. These novelties are supported by an extensive convergence study and benchmarking against the conventional method to validate the novelties. Finally, the paper is concluded by a study of the differences between a velocity and pressure source in the acoustic field.
If the reader is not familiar with bi-orthogonality conditions or wave propagation and power

flow in infinite fluid-filled elastic cylindrical shells it is **strongly recommended** to read the paper before continuing with this part of the thesis.

In chapter 2 the aforementioned improvements necessary to accommodate with the scope of the thesis are collected. Thus this chapter can be considered as a theoretical chapter including independent sections of expanded theory and advanced improvements to the classical cylindrical shell theory of multi-modal waveguides.

In chapter 3 the CFD-data for the S-tube is presented and the acoustical sources deduced from the data by means of decomposition; first from the time domain into the frequency domain and successively further into each circumferential wave-number represented as a continuous acoustic source distributed in the radii. This procedure is known as modal decomposition. Subsequently, the acoustical sources derived from the CFD-data are applied in the vibro-acoustic model as arbitrary sources and the vibro-acoustic performance of the waveguide is assessed when subjected to the sources present in Grundfos' S-tube pump operating at nominal load when represented by CFD-data.

In chapter 4 the model is validated through experiments. Initially, the set-up is briefly presented, followed by a presentation of the results obtained through the experiments here including the measured response and the observed resonance frequencies. Successively the material parameters are deduced from the results by inverse methods and further the data is decomposed following the same mathematical procedure used in the decomposition of the CFD-data. Subsequently the model and experimental data is compared to verify the coherence and finally the issues observed in the comparison are discussed thoroughly and investigated further through a toy case.

In chapter 5 the idea of inverse source characterisation is outlined with respect to its practical application and the formulation of the inverse optimisation algorithm is introduced. Subsequently, the different parameters affecting the quality of the source characterisation is discussed together with the sensitivities related to the initial guess. Unfortunately, several issues addressed in previous chapters has confined the possibilities for conducting inverse optimisation at this point and instead a method that circumvent this is proposed. The method is based on solving the inverse problem through a case study where complexity is added gradually and consequently experiments are redundant in relation to the prove of concept approach taken in this thesis.

In chapter 6 and 7 the thesis is concluded with respect to the project proposal suggested by Grundfos and likewise with respect to the authors personal expectations. Finally, the succeeding chapter contains a discussion regarding possible future work all made possible by application of the bi-orthogonality conditions for solving the governing equations such that the accuracy of the conducted analysis are increased significantly.

Improvements to the vibro-acoustic model 2

In the interest of conducting a detailed power flow analysis, inverse source characterisation and eventually optimisation all including a significant number of waves, the performance of the vibro-acoustic model is essential to its success. This chapter is thereby devoted to improvements and further developments with the scope of improving the efficiency and extend the area of application of the vibro-acoustic model presented in the associated paper, [Ledet et al., 2015]. Consequently, this section can be viewed as a theoretical chapter including independent sections of expanded theory and improvements.

To be consistent this chapter is also based on the data used throughout the paper i.e. a steel pipe including water. The material and geometry can be found in table 2.1.

Name	Decription	Value	Unit
Material data			
ν	Poisson's ratio	0.3	-
E	Young's modulus	210	GPa
ρ_{str}	Shell density	7800	kg/m^3
ρ_{fl}	Fluid density	1000	kg/m^3
c_{str}	Structural sound speed	2.308e08	m/s
c_{fl}	Fluid sound speed	1440	m/s
Geometry			
R	Shell radius	20	mm
h	Shell thickness	0.35	mm

Table 2.1. Material data and geometry used in [Ledet et al., 2015] and throughout this chapter.

In relation to improving the computational efficiency of the vibro-acoustic model one of the primary interests is to improve the root-finding of the dispersion equation to cope with the demands for inverse source characterisation and optimisation. Finding the roots is not only a challenging task but also very time consuming and unfortunately they must be found in each iteration as the dispersion of the roots change with changing physical parameters. To clarify and avoid confusion we refer, in the following, to roots of the dispersion equation rather than to the axial wave-numbers, however, they are essentially identical.

2.1 Calculating the dispersion curves

With the interest of applying the model for inverse source characterisation and for general optimisation tasks it is crucial that the model is computationally efficient such that we can extract results within a reasonable time frame. Significant improvements to the model have

already been implemented through the novelties presented in [Ledet et al., 2015], however, in this case the physical parameters are considered invariant and the roots of the dispersion equation are therefore only to be calculated once to conduct the necessary analysis. For optimisation purposes the physical parameters might change in each iteration and consequently the dispersion of the roots change accordingly. Now, as calculating the dispersion curves governs approximately 90-95% of the computational time when the novelties are implemented it is essential to derive an alternative fast method/solution for calculating the dispersion curves.

To find this alternative method the dispersion equation has been thoroughly examined to withdraw knowledge regarding the root dispersion. This has lead to a comprehensive study which is fully documented in appendix B. In this section we therefore only present the most essential conclusions of the investigation.

2.1.1 Introduction to the dispersion equation(s)

The formulation of the dispersion equation is treated in many references e.g. [Sorokin and Terentiev, 2006; Sorokin et al., 2004; Novozhilov, 1959; Fuller and Fahy, 1982; Pavić, 1990] and particularly for the Novozhilov-Gol'denveiser theory for thin shells used in this thesis, the references [Sorokin and Terentiev, 2006; Sorokin et al., 2004; Novozhilov, 1959] treats this specific theory in detail. However, a brief description of the governing equations and solution ansatz can be found in the associated paper [Ledet et al., 2015]. Based on the latter references it is evident that the dispersion equation is given as the characteristic equation of the linear system of equations as shown in equation (2.1).

$$d_{11}d_{22}d_{33} + d_{13}^2 d_{22} + d_{12}^2 d_{33} - d_{23}^2 d_{11} - d_{12}d_{23}d_{13} - d_{13}d_{12}d_{23} = 0 \tag{2.1}$$

where the entries, d_{ij}, of the system matrix can be found in e.g. [Sorokin et al., 2004] or in equation (B.1) of appendix B.1.1.

By substitution of d_{ij} into equation (2.1) the dispersion equation can conveniently be split into terms including the Bessel-functions and the remaining terms.

$$f_2(m,k,\Omega) - f_1(m,k,\Omega)\frac{\tilde{\rho}\Omega^2 R}{h} J_m(\kappa)\left[\frac{\mathrm{d}J_m(\kappa)}{\mathrm{d}\kappa}\kappa\right]^{-1} = 0 \tag{2.2}$$

where m, k and κ are the circumferential, axial and radial wave-numbers, J_m is the m^{th} order Bessel-function of first kind, f_1 and f_2 are functions of m, k, Ω and are respectively second and fourth order polynomials in k^2. The definitions of the non-dimensional partameters Ω, $\tilde{\rho}$ etc. are found in equation (B.2) in appendix B.1.1.

This formulation of the dispersion equation does unfortunately hold periodic poles at the zeros of the derivative of the Bessel-function and effectively it forms a sever discontinuous/singular function. To prevent this the dispersion equation can be modified as

$$f_2(m,k,\Omega)\kappa\frac{\mathrm{d}J_m(\kappa)}{\mathrm{d}\kappa} - f_1(m,k,\Omega)\frac{\tilde{\rho}\Omega^2 R}{h} J_m(\kappa) = 0 \tag{2.3}$$

and since the functions f_1 and f_2 does not contain any polynomial fractions this modified formulation of the dispersion equation is continuous in the real domain, $\mathbb{R}$.

To distinguish the two formulations for future reference the original dispersion equation of (2.2) is referred to as the *original dispersion equation* while the re-formulation of (2.3) is referred to as the *modified dispersion equation*.

2.1.2 Introduction to the problem

To introduce the issues that makes the convergence rate and the convergence of the roots a challenging problem the distribution of the roots in the two formulations of the dispersion equation are investigated to extract general knowledge which can lead to possible solutions for improving convergence and convergence rate for calculating the dispersion curves. This investigation is presented and elaborated in appendix B.1.1, thus only the most essential observations are outlined in the following.

The dispersion of waves in an elastic waveguide contains three types of waves; propagating, decaying and attenuating waves as illustrated in figure 2.1.

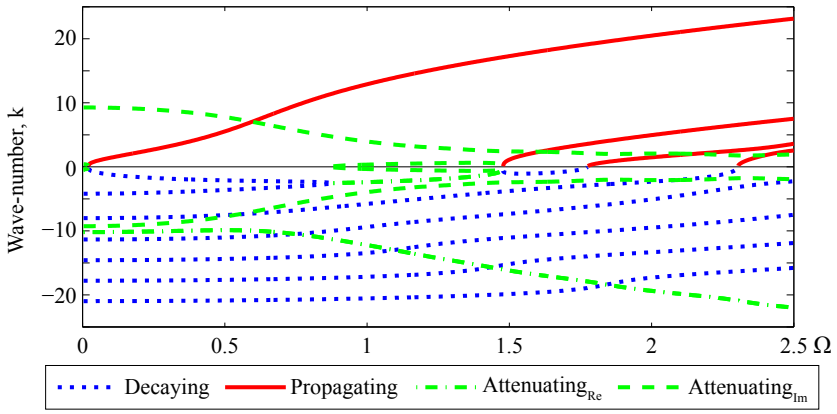

Figure 2.1. Dispersion curve for $m = 3$ and the parameters of table 2.1. The blue ··· are decaying waves (real roots), the green – – and – · – are attenuating waves (complex roots) and the red – are propagating waves (purely imaginary).

For elastic waveguides the energy carrying waves are the propagating waves, corresponding the purely imaginary roots of the dispersion equation whereas the decaying (real roots) and attenuating waves (complex roots) satisfy the decay conditions and does therefore vanish in time. The latter decaying wave types does thereby not contribute to the energy transportation but does nevertheless contribute to the energy exchange that appears in the vicinity of the source between the acoustic and structural domains. In this case the span of the term vicinity is determined by the frequency and physical parameters.

The issues related to the dispersion of the waves shown in figure 2.1 for infinite fluid-loaded pipes is that due to the presence of the fluid the dispersion equation is rather involved and the roots are difficult and computationally expensive to find.

Through this investigation of the distribution of the roots it is found that the real roots oscillate and are governed by the derivative of the Bessel-function. Further the investigation shows that the real roots are more pronounced in the modified dispersion equation as the poles and zeros in the original dispersion equation collide for increasing wave-numbers and in the presence of this singularity it is strictly speaking impossible to solve numerically for the roots. This can be illustrated by considering the two formulations of the dispersion equation when $\Omega \to 0$.

$$\text{Original:} \quad f_2(m,k,\Omega \to 0) - f_1(m,k,\Omega \to 0)\frac{\tilde{\rho}(\Omega \to 0)^2 R}{h} J_m(k) \left[\frac{\mathrm{d}J_m(k)}{\mathrm{d}k} k\right]^{-1} = \ldots$$

$$\ldots = f_2(m,k,\Omega \to 0) = 0$$

$$\text{Modified:} \quad f_2(m,k,\Omega \to 0) k \frac{\mathrm{d}J_m(k)}{\mathrm{d}k} = 0$$

From the latter equation it is clear that due to the singularities in the original dispersion equation it is difficult to capture the acoustic roots of the Bessel-function at low frequencies.

This collision of the zeros and poles suggest, however, that the asymptotic roots of the dispersion equation will converge to the zeros of the derivative of the Bessel-function which corresponds to the dispersion of waves in an acoustic duct. Physically, this implies that the higher order acoustic waves sees the slow vibrating shell as completely rigid, meaning that the large decay rate of the acoustic waves does not interact with the shells vibration pattern.

For the complex and purely imaginary roots the investigation does not point towards a specific distribution pattern as for the real roots. Nonetheless it is found that for increasing frequency the purely imaginary roots converge to the purely imaginary roots of f_2. Further it is proven that for complex roots there is a finite number of roots as the oscillating Bessel-function does not contain complex roots itself. Finally, the investigation of the complex and imaginary roots suggests that the original dispersion equation should be used in solving these roots as the complex zeros and poles are not colliding and they are therefore not affected by the singularities. Notice further that the original dispersion equation is better scaled than the modified dispersion equation and the complex roots are therefore more pronounced in the original equation.

2.1.3 Approximations to roots of the dispersion equation

As formally stated the root-finding confines the possibility of inverse source characterisation and optimisation in general, why the motivation for improving the computational time spend here is high. Furthermore a bunch of the roots tend to be "hidden" in the dispersion equation depending on the formulation as discussed in the previous section. Thus besides the issue of convergence rate, the convergence of specific roots themselves are also a major issue in wave theory. This section does thereby contain a first, slightly naive approach namely to derive approximations for the roots of the dispersion equation.

The area of calculating/approximating the roots of such elastic waveguides is besides in engineering also a major issue in applied physics and mathematics. In fact this constitute a major research area in many papers and in e.g. [Landau, 1999] ratios of Bessel-functions, similar to the ratio seen in the original dispersion equation, are investigated and further, with interest in this study, the solution to properly the simplest mixed cylindrical boundary value problem; $\alpha J_\nu(x) + xJ'_\nu(x) = 0$ is sought. In this paper an analytical solution to the "simple" boundary value problem is sought and in addition the author lists 10 additional papers including extensive studies of the exact same equation. Notice that this equation is similar to our modified dispersion equation, however for the fluid-loaded cylindrical elastic waveguide treated in this theses the governing equations are much more involved than that treated in [Landau, 1999].

This equation was then again treated in [Rawlins, 2011] here by successful application of the finite-product method developed in [Chapman and Sorokin, 2009]. This method builds on approximating the governing equation by means of a finite product formulation and approximations by Gamma-functions, which in the latter reference was validated for the classical Rayleigh-Lamb problem.

As mentioned this finite-product method was successfully applied in [Rawlins, 2011] to approximate the governing equation for the cylindrical boundary value problem also treated in [Landau, 1999]. However, as the finite-product method provides good approximations for the complete dispersion equation and not only the roots it would involve similar issues, singularities

etc. as discussed in the previous section for the original dispersion equation. It is therefore expected that the finite-product method does not ease the challenges in this thesis.

Thus since many papers in the past have treated the aforementioned, much simpler, cylindrical boundary value problem without drawing any final conclusions on how the root-finding is eased by these methods or on how the roots can be approximated, our approach regarding approximating the roots of the much more involved boundary value problem can be considered as slightly naive. Nonetheless it was possible to derive a successful method for approximating the real roots.

The investigation of possible approximations of the roots and the related aspects are documented in detail in appendix B.1.2 and for an elaborated discussion on the subject this appendix should be attended. In this section only the most essential finding are presented.

For the real roots two valid approximation methods are proposed. The first method is simple and is based on the knowledge obtained in section 2.1.2 regarding the collision of zeros and poles. Thus the asymptotic (real) roots can be approximated as the zeros of the derivative of the Bessel-function, $j'_{m,n}$, corrected such that; $\tilde{k}_n = \sqrt{(j'_{m,n})^2 - \tilde{\gamma}^2\Omega^2}$.

The second method is on the other hand based on the idea of estimating the roots through a linear combination of the individual roots of the Bessel-functions as shown in equation (2.5). The nature of this idea originates from the fact that the real roots are governed by the Bessel-function which then implies that the actual "repeated" roots of the dispersion equation must distribute in-between the roots of these Bessel-functions. Thus only one root will be present between the Bessel-zeros.

$$\tilde{k}_n = w_{2n} j'_{m,n} + w_{1n} j_{m,n} \tag{2.5}$$

where $j_{m,n}$ and $j'_{m,n}$ are the zeros of the Bessel-functions, w_{1n} and w_{2n} the weighting functions for the n^{th} zero and $\tilde{k_n}$ the approximated root.

The weighting functions in the latter equation are based on the function values at the zeros of the Bessel-functions as illustrated in figure 2.2 and the mathematical formulation are presented in equation (B.6) in appendix B.1.2.

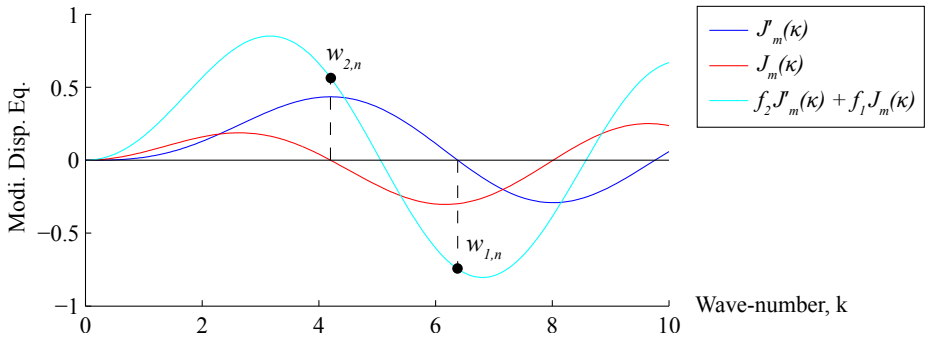

Figure 2.2. Sketch illustrating the idea for calculating the weighting-functions by means of the function values at the Bessel-zeros. The blue graph represent the derivative of the Bessel-function while the red represent the Bessel-function itself and the cyan the dispersion equation.

To validate the quality if the approximations the results from the two methods are presented in figure 2.3 together with the authentic roots solved for in the modified dispersion equation by a standard commercial search algorithm.

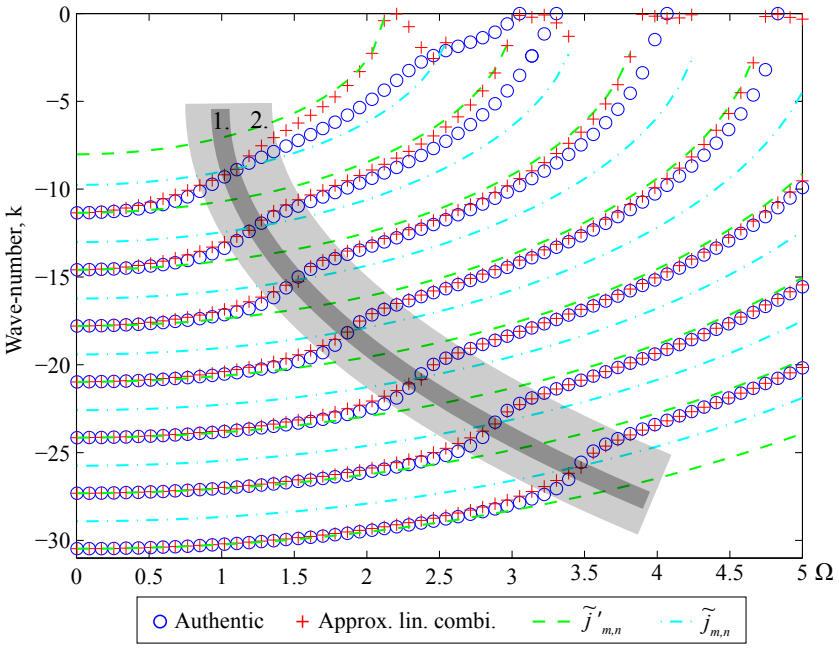

Figure 2.3. Dispersion of real roots at $m = 3$. o indicates the authentic roots of the dispersion equation, + the approximation by a linear combination of the Bessel-zeros while – – and –· are the corrected Bessel-zeros of the derivative and the Bessel-function itself, respectively.

From the latter figure it is seen that the simple approximation by the corrected zeros of the derivative of the Bessel-function is acceptable at higher order wave-numbers and at higher frequencies. Notice however, that each root passes through a phase illustrated by region 2 in the figure where the roots drop from one zero of the Bessel-function to one of lower order. Nevertheless, this transition is not captured by simple approximation, however, by the linear combination approach this transition is fully captured and with an excellent accuracy.

As illustrated in region 1 of figure 2.3 each wave satisfy the pressure release boundary condition at a specific frequency. This corresponds to the fluid vibrating in perfect phase with the shell causing larger amplitudes than for the out-of-phase wave-numbers. This is an interesting observation that may lead to an increased understanding of the coupling between the fluid and structure if investigated further. This is nonetheless found out of scope in the present thesis, however in comparison with the governing equations it can be concluded that these roots are structure originated.

Thus based on the evidence shown in the figure and the extended discussion in appendix B.1.2 it can be concluded that the linear combination for approximating the higher order real roots is indeed very good. Furthermore, as it is based on the simple fact that only one roots will be present between the zeros of the two Bessel-functions this method is indeed considered as a sustainable method for approximating the real roots and also for the case when the roots distribute more freely between the zeros of the Bessel-function and its derivative as seen in region 2 in figure 2.3.

In conclusion it has been possible, despite the naive approach, to derive a sustainable approximation for the real roots. Nonetheless, it is still important, from the view point of inverse source characterisation and optimisation, to investigate how the complex roots and lower order real roots can be extracted from the dispersion equation in a computationally efficient way. This is treated in the following section.

2.1.4 Calculation of remaining roots

With inverse source characterisation and optimisation in mind the following investigation takes interest in improving the initial guesses for the complex and first few real roots such that the roots can be found in few iterations through a standard commercial search algorithm.

The most widely used method for retrieving initial guesses is, to the authors knowledge, based on approximating the dispersion equation by a Taylor series and apply the roots found in this approximation as the initial guesses in the actual dispersion equation. This method is however highly computationally time consuming and through this investigation, documented in appendix B.1.3, another and much more efficient method is proposed.

The alternative method to the latter is based on facilitating the roots found at previous frequencies, Ω, to approximate the initial guess at the present Ω. This is done simply by the linear extrapolation shown in equation (2.6).

$$\tilde{k}_n = \frac{\tilde{k}_{n-1} - \tilde{k}_{n-2}}{\Omega_{n-1} - \Omega_{n-2}} \Delta\Omega + \tilde{k}_{n-1} \tag{2.6}$$

This method reduces the number of trivial guesses significantly compared to the Taylor approach and with basis in the smooth and continuous distribution of the roots in the dispersion curves (seen in figure 2.1 for $m = 3$) this method will provide initial guesses so close to the authentic roots that convergence usually occur in 1 or 2 iterations.

Obviously, the quality of the initial guesses are confined by the frequency step size and whether the extrapolation procedure captures the domain shift ($\mathbb{R}$ and $\mathbb{C}$) e.g. in the transition where decaying waves transform into propagating waves etc. This can however be controlled by implementing simple transition-rules for the initial guesses as the transformation of waves is well-defined from certain physical aspects. Several of these transition-rules are in fact visible in figure 2.1 but are elaborated and thoroughly explained through figure B.7 in appendix B.1.3. Despite the good initial guesses the proposed method it not valid at arbitrary frequencies and thus has the disadvantages that it needs to start at $\Omega = 0$ as this is the only frequency at which the first set of initial guesses are available. Thus at first impression this method is not feasible as the complete dispersion curve need to be calculated from $\Omega = 0$ in each iteration. However, this can be improved by introducing corrections of the initial roots.

While the latter method improves the root-finding significantly compared to the conventional approach by a Taylor approximation it is still possible to incorporate further improvements. Based on the knowledge gained through the latter investigations of the dispersion equation and due to the high quality of the initial guesses, it is sufficient to correct the initial guesses by the simple Newton-Raphson scheme shown in (2.7) to get the desired accuracy of the roots.

$$\tilde{k}_n = \tilde{k}_{n-1} - \frac{f(\tilde{k}_{n-1})}{f'(\tilde{k}_{n-1})} \tag{2.7}$$

where f and f' in this case represent the dispersion equation and its derivative.

This is indeed convenient from an optimisation view point as the roots only need to be calculated for the initial physical parameters and in the following iterations the existing roots are corrected by the simple Newton-Raphson scheme.

2.1.5 Summary

Thus in summary the complex roots and the first 2-3 real roots are calculated by correcting the initial guesses (found from extrapolation of previous roots) with a Newton-Raphson scheme. The remaining real roots up to the desired number are approximated by the linear combination approach. This is done for the initial physical parameters, in the frequency spectrum of practical interest and with the desired frequency resolution.

In case of inverse source characterisation or optimisation the initial roots are simply corrected in each iteration by the simple Newton-Raphson scheme which will provide acceptable approximations for the roots provided that the changes in the physical parameters in each iteration are sufficiently small. Thus the proposed combination of methods provide a computationally efficient method for calculating and correcting the roots and it is indeed sufficient for optimisation and inverse source characterisation as the correction is based on function evaluations.

2.2 Reformulation of the fluid power flow equation

When calculating the power flow for a given load the evaluation of the fluid power flow is a rather time consuming process as we need to use numerical integration to evaluate it. This contains two immediate downsides; 1) Varying numerical accuracy on the different numerical integrators might cause a slightly oscillating power balance and in combination with approximated roots the oscillations might make us question the validity of the vibro-acoustic model. 2) Numerical integration are in most commercial software only done with all variables included in the integral which is problematic when the fluid power flow is integrated across r while x is kept variable. Alternatively, we can discretise the problem in either r, x or both and use a simple (or advanced) integration rule e.g. trapezoidal, Simpsons 3/8 etc. On the other hand when analysing intense loads such as the delta-function the resolution in r needs to be extremely high for these integration rules to fully capture the intensity of the load. This will increase the computational time significantly and if the discrete resolution is too low it might distort the picture of the energy distribution in the near field.

The purpose of this section is therefore to avoid these issues by reformulating the power flow equation such that it can be expressed analytically. The motivation for this reformulation originates from the fact that the integral in the fluid power flow contains a summation of Lommel integrals which holds an elegant analytical solution. The purpose is thus to divide the integral up such as to recognise the Lommel integrals and replace these by their analytical equivalents.

The definition of the power flow can be found in several references e.g. [Pavić, 1990; Fuller and Fahy, 1982] etc. and by following the latter notation the fluid power flow is expressed as

$$N_{fl} = \frac{1}{2}\Re\mathrm{e}\left(\int_0^{2\pi}\int_0^R p_m \bar{\vartheta}_m r \mathrm{d}r\mathrm{d}\theta\right) \tag{2.8}$$

where overline, $\bar{}$, indicate the complex conjugated and p_m and ϑ_m is the acoustic pressure and axial velocity at each circumferential wave-number.

The pressure and velocity is defined as

$$\begin{aligned} p_m &= \sum_{n=1}^{M} \rho_{fl} R\omega^2 C_m^{(n)} J_m(\kappa^{(n)} r) \left[\left. \frac{\mathrm{d}J_m(\kappa^{(n)} r)}{\mathrm{d}r} \right|_{r=1} \right]^{-1} \exp\left(\frac{k^{(n)}}{R} |x-\xi| \right) \\ \vartheta_m &= \sum_{n=1}^{M} -i\mathrm{sgn}(x-\xi) k^{(n)} \omega C_m^{(n)} J_m(\kappa^{(n)} r) \left[\left. \frac{\mathrm{d}J_m(\kappa^{(n)} r)}{\mathrm{d}r} \right|_{r=1} \right]^{-1} \exp\left(\frac{k^{(n)}}{R} |x-\xi| \right) \end{aligned} \tag{2.9}$$

where M is the number of waves included in the analysis and each summed term of p_m and ϑ_m belongs to either $\mathbb{R}$ or $\mathbb{C}$.

The pressure and velocity profiles can thus be conveniently represented on a general form i.e. as a summation of the product between two complex numbers as illustrated in equation (2.10).

$$p = \sum_{n=1}^{M} z_n^{\alpha} z_n^{\beta} \qquad\qquad \bar{\vartheta} = \sum_{j=1}^{M} \bar{z}_j^{\delta} \bar{z}_j^{\gamma} \tag{2.10}$$

where the complex numbers are distinguished by Greek letters.

The pressure and the conjugated velocity product is then written as

$$\begin{aligned} p\bar{\vartheta} = \sum_{n=1}^{M}\sum_{j=1}^{M} z_n^{\alpha} \bar{z}_j^{\delta} z_n^{\beta} \bar{z}_j^{\gamma} = & z_1^{\alpha} \bar{z}_1^{\delta} z_1^{\beta} \bar{z}_1^{\gamma} + z_1^{\alpha} \bar{z}_2^{\delta} z_1^{\beta} \bar{z}_2^{\gamma} + \ldots + z_1^{\alpha} \bar{z}_M^{\delta} z_1^{\beta} \bar{z}_M^{\gamma} \\ & z_2^{\alpha} \bar{z}_1^{\delta} z_2^{\beta} \bar{z}_1^{\gamma} + z_2^{\alpha} \bar{z}_2^{\delta} z_2^{\beta} \bar{z}_2^{\gamma} + \ldots + z_2^{\alpha} \bar{z}_M^{\delta} z_2^{\beta} \bar{z}_M^{\gamma} \\ & \vdots \\ & z_M^{\alpha} \bar{z}_1^{\delta} z_M^{\beta} \bar{z}_1^{\gamma} + z_M^{\alpha} \bar{z}_2^{\delta} z_M^{\beta} \bar{z}_2^{\gamma} + \ldots + z_M^{\alpha} \bar{z}_M^{\delta} z_M^{\beta} \bar{z}_M^{\gamma} \end{aligned} \tag{2.11}$$

And if the complex numbers are instead ordered in vectors as illustrated in (2.12).

$$\mathbf{z}^{\alpha} = \begin{bmatrix} z_1^{\alpha} \\ z_2^{\alpha} \\ \vdots \\ z_N^{\alpha} \end{bmatrix} \qquad \mathbf{z}^{\delta} = \begin{bmatrix} z_1^{\delta} \\ z_2^{\delta} \\ \vdots \\ z_N^{\delta} \end{bmatrix} \qquad \mathbf{z}^{\beta} = \begin{bmatrix} z_1^{\beta} \\ z_2^{\beta} \\ \vdots \\ z_N^{\beta} \end{bmatrix} \qquad \mathbf{z}^{\gamma} = \begin{bmatrix} z_1^{\gamma} \\ z_2^{\gamma} \\ \vdots \\ z_N^{\gamma} \end{bmatrix} \tag{2.12}$$

Then the product of equation (2.11) can be expressed as the sum of the diagonal in the following vector/matrix product

$$p\bar{\vartheta} = \sum \left[\left(\mathbf{z}^{\alpha} \bar{\mathbf{z}}^{\delta \mathbf{T}} \right) \left(\mathbf{z}^{\beta} \bar{\mathbf{z}}^{\gamma \mathbf{T}} \right) \right]_{\mathrm{diag}} \tag{2.13}$$

where each of the vector products $(\mathbf{z}^{\alpha} \bar{\mathbf{z}}^{\delta \mathbf{T}})$ holds conjugated symmetry, meaning that the lower part is symmetric with the upper part by the complex conjugated.

If the complex numbers of the pressure-velocity product in (2.11) are collected such that $\mathbf{z}^{\alpha}$ and $\mathbf{z}^{\delta}$ are the only ones including r-dependence then we can conveniently reformulate the fluid power flow to (2.14). In this case the power flow equation is collected such that $\mathbf{z}^{\alpha} = \mathbf{z}^{\delta} = J_m(\kappa r)$ and the remaining is collected in $\mathbf{z}^{\beta}$ and $\mathbf{z}^{\gamma}$.

$$N_{fl} = \gamma_m R^2 \frac{\pi}{2} \Re\mathrm{e} \left(\left[\left(\mathbf{z}^{\beta} \bar{\mathbf{z}}^{\gamma \mathbf{T}} \right)^{\mathbf{T}} \int_0^1 \left(\mathbf{z}^{\alpha} \bar{\mathbf{z}}^{\alpha \mathbf{T}} \right) r \mathrm{d}r \right]_{\mathrm{diag}} \right) \tag{2.14}$$

where the $\gamma_m\pi$ appears from the circumferential integral, hence $\gamma_{m=0} = 2$ and $\gamma_{m\neq 0} = 1$.

Now the integral is evaluated by introducing the r-dependence into $\mathbf{z}^\alpha$ and in addition to this we notice that the Bessel-function of first kind of any order is a holomorphic function meaning that it is differentiable in the neighborhood of any point within the complex domain. Effectively, this leads to the convenient statement that; $\overline{J_m(z)} = J_m(\bar{z})$ and the integral reduce to

$$\int_0^1 \mathbf{z}^\alpha \overline{\mathbf{z}}^{\alpha\mathbf{T}} r\mathrm{d}r = \int_0^1 \begin{bmatrix} J_m(\kappa_1 r)J_m(\bar{\kappa}_1 r) & J_m(\kappa_1 r)J_m(\bar{\kappa}_2 r) & \cdots & J_m(\kappa_1 r)J_m(\bar{\kappa}_M r) \\ & J_m(\kappa_2 r)J_m(\bar{\kappa}_2 r) & \cdots & J_m(\kappa_1 r)J_m(\bar{\kappa}_M r) \\ & & \ddots & \vdots \\ \text{Conj. Symm.} & & & J_m(\kappa_M r)J_m(\bar{\kappa}_M r) \end{bmatrix} r\mathrm{d}r$$

Notice that this matrix also holds conjugated symmetry since $\overline{J_m(z_1)J_m(\overline{z}_2)} = J_m(\overline{z}_1)J_m(z_2)$ conveniently caused by the holomorphic properties of the Bessel-functions. Thus only the upper or lower triangle needs to be integrated as the integration does not disrupt the holomorphic properties.

Fortunately, this integral is as mentioned what is known as Lommel's integral and contains an elegant analytical solution. Nonetheless, we need to introduce a perturbation to the Lommel integral to be able to retrieve all possible solutions i.e. solutions for $\kappa_n \neq \kappa_j$, $\kappa_n = \kappa_j$ and $\kappa_n = \bar{\kappa}_j$. The Lommel integral and its analytical solution including a perturbation is illustrated in equation (2.15).

$$\begin{aligned} \int_0^1 J_m(\kappa_n r)J_m(\bar{\kappa}_j r)r\mathrm{d}r &= \lim_{\varepsilon\to\kappa_j-\kappa_n} \int_0^1 J_m(\kappa_n r)J_m(\kappa_n r+\varepsilon r)r\mathrm{d}r \qquad (2.15) \\ &= \lim_{\varepsilon\to\kappa_j-\kappa_n} -\frac{1}{\varepsilon(\varepsilon+2\kappa_n)} \left[r\left\{J_m(\kappa_n r)(\kappa_n+\varepsilon)J_{m-1}(\kappa_n r+\varepsilon r) - \ldots \right.\right. \\ &\qquad \left.\left. -\kappa_n J_{m-1}(\kappa_n r)J_m(\kappa_n r+\varepsilon r)\right\}\right]_{r=0}^{r=1} \end{aligned}$$

So based on the solution the latter Lommel integral we can evaluate the fluid power flow analytically by means of equation (2.14) and (2.15) that now only contains $\frac{M^2+M}{2}$ simple function evaluations instead of a summation of M^2 Lommel integrals. Thus we avoid numerical errors causing a spurious oscillating power flow and similarly we can treat intensified loading conditions without caution. Further, as might be expected, this representation of the power flow is computationally stronger than the conventional integration of equation (2.8). Finally, to ensure a correct derivation the reformulation has been validated against the original integral for several cases.

2.3 Arbitrary time-harmonic excitations

In this section the vibro-acoustic model is expanded to include any arbitrary loading in either the acoustic or mechanical field. The conventional approach to arbitrary loadings is based on the convolution integral between Green's matrix and the load vector. In this section we will however conduct this convolution at an earlier stage as this has several computational advantages. By direct application of the conventional approach we would initiate similar issues as just addressed in section 2.2 and therefore it is more convenient to introduce the convolution in the explicit formulation of the amplitudes.

In addition to the explicit formulation of the amplitudes for Green's matrix presented in [Ledet et al., 2015] the amplitudes for any arbitrary loading, $q(x)$, can be expressed as in equation (2.16).

$$\begin{aligned}
C_m^{01(n)} &= \alpha_m^{(n)} \left[F_m^{(n)}\right]^{-1} \int_0^L q(x) \exp\left(-\tfrac{k^{(n)}}{R}x\right) \mathrm{d}x \\
C_m^{02(n)} &= -\beta_m^{(n)} \left[F_m^{(n)}\right]^{-1} \int_0^L q(x) \exp\left(-\tfrac{k^{(n)}}{R}x\right) \mathrm{d}x \\
C_m^{03(n)} &= -\left[F_m^{(n)}\right]^{-1} \int_0^L q(x) \exp\left(-\tfrac{k^{(n)}}{R}x\right) \mathrm{d}x \\
C_m^{04(n)} &= \frac{\mathrm{sgn}(x-\xi)}{R} k^{(n)} \left[F_m^{(n)}\right]^{-1} \int_0^L q(x) \exp\left(-\tfrac{k^{(n)}}{R}x\right) \mathrm{d}x \\
C_m^{05(n)} &= i\frac{R}{\omega} \left[F_m^{(n)}\right]^{-1} \int_0^1 q(r) \vartheta_m^{05(n)}(r) r \mathrm{d}r \\
C_m^{06(n)} &= i\frac{R}{\omega} \left[F_m^{(n)}\right]^{-1} \int_0^1 q(r) p_m^{05(n)}(r) r \mathrm{d}r
\end{aligned} \tag{2.16}$$

where each integral in most cases will be available in an analytical form or easily evaluated numerically.

2.3.1 Validation of the formulation

To verify whether the above formulation for an arbitrary load is derived correctly the formulation is validated by applying a load in the velocity field that is similar to the delta-function. A function suitable for such is for example the Gaussian probability function shown in equation (2.17).

$$q(r) = \frac{1}{\sigma\sqrt{2\pi}} \exp\left(-\tfrac{1}{2}\left(\tfrac{r-r_0}{\sigma}\right)^{p=2}\right) \qquad \Rightarrow \qquad \int_{-\infty}^{\infty} q(r)\mathrm{d}r = 1 \tag{2.17}$$

where r_0 is the location of the source, p the exponent that determines the shape ($p = 2$ in the normal distribution) and as the intensity is chosen to $\frac{1}{\sigma\sqrt{2\pi}}$ the infinite integral from $-\infty$ to ∞ will always be 1 independent on the choice of σ. Thus increasing the intensity to infinity by letting $\sigma \to 0$ the probability function becomes by definition the delta-function as shown in figure 2.4.

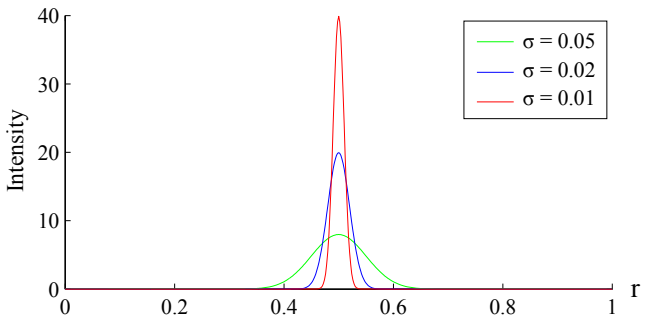

Figure 2.4. The Gaussian probability function located at $r_0 = 0.5$ for $\sigma = 0.05$ (green), 0.02 (blue) and 0.01 (red). For decreasing σ the probability function goes towards the delta-function.

To validate the derivation, the power flow is compared when calculated with a delta function and by the probability function both applied in the acoustical velocity field at $r_0 = 0.5$. For the

probability function σ is chosen to 10^{-3} which provides good resemblance to the delta-function. The power flow for the delta-function is seen in figure 2.5 while it is shown for the probability function in 2.6.

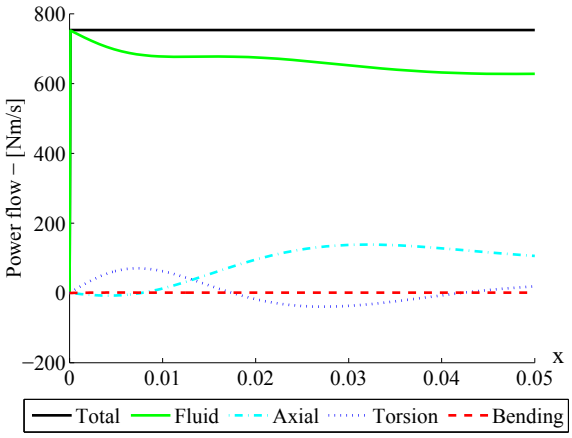

Figure 2.5. Delta-function applied in the acoustical velocity field at $r_0 = 0.5$, $f = 67.8$kHz and $m = 3$ with 25 waves included.

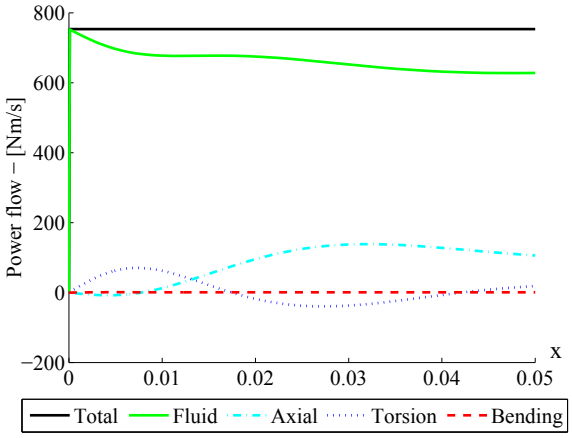

Figure 2.6. Probability function with $\sigma = 0.001$ applied in the acoustical velocity field at $r_0 = 0.5$, $f = 67.8$kHz and $m = 3$ with 25 waves included.

As is evident from the graphs the power flows are identical, which indeed imply that the derivation is correct. To support this the same graphs are presented in appendix B.2 in figure B.8 but for $\sigma = 0.1$. In this case the distributions are almost similar, however it is evident that the total power flow has increased which suggests that the source is not sufficiently localised to resemble the delta-function. This increase in the power flow when the source is less intense might at first seem strange but is actually explained by the studies conducted in section 3.3.3.

To ensure that the power flow is calculated correct it should also be verified whether or not the acoustical velocity resembles the applied load at the load introduction $\xi = 0$. Thus if the velocity is plotted across the radii at $\xi = 0$ it should resemble the applied load. This is illustrated in figure 2.7 and similar in figure 2.8 for the pressure field when the load is applied in the velocity field.

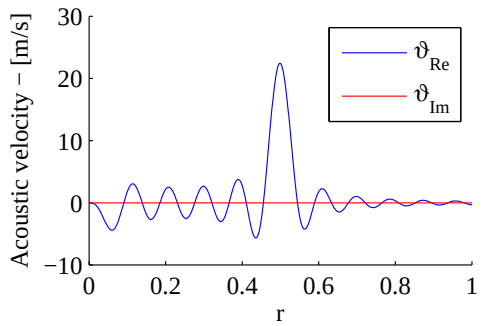

Figure 2.7. Real and imaginary part of the acoustic velocity across the radii at the load excitation, $\xi = 0$, with a velocity excitation applied through the probability function at $r_0 = 0.5$, $f = 67.8$kHz, $m = 3$ and 25 waves included.

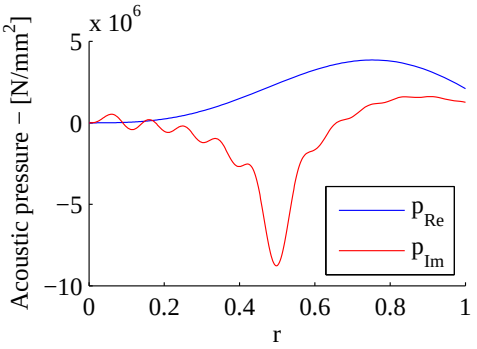

Figure 2.8. Real and imaginary part of the acoustic pressure across the radii at the load excitation, $\xi = 0$, with a velocity excitation applied through the probability function at $r_0 = 0.5$, $f = 67.8$kHz, $m = 3$ and 25 waves included.

Based on the figure it is clear that the velocity profile at the excitation point is somewhat similar to a delta-function except that it contains a finite intensity which is caused by truncating the

number of waves included in the analysis to a finite number, 25 in this case. Nevertheless, the acoustical profiles are inseparable to those of the delta-load when the same number of waves is included. Hence it can finally be concluded that the derivation of the amplitudes with arbitrary loading is correct - at least for the velocity field. However, following the same procedure the remaining derivations can be validated as well.

As a final comment to this comparison and to convergence studies in general it is of great importance to verify if the load is recovered sufficiently as, in case of the delta-function, the total power flow will be different if the load is not localised sufficiently as indicated in appendix B.2. For this specific case it is crucial to verify that the total power flow is kept constant and that the near field distribution has converged when the number of included waves is increased.

If we instead consider figure 2.8 which display the pressure profile at the excitation point when the load is applied in the velocity field. It should be noted that the pressure front is governed by the imaginary part. This implies that there is a 90° lag of phase between the velocity and the pressure field at this location. This phase shift does on the other hand vanish shortly after the excitation e.g. at $x = 0.01$m as seen in figure B.10 for the velocity profile and B.11 for the pressure profile in appendix B.2.

Arbitrary loading by a penalised probability function

As a final validation we subject the velocity field to the probability function, however, this time we change the power, p, in the exponential function from 2 to 500 to create a function that is nearly constant across the radii except close to the bounds i.e. at $r = [0; 0.1]$ and $r = [0.9; 1]$ where the function is zero as seen in figure 2.9. In this case σ is calculated to 0.3989, which makes the constant value 1 and the bounds as shown above when $r_0 = 0.5$. To keep the integral or input energy the same as for the delta-function we scale the function by 1.25, making the infinite integral 1. The applied load is shown in figure 2.9 and the corresponding power flow in figure 2.10 for $f = 67.8$kHz, $m = 3$ and 25 waves included.

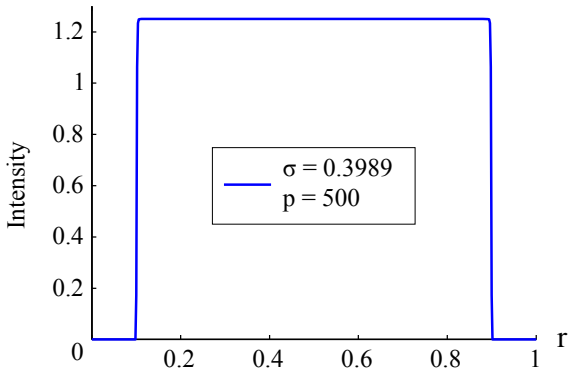

Figure 2.9. Modified Gaussian probability function penalised by $p = 500$ and $\sigma = 0.3989$ to get the bounds of the square and a unit input. Finally, the load is applied at $r_0 = 0.5$ and scaled by 1.25 to make the infinite integral 1.

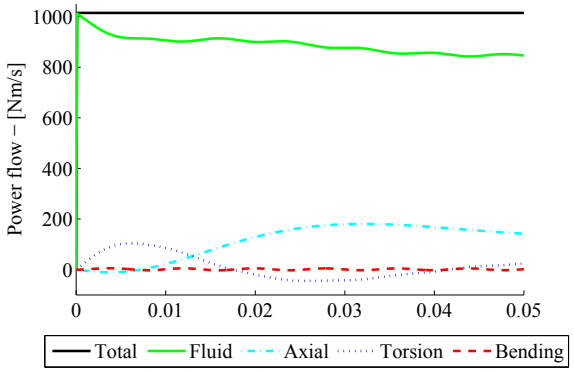

Figure 2.10. The power flow when the source of figure 2.9 is applied in the acoustic velocity field at $f = 67.8$kHz, $m = 3$ and with 25 waves included.

Based on the power flow in figure 2.10 and in 2.5 for a delta-function at $r_0 = 0.5$ it is seen that the distribution between the transmission paths are similar, nonetheless, with a higher total power and a slightly more oscillating nature with the constant load applied. This is once again explained by the phenomenons studied in section 3.3.3.

If we again evaluate the velocity profile at the excitation point to conclude on the number of waves included we observe through figure 2.11 that including $7-10$ waves in the analysis is not sufficient enough to resemble the load and in fact it seems that more waves are need for this load than for the probability function presented in figure 2.4. Therefore it is suggested to always evaluate convergence of symmetry, load and power flow as described in [Ledet et al., 2015] to prevent too few roots from being used in analysis where high accuracy is crucial. On the other hand it is expected that, for this case, 25 waves and above are sufficient; from the view point of load convergence.

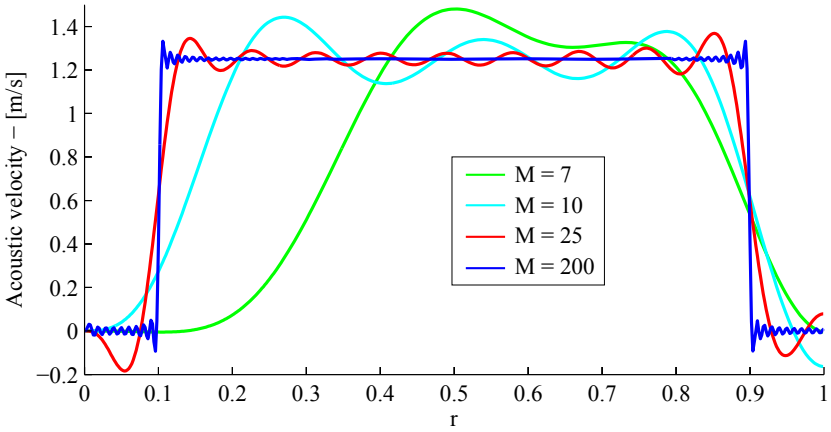

Figure 2.11. Recovery of the introduced load for an increasing number of waves. $7-10$ waves are considered too few while 25 and above are considered sufficient from the view point of load convergence.

As a benchmark figure 2.11 also includes the load when 200 waves are included in the analysis just to illustrate that eventually the profile converges to the applied one and the amplitudes calculated for the arbitrary load by equation (2.16) produces a load converging towards the applied load and the equations are derived correctly.

Notice also in figure 2.11 that Gibbs phenomenon is present at the "discontinuities" when the load turns rapidly towards zero. This imply that the response is a formulation based on a Fourier series i.e. a summation of trigonometric functions which should nevertheless be evident from the ansatz chosen by the Fourier method in the derivation of the governing equations, see e.g. [Ledet et al., 2015] or equation (2.9).

2.4 The Boundary Integral Equation Method

To improve this vibro-acoustic model further it is of great practical and commercial interest to extent the model to cover finite shells with arbitrary boundary conditions. This extension is possible by means of the Boundary Integral Equation Method (BIEM) described in e.g. [Sorokin et al., 2004] for shells in vacuo. In this thesis the BIEM is not extended to fluid-filled shells as this extension primarily serves the purpose of reducing the experimental complexity for hollow shells and hence allow for experiments on finite shells. Furthermore this extension is quite cumbersome and is due to time constraints found out of scope.

The derivation procedure for the BIE's for shells in vacuo are left to the literature in [Sorokin et al., 2004] why the complete derivation of the BIE's are not shown here. Instead we settle with presenting the final BIE's when derived for the notation used throughout this thesis.

From the governing equation for shells in vacuo it is evident that there will be 16 unknown boundary coefficients allocated as 4 force conditions and 4 displacement conditions at each boundary (recall that the shell formulation contains 4 generalised forces and 4 generalised displacements). To determine these 16 boundary coefficients 16 equations are necessary. The first 8 equations appear as boundary conditions formulated through a linear combination, equation (2.18), of forces and complementary displacements to account for arbitrary boundary conditions.

$$\begin{aligned}
&\textbf{At} \quad \mathbf{x = a} && \textbf{At} \quad \mathbf{x = b} \\
&\eta_{11}Q_{1m} + \eta_{12}u_m = 0 && \eta_{51}Q_{1m} + \eta_{52}u_m = 0 \\
&\eta_{21}Q_{2m} + \eta_{22}v_m = 0 && \eta_{61}Q_{2m} + \eta_{62}v_m = 0 \\
&\eta_{31}Q_{3m} + \eta_{32}w_m = 0 && \eta_{71}Q_{3m} + \eta_{72}w_m = 0 \\
&\eta_{41}Q_{4m} + \eta_{42}\frac{\mathrm{d}w_m}{\mathrm{d}x} = 0 && \eta_{81}Q_{4m} + \eta_{82}\frac{\mathrm{d}w_m}{\mathrm{d}x} = 0
\end{aligned} \tag{2.18}$$

where η_{ij} is the linear weighting coefficients and Q_j and u,v,w,w' the boundary forces and displacements.

In addition to the 8 equations in (2.18) another 8 are needed. These are formulated as Boundary Integral Equations which follows from the reciprocity relation of the Novozhilov-Gol'denveiser theory. This reciprocity relation can be found in e.g. [Sorokin et al., 2004] along with the derivation procedure for the BIE's as mentioned earlier. However, due to inconsistencies between the conventions and definitions of non-dimensional parameters as well as generalised forces and displacements the BIE's are derived and presented here in short for the notation used throughout this thesis.

For the free-free boundary condition relevant to the comparison with experiments the boundary conditions are formulated as $\eta_{i2} = 0$ for $i = 1, \ldots, 8$.

2.4.1 Boundary Integral Equations

Based on the reciprocity theorem we can derive Somigliana's identities when applying three sets of driving forces and their corresponding solutions. The driving forces are defined as the three possible point sources; $\lfloor \delta(x-\xi),0,0 \rfloor^T$, $\lfloor 0, \delta(x-\xi),0 \rfloor^T$ and $\lfloor 0,0,\delta(x-\xi) \rfloor^T$ with their associated trail solutions given as $\left\lfloor u_m^{0j}(|x-\xi|),v_m^{0j}(|x-\xi|),w_m^{0j}(|x-\xi|) \right\rfloor^T$ for $j = 1,2,3$. Notice that as these driving forces are similar to those used in the derivation of Green's matrix the associated trial solutions are effectively the entries in Green's matrix. Thus the trial solutions are readily available by facilitating the bi-orthogonality conditions described in [Ledet et al., 2015].

Now, by applying one driving set in the reciprocity relation at a time three identities of Somigliana appears as illustrated in equation (2.19). The fourth identity can be retrieved by the same analogy but is more conveniently found by differentiation of the third identity

with respect to the observation point, ξ.

$$
\begin{aligned}
u_m(\xi) = &\left[Q_{1m}(x)u_m^{01}(x,\xi) + Q_{2m}(x)v_m^{01}(x,\xi) + Q_{3m}(x)w_m^{01}(x,\xi) + Q_{4m}(x)\frac{\partial w_m^{01}(x,\xi)}{\partial x} \right]_{x=a}^{x=b} \\
&- \left[Q_{1m}^{01}(x,\xi)u_m(x) + Q_{2m}^{01}(x,\xi)v_m(x) + Q_{3m}^{01}(x,\xi)w_m(x) + Q_{4m}^{01}(x,\xi)\frac{\mathrm{d}w_m(x)}{\mathrm{d}x} \right]_{x=a}^{x=b} \\
&+ \int_a^b \left[q_{1m}(x)u_m^{01}(x,\xi) + q_{2m}(x)v_m^{01}(x,\xi) + q_{3m}(x)w_m^{01}(x,\xi) \right] \mathrm{d}x \\
v_m(\xi) = &\left[Q_{1m}(x)u_m^{02}(x,\xi) + Q_{2m}(x)v_m^{02}(x,\xi) + Q_{3m}(x)w_m^{02}(x,\xi) + Q_{4m}(x)\frac{\partial w_m^{02}(x,\xi)}{\partial x} \right]_{x=a}^{x=b} \\
&- \left[Q_{1m}^{02}(x,\xi)u_m(x) + Q_{2m}^{02}(x,\xi)v_m(x) + Q_{3m}^{02}(x,\xi)w_m(x) + Q_{4m}^{02}(x,\xi)\frac{\mathrm{d}w_m(x)}{\mathrm{d}x} \right]_{x=a}^{x=b} \\
&+ \int_a^b \left[q_{1m}(x)u_m^{02}(x,\xi) + q_{2m}(x)v_m^{02}(x,\xi) + q_{3m}(x)w_m^{02}(x,\xi) \right] \mathrm{d}x \\
w_m(\xi) = &\left[Q_{1m}(x)u_m^{03}(x,\xi) + Q_{2m}(x)v_m^{03}(x,\xi) + Q_{3m}(x)w_m^{03}(x,\xi) + Q_{4m}(x)\frac{\partial w_m^{03}(x,\xi)}{\partial x} \right]_{x=a}^{x=b} \\
&- \left[Q_{1m}^{03}(x,\xi)u_m(x) + Q_{2m}^{03}(x,\xi)v_m(x) + Q_{3m}^{03}(x,\xi)w_m(x) + Q_{4m}^{03}(x,\xi)\frac{\mathrm{d}w_m(x)}{\mathrm{d}x} \right]_{x=a}^{x=b} \\
&+ \int_a^b \left[q_{1m}(x)u_m^{03}(x,\xi) + q_{2m}(x)v_m^{03}(x,\xi) + q_{3m}(x)w_m^{03}(x,\xi) \right] \mathrm{d}x
\end{aligned}
\tag{2.19}
$$

$$
\begin{aligned}
\frac{\mathrm{d}w_m(\xi)}{\mathrm{d}\xi} = &\left[Q_{1m}(x)\frac{\partial u_m^{03}(x,\xi)}{\partial \xi} + Q_{2m}(x)\frac{\partial v_m^{03}(x,\xi)}{\partial \xi} + Q_{3m}(x)\frac{\partial w_m^{03}(x,\xi)}{\partial \xi} + Q_{4m}(x)\frac{\partial^2 w_m^{03}(x,\xi)}{\partial \xi \partial x} \right]_{x=a}^{x=b} \\
&- \left[\frac{\partial Q_{1m}^{03}(x,\xi)}{\partial \xi}u_m(x) + \frac{\partial Q_{2m}^{03}(x,\xi)}{\partial \xi}v_m(x) + \frac{\partial Q_{3m}^{03}(x,\xi)}{\partial \xi}w_m(x) + \frac{\partial Q_{4m}^{03}(x,\xi)}{\partial \xi}\frac{\mathrm{d}w_m(x)}{\mathrm{d}x} \right]_{x=a}^{x=b} \\
&+ \int_a^b \left[q_{1m}(x)\frac{\partial u_m^{03}(x,\xi)}{\partial \xi} + q_{2m}(x)\frac{\partial v_m^{03}(x,\xi)}{\partial \xi} + q_{3m}(x)\frac{\partial w_m^{03}(x,\xi)}{\partial \xi} \right] \mathrm{d}x
\end{aligned}
$$

Now to extract the necessary 8 equations from the 4 BIE's above an observation point is placed at each boundary such that we get 4 additional equations at $\xi = a$ and 4 additional equations at $\xi = b$. Thus the system of 16 equations can be rewritten on the simple linear algebraic form as shown in (2.20).

$$
\mathbf{B_{IEM}}(\omega)x = q(\omega) \tag{2.20}
$$

where x represents the 16 boundary coefficients ($Q_{1m}(x = a)$, $Q_{1m}(x = b)$ etc.), $\mathbf{B_{IEM}}$ the coefficient matrix and $q(\omega)$ is the applied load in forces vibration. Notice that both $\mathbf{B_{IEM}}$ and q are frequency dependent.

From the latter equations we are able to derive both the resonance frequencies but similar the response in forced vibration. If we consider free vibration the equations system reduce as $q = 0$. In this case the resonances are found when the determinant of the coefficient matrix $\mathbf{B_{IEM}}$ is zero as the resonances are the non-trivial solution to the equation system. In practice the resonances are found in a discrete frequency sweep as the trial solutions, $\left| u_m^{0j}(|x-\xi|), v_m^{0j}(|x-\xi|), w_m^{0j}(|x-\xi|) \right|^T$, are calculated at discrete frequencies. This procedure for finding the resonances are shown in figure 2.12 for $m = 4$, the geometry and material data for the thin shell facilitated in the experiments and with free-free boundary conditions.

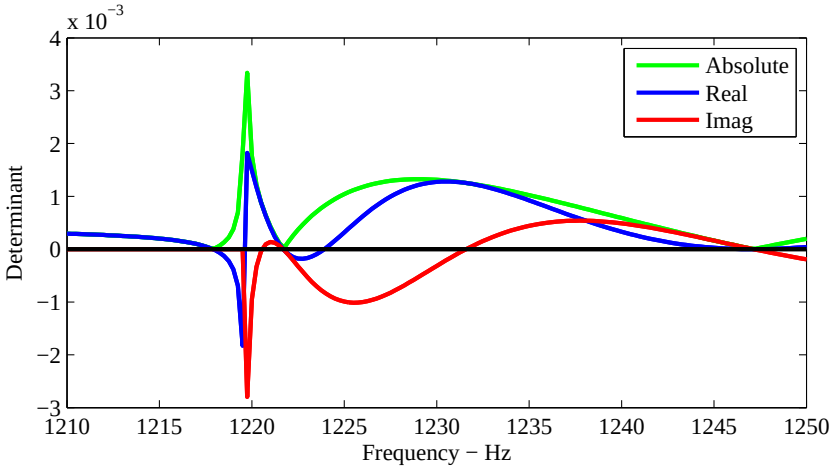

Figure 2.12. Frequency sweep for the determinant to locate the resonance frequencies. Illustration based on $m = 4$ and the geometry and material data for the thin shell facilitated in the experiments with free-free boundary conditions.

From the figure it is seen that for the thin shell with free-free boundary conditions at $m = 4$ we can locate the resonances where the absolute value is zero i.e. at the cut-on at approximately 1218Hz and again at approximately 1222 and 1247Hz.

The general response caused by an arbitrary loading reveals by solving the algebraic equation system and substituting the solution back into Somigliana's identities where the general response is then given as an implicit function of frequency and an explicit function of axial distance by means of ξ. The validation of this procedure is skipped for now but is nonetheless treated in chapter 4.

This extension to the area of application does indeed lead to significant reduction of experimental complexity as concerns regarding e.g. anechoic terminations are eliminated. Furthermore it is crucial to noticed that the extension into finite shells is based on solid analytical equations which are of no less accuracy than the adopted governing equations from Novozhilov-Gol'denveiser thin shell theory. Thus in conclusion the extension of the model into the finite domain retains the same accuracy, while the sources of error related to experiments are lowered remarkably.

This concludes the theoretical chapter of improvements to the vibro-acoustic model and in the following chapters these improvements are adopted to cope with the expectations of the thesis. Thus in the following we start out by applying the formulation for an arbitrary source and the reformulation of the power flow equations to address the response of the waveguide when subjected to deduced acoustical sources.

Source characterisation and reponse by CFD-data 3

In this chapter the attention is drawn towards assessing the vibro-acoustic performance when the pipe system is connected to an operating pump. The operating pump is in this case represented by a time varying discrete pressure and velocity field estimated by means of a CFD analysis. In the following the CFD-data provided by Grundfos is presented and subsequently the CFD-data is decomposed into the domain of the vibro-acoustical model. Finally, the response when the vibro-acoustic model is subjected to the CFD-data is assessed.

Through the following study the material parameters of the shell are similar to those presented in table 2.1, however with a radii of 75mm and a shell thickness of 7.5mm.

3.1 Data from CFD-modelling of an operating pump

The CFD-data, referred to as the original data, is provided by Grundfos for two different cases: 1) Discrete nodal pressure and velocity distribution in the outlet cross section (illustrated in figure 3.1) when the pump is operating at nominal load, referred to as $Q100$ and 2) when the pump is operated at 5% of the nominal load, referred to as $Q5$.

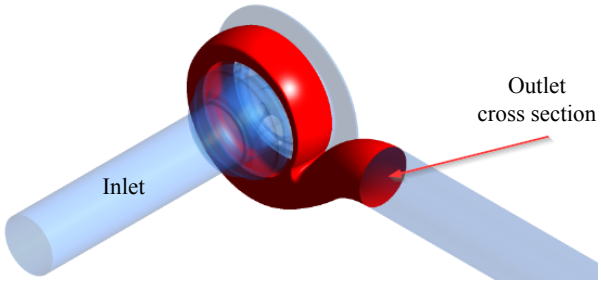

Figure 3.1. Pump casing with indication of in- and outlet. The CFD-data is given at the cross-section illustrated. Figure provided by [Grundfos Holding A/S, 2014-2015].

In both cases the data represent one revolution of the impeller measured in 144 time steps providing a Δt_{100} = 2.8e-04s for $Q100$ and similar for $Q5$. In practical CFD-analysis this is done by changing the boundary conditions by changing the massflow with respect to a flow point. This is as mentioned conducted at Grundfos' CFD department and as it is not inside the scope of this thesis the underlying CFD assumptions are not considered further and the CFD-data is therefore just treated as the source of interest.

To visualize the time varying distribution of the pressure and velocity in the x, y and z direction for each of the two cases the attention should be drawn to the appendix CD A.1 where animations of these eight cases can be found. Nonetheless, the pressure and velocity (in

the x-direction) distribution can be seen in figure 3.2 to 3.5 at an arbitrarily chosen time frame corresponding to a half revolution of the impeller.

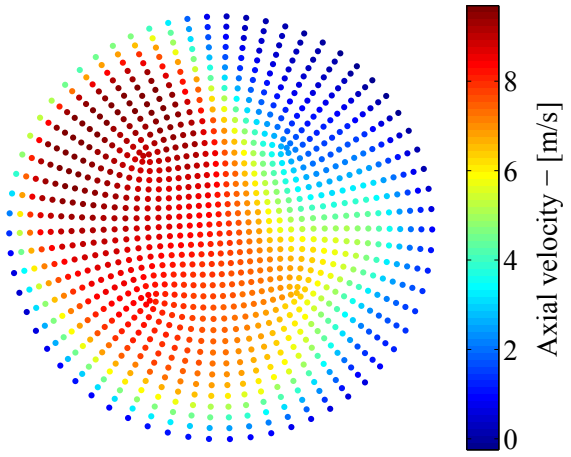

Figure 3.2. Axial velocity distribution for $Q100$ at a half revolution of the impeller.

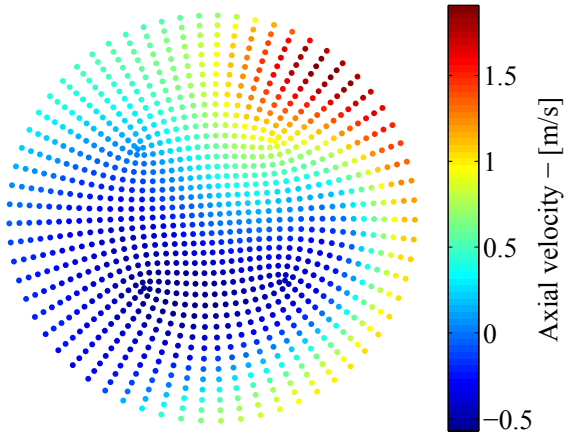

Figure 3.3. Axial velocity distribution for $Q5$ at a half revolution of the impeller.

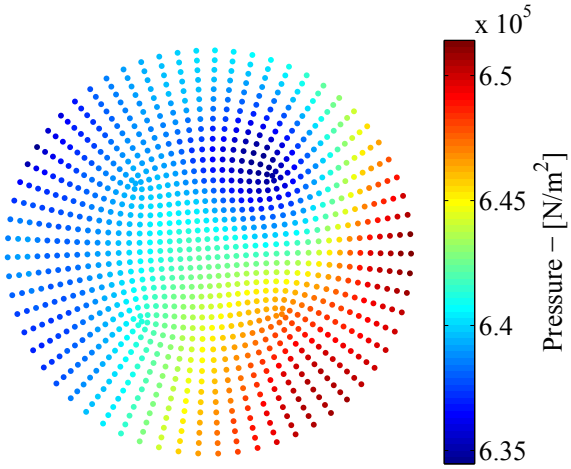

Figure 3.4. Pressure distribution for $Q100$ at a half revolution of the impeller.

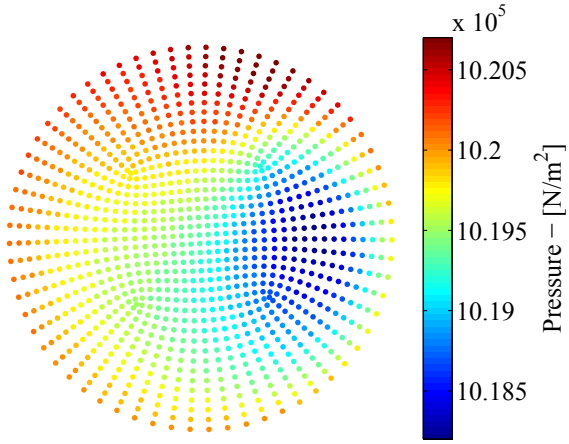

Figure 3.5. Pressure distribution for $Q5$ at a half revolution of the impeller.

In a brief investigation of these fields it has been found that the pressure pulsations are highest at $Q5$ and that the velocity pulsations are highest at $Q100$.

As a final comment notice that confer to the simplified definition of the acoustic velocity, $v = \frac{\mathrm{d}\phi}{\mathrm{d}x}$, in the model our interest is only the axial velocity as this constitutes the primary source. Thus the velocity in y and z are not treated further in the following.

3.2 Source characterisation of CFD-data by modal decomposition

In the interest of analysing the vibro-acoustic performance of a pipe system when subjected to the CFD-data of an operating pump it is necessary to convert the CFD-data into the domain where the vibro-acoutical model is defined. That is; the time varying data must be decomposed into frequencies, which is then further decomposed into the circumferential wave-numbers and finally interpolated into continuous profiles which can be applied as arbitrary functions as

described in section 2.3. This is done first by a Fourier transformation, then decomposed by a Fourier series and finally made continuous by any desired regression.

3.2.1 Shifting from time to frequency

To ensure that the CFD-data and the vibro-acoustic model are confined by the same assumptions the assumptions from the model must be applied to the CFD-data as well. Since the model is confined to time harmonic response the CFD-data must be bounded by the same assumption i.e. we assume that this one revolution of the impeller is free of initial conditions and will continue harmonically with the exact same characteristic. This is a reasonable assumption from the view point of the CFD analysis provided by Grundfos as the analysis is confined by the very same assumptions.
The latter and following theory on discrete and continuous Fourier Transformations and series are based on [Kreyszig, 2011] and for elaborated theory this reference should be accessed.

Thus to change from the time domain to the frequency domain the CFD-data is transformed by means of a Fourier Transform defined as in equation (3.1) for continuous functions.

$$\mathcal{F}(\omega) = \frac{1}{2\pi} \int_{-\infty}^{\infty} f(t) \exp(-i\omega t) \mathrm{d}t \tag{3.1}$$

For the discrete data set the FT is reformulated from an integral to a summation across the given data points such that t is represented by discrete time steps $t = nT$ for $n \in \mathbb{Z}$. This is also known as the Discrete Time Fourier Transform (DTFT) that is a periodic summation in time of the original function providing a frequency-continuous function as is shown in equation (3.2).

$$X_{1/T}(\omega) = \frac{1}{N} \sum_{n=-\infty}^{\infty} x(nT) \exp(-i\omega nT) \qquad \text{for} \qquad n \in \mathbb{Z} \tag{3.2}$$

where $X(\omega)$ is the Fourier transformation of the function $x(t)$ sampled at $\frac{1}{T}$ Hz, n is the sample number, N the total number of samples, T the sampling time and $\mathbb{Z}$ represents the integer domain.

On the other hand we are considering the CFD-data as being periodic on a finite period defined by one revolution of the impeller i.e. it is seen as periodic from the last sample, N. Thus the DTFT is sampled over one period at discrete frequencies providing a periodic summation of the DTFT. This is known as the Discrete Fourier Transform (DFT) that is equivalent to the coefficients of the Fourier Series i.e. the Fourier coefficients are discrete samples of the continuous Fourier Transformation.

In this case the discrete angular frequency is expressed as

$$\omega_h = \frac{2\pi h}{NT} \qquad \text{for} \qquad h = 0,1,\ldots,N-1 \tag{3.3}$$

and the DFT is

$$X_h = \frac{1}{N} \sum_{n=0}^{N-1} x_n \exp\left(-i\frac{2\pi h n}{N}\right) \tag{3.4}$$

where x_n is the time discrete data set and X_h the discrete Fourier Transform at discrete frequencies defined by integer numbers of h. Notice here that the summation is truncated to

$N-1$ samples as we force periodicity at N and consequently the value at $n=0$ and $n=N$ are forced to be the same. If this assumption is poor, forcing periodicity here would introduce the presence of spurious frequencies in the transformed response which may affect certain aspects of the analysis.

In practice the DFT is conducted through a fast algorithm called a Fast Fourier Transform (FFT), which is essentially the same as a DFT but evaluated much faster. Using FFT over DFT will reduce the number of operations from N^2 to $N\log_2(N)$ according to [Kreyszig, 2011].

Conducting a FFT on the available CFD-data will give the velocity and pressure amplitudes illustrated in figure 3.6 and 3.7 for $Q100$ at $f=25$Hz. Notice here that the transformation is done for each node in the CFD-data. Furthermore it is given from the definition in (3.4) that the amplitudes will be complex and therefore this and the following figures will only represent the real part of the amplitudes unless stated otherwise.

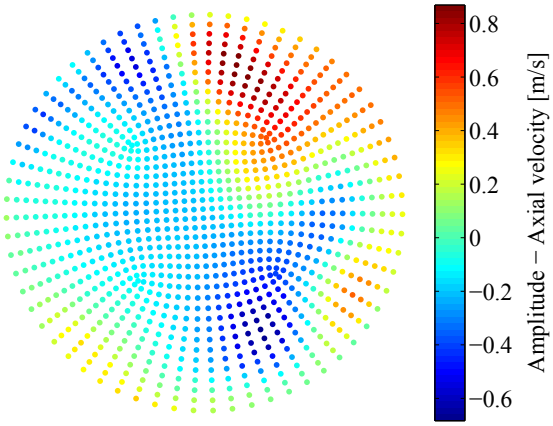

Figure 3.6. Axial velocity pulsations at $f=25$Hz for $Q100$.

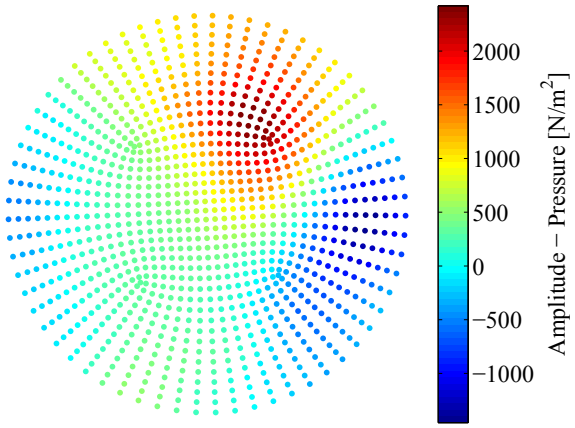

Figure 3.7. Pressure pulsations at $f=25$Hz for $Q100$.

From the latter transformation it is given that the maximum frequency in the spectrum is 1760Hz and the frequency resolution is 24.79Hz. If we wish to analyse higher frequencies or analyse with a higher frequency resolution a higher degree of information is needed. For a higher frequency spectrum the sampling frequency in the CFD analysis must be increase by at least 2 times the highest desired frequency - specified by Nyquist's sampling theorem. Nonetheless many commercial Fourier analysers for experimental purposes usually suggest 2.56 times the desired spectrum.
To increase the frequency resolution on the other hand the sampling time needs to be increased. In this case the sampling time is approximately 0.04s and to get a 1Hz resolution we need to sample 25 revolutions of the impeller. Alternatively this can be done mathematically simply by repeating the data 25 times. However, this is only feasible if the data is indeed periodic, meaning that the value at sample $n=0$ and $n=N$ must be identical. If this is not the case spurious frequencies and amplitudes will occur in the spectrum.

In the following sections we treat each discrete frequency separately i.e. the following applies for each h in equation (3.4) and again only the real part of the amplitudes are illustrated.

3.2.2 Mapping from unstructured to structured mesh

To be able to decompose the data further into the circumferential wave-numbers the mesh should be structured in the sense illustrate in figure 3.8. However, as this is not completely

legit from the view point of CFD analysis such a mesh is rarely the case. To comprehend this the data is mapped by a linear interpolation from the unstructured CFD-mesh onto the structured grid shown in figure 3.8 where the radial and circumferential grid is 16 and 10, respectively, meaning that there will be 10 circular grid lines at each $1/10^{\text{th}}$ radii and 16 radial grid lines spaced by an angle of $\pi/8^{\text{th}}$.

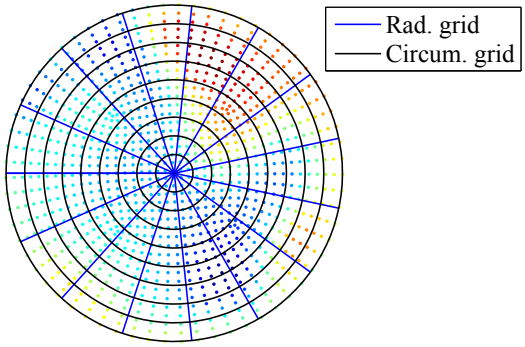

Figure 3.8. Illustration of the structured grid where the unstructured CFD-data is mapped onto. Background data is similar to that in figure 3.6 and the grid is here divided into 10 circular grid lines and 16 radial grid lines.

If the grid size is chosen sufficiently the mapped data should reflect the actual data well and in figure 3.9 the interpolated data is shown as a 3-dimensional plot for $Q100$ at $f = 25$Hz.

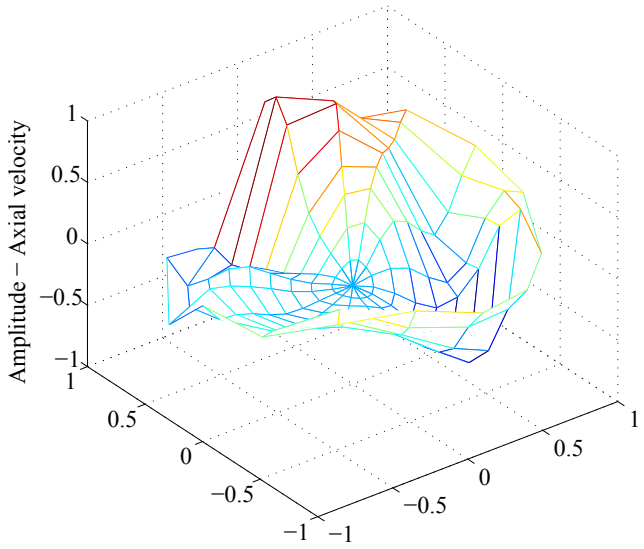

Figure 3.9. The axial velocity from figure 3.6 mapped onto the grid shown in figure 3.8. It is difficult to determine whether the data is represented well or not, hence an error estimation is necessary.

Based on this figure it is difficult to determine whether the mapped data reflect the original data well and whenever the data is not identical some (maybe important) information may be unintentionally sorted out of the circumferentially decomposed data. This is known as modal leakage and to reduce this it is necessary to estimate the error between the two data set to qualify the mapped data. This is treated in detail in the following section.

As a final comment it should be noted that the radial grid division determines, besides the quality of the mapping, also the maximum circumferential wave-number that can be analysed - determined by Nyquist's sampling theorem. This is further discussed in section 3.2.4.

3.2.3 Map quality by error estimation

To ensure high quality of the map it is crucial that the error between the data sets are estimated such that the possibility of sorting out critical modal information during the data processing is reduced. To determine a proper grid size in the mapping the quality of the map needs to be evaluated. This can be done by estimating an error between the original FFT data and the mapped data. However, as not all nodes are coincident in the two grids it is rather involved to determine the quality, nonetheless the procedure used in this thesis is described in detail in appendix C and in the following only the conclusions are presented.

The idea of determining the map quality is based on the grids ability to recover the original FFT data in a double mapping procedure i.e. estimating the error between the original FFT data and the data when it is first mapped onto the grid and then back onto the original mesh. The error between the to data set can then be see as a measure of the quality of the mapping and from this analysis the proper grid size can be determined.

Based on this investigation it was found that the 16x10 grid shown in figure 3.8 is not sufficient to predict the peaks present in the FFT data and in conclusion the proper grid is chosen to a 32x20 grid.

As a final remark it is not always straight forward to qualify the grid by this method, in particular when the amplitudes at certain frequencies crosses the zero axis as this compromises the quality of the relative error measure. This is seen for instance at the higher frequencies and especially in the velocity field. The procedure facilitated to overcome this issue in the present thesis can likewise be found in appendix C.

3.2.4 Circumferential decomposition of FFT data

The final stage of data processing to make the CFD-data cope with the vibro-acoustical model is to decompose the data further into each circumferential wave-number and according to the procedure outlined initially this is done first by a Fourier series in the circumference and then a regression in the radial direction.

The first step is to create a Fourier series at the chosen frequency for each of the circumferential grid lines. The Fourier series is defined as a periodic summation of trigonometric function as shown in equation (3.5).

$$f(\theta) = \sum_{m=0}^{M} \left[a_m \cos(m\theta) + b_m \sin(m\theta) \right] \tag{3.5}$$

Or as a periodic summation of exponentials as shown in (3.6).

$$f(\theta) = \sum_{m=0}^{M} c_m \exp(im\theta) \tag{3.6}$$

where m is the circumferential wave-number, M the total number of circumferential waves included in the Fourier representation and the coefficients, a_m, b_m and c_m are defined as in

equation (3.7) for the continuous and discrete case.

$$\begin{aligned} a_m &= \frac{2}{\tau}\int_0^\tau f(\theta)\cos(m\theta)\,\mathrm{d}\theta \quad &\rightarrow \quad &\frac{2}{N}\sum_{n=0}^{N-1} f(\theta_n)\cos(m\theta_n) \\ b_m &= \frac{2}{\tau}\int_0^\tau f(\theta)\sin(m\theta)\,\mathrm{d}\theta \quad &\rightarrow \quad &\frac{2}{N}\sum_{n=0}^{N-1} f(\theta_n)\sin(m\theta_n) \\ c_m &= \frac{1}{\tau}\int_0^\tau f(\theta)\exp(-im\theta)\,\mathrm{d}\theta \quad &\rightarrow \quad &\frac{1}{N}\sum_{n=0}^{N-1} f(\theta_n)\exp(-im\theta_n) \end{aligned} \tag{3.7}$$

where $\theta_n = n\frac{2\pi}{N}$ and τ is the period which in this case corresponds to 2π.

From the above definitions it is obvious that the complex coefficients can be expressed in terms of the real coefficients through Euler's identity such that; $c_m = \frac{a_m - ib_m}{2}$ and therefore either of the latter definitions are valid in the decomposition of CFD-data. Even though the velocity potential in the derivation of the governing equations are introduced as $\phi(\theta) = \bar{\phi}\cos(\theta)$ it is still beneficial to retain the phase information in terms of the sine part. Therefore it is most convenient to adopt the exponential formulation even though it is divided into the cosine and sine parts for illustration purposes in the graphs. However, it should be noted that if the assumption regarding the circumferential distribution of the velocity potential is correct the exponential decomposition will reduce to a pure cosine decomposition. Hence the presence and magnitude of the sine part is very useful in validation of this assumption.

In the definition of the complex coefficients c_m it should be noted that this corresponds to the Discrete Fourier Transformation presented in equation (3.4). Thus instead of calculating the coefficients by means of the latter discrete formula it is more convenient to do a FFT and retrieve the complex coefficients from this. Notice furthermore that due to the polar grid the sampling frequency is identical for any given circumference, thus the FFT can be conducted for the full data set of the grid an no further processing of the data is necessary.

Based on these coefficients the Fourier series can be assembled for each circumferential grid line and plotted as in figure 3.10 to evaluate the circumferential distribution at the given frequency.

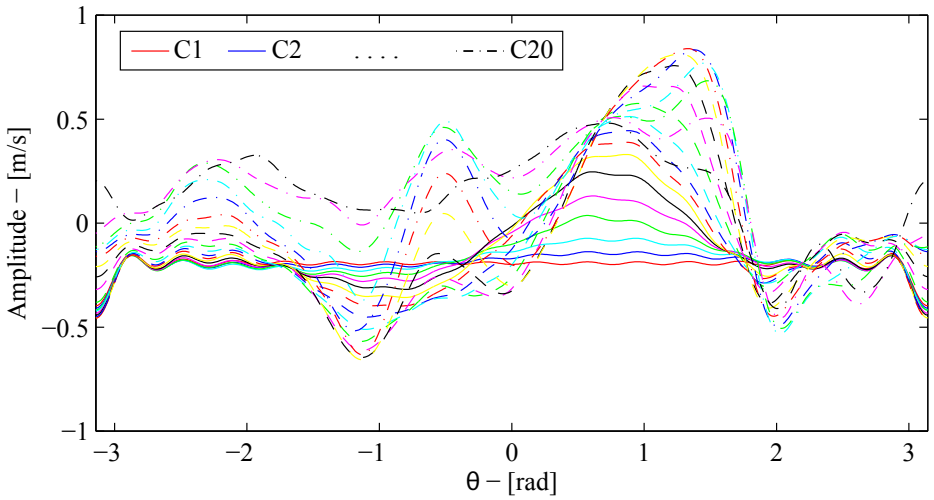

Figure 3.10. Circumferential distribution of the $Q100$ axial velocity at $f = 25$Hz for each circumferential grid line represented as a Fourier series.

Based on the circumferential distribution at the grid lines it is evident that the distribution at

each circumference are similar but as the shell wall is approached the peak magnitudes increase just as seen from the contour graphs in e.g. figure 3.6. Notice finally that the outermost circumference, C20, differs from the others in the shape characteristic which is expected to be a consequence of the viscosity effects.

To terminate at a circumferential decomposed data set the subsequent step is simply to interpolate the modal amplitudes from each of the circumferential grid line retrieved from equation (3.7) into a continuous function. The curve fitting procedure can be chosen as desired e.g. a Fourier series, polynomial regression, spline interpolation etc.

To clarify the procedure imagine that we specifically wish to assess the behaviour of the flexural mode, $m = 1$. In this case we create a polynomial regression based on the amplitudes $c_{m=1}^{(j)}$ where j represent the j^{th} circumferential grid line.

From this procedure we can estimate the radial (continuous) load distribution of the CFD-data at a given frequency contained in the CFD-data and at a given circumferential wave-number, m. This corresponds exactly to the acoustical source at this frequency and wave-number. If this continuous radial distribution is applied as an arbitrary function it is possible to assess the response of the vibro-acoustic shell. The radial distribution for the circumferential wave-numbers $m = 0, \ldots, 5$ at $f = 25$Hz are shown in figure 3.11.

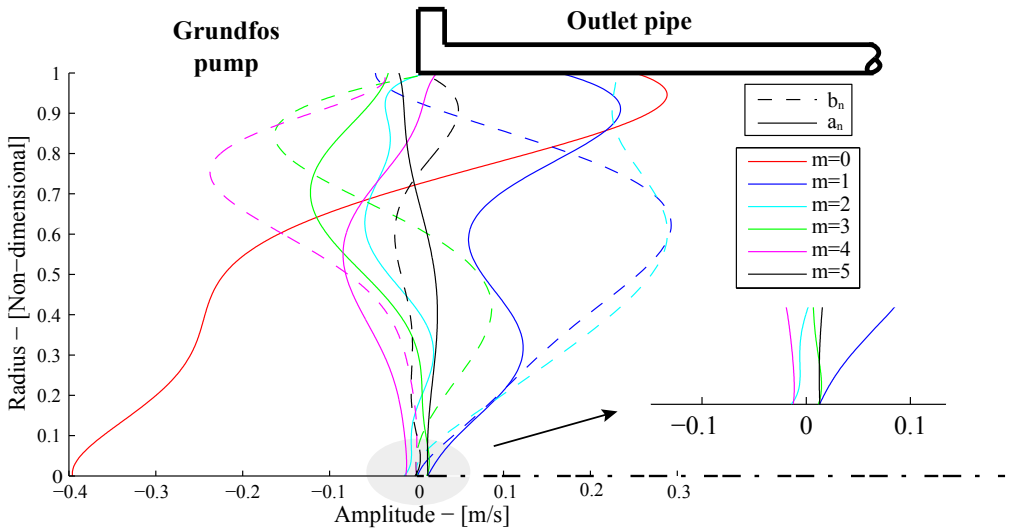

Figure 3.11. Radial distribution at each circumferential wave-number at $f = 25$Hz for $Q100$. The modal leakage for $m \neq 0$ is seen in terms of non-zero values at $r = 0$. Notice that the coefficients of the sine part are non-zero and the assumption regarding the circumferential distribution of the velocity potential may be questionable.

From the radial distributions of the derived acoustic source from the velocity field at $f = 25$Hz several interesting things can be observed. First of all it is evident that the magnitude of the profiles drops gradually with increasing circumferential wave-numbers. This is also to be expected as the primary part of the pulsations are usually carried in the lower order modes. Furthermore slight modal leakage can also be observed from the figure at the non-zero modes and is seen as the non-zeros amplitudes at $r = 0$. In practice only $m = 0$ can carry loads at the centre and contributions from the zero-mode is therefore present in the non-zero modes. To avoid this we should impose the zero departure manually in the decomposition as the automatic procedure treats the centre point as a circle of zero radii with 32 samples of equal magnitude - corresponding to the centre value.

Finally, it is seen that the sine part (represented by a dash line) is indeed present in the decomposed CFD-data and in fact they seem governing in relation to the cosine terms. This immediately implies that the assumption regarding the circumferential distribution of the velocity potential may be poor and could conveniently be changed to $\exp(im\theta)$ over $\cos(m\theta)$. Nonetheless it might on the other hand also be caused by pitfalls or unfortunate assumptions in the CFD-data which then provides spurious phase information. However, the investigation conducted in this thesis is not sufficient to designate one hypothesis over the other. Thus to finally prove or disprove the hypothesis measurements on a pipe subjected to a pump must be conducted and by means of the modal decomposition of the experimental results it should be possible to conclude on the presence of the sine term.

Notice, however that the circumferential decomposition is confined by Nyquist's sampling theorem i.e. in this case only $m = 0, \ldots, 15$ can be assessed by 32 samples without introducing aliasing issues. If it is desirable to analyse higher circumferential wave-numbers it is necessary to refine the radial grid. Similar the number of governing modes present in the CFD-data is also of crucial importance for the grid size as the truncation to a finite number, M, in the Fourier representation of equation (3.6) may introduce significant errors. This is discussed in detail for the modal decomposition of the experimental data in section 4.3 as the issues are more pronounced here and furthermore it is not expected that this type of modal leakage will occur for the chosen 32x20 grid.

The radial grid on the other hand is independent of the number of circumferential waves we wish to include but do instead determine the resolution of the radial distribution. A refined radial grid is only necessary if distinct peaks are observed in the interpolated radial distribution.

3.3 Vibro-acoustic response with acoustical sources from CFD-data

With the modal decomposition conducted for the CFD-data it is possible to assess the vibro-acoustic performance of the shell when subjected to the characteristics from an operating pump (Q100) provided as CFD-data. Thus the following analysis is confined by the vibro-acoustic model and therefore discrete frequencies and integer circumferential wave-numbers are treated separately in the following. Furthermore 25 waves are included in the analysis unless stated otherwise and confer to the discussion in [Ledet et al., 2015] we are confident with "only" 25 waves as convergence issues related to symmetry conditions, load convergence and convergence of the power flow are directly visible in the graphs we wish to assess.

3.3.1 Power flow analysis

As mention the frequency spectrum of the CFD data spans from 0 to 1760Hz and the analysis is therefore restricted to this spectrum. Furthermore this spectrum only includes 3 modes ($m = 0, 1, 2$) with cut-on and it is therefore reasonable to confine the analysis to this spectrum as well.

In figure 3.12 and 3.13 the power flow is shown at 50Hz for $m = 1$ and $m = 2$, respectively. The load in these figures are applied in the acoustic velocity field and by means of the radial distribution for c_m obtained through the CFD modal decomposition. The real and imaginary load for $m = 1$ is depicted in figure 3.15.

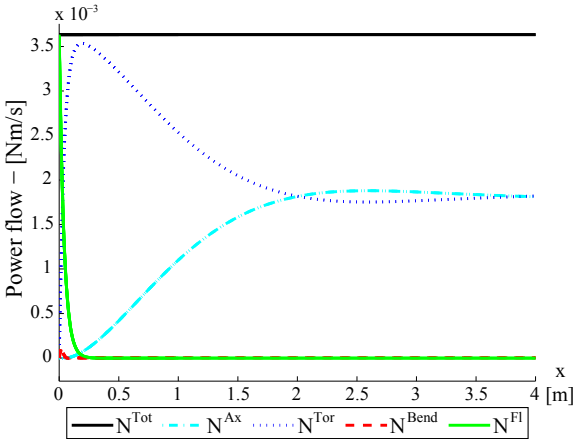

Figure 3.12. Power flow through the shell at 50Hz and $\underline{m = 1}$ when the source is applied in the velocity field by the radial distribution for c_m obtained in the modal decomposition.

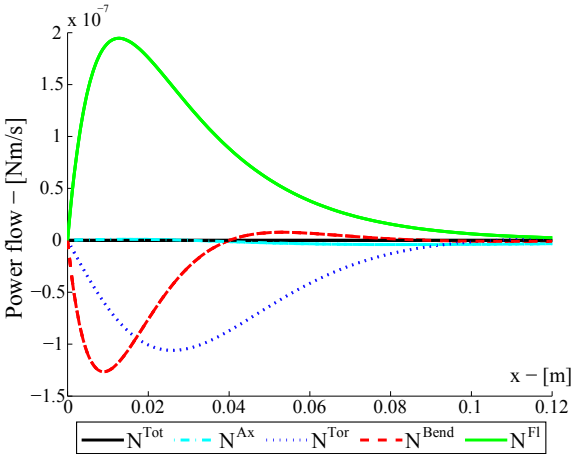

Figure 3.13. Power flow through the shell at 50Hz and $\underline{m = 2}$ when the source is applied in the velocity field by the radial distribution for c_m obtained in the modal decomposition.

From the power flow analysis at 50Hz it is clear that at $m = 1$ propagating waves are present while at $m = 2$ no propagating waves are present and the total power flow sum to zero. Based on the left power flow graph it is evident that the energy in the fluid escapes rapidly to the shell and is at first carried primarily as torsional energy but disperse and is carried equally by the torsional and axial wave in the far field. In this case it is interesting to notice that this transition of the energy transporting path appears very slow at low frequencies and the (re)distribution completes approximately 4 metres from the excitation cross section.

From the right figure it is seen that we are able to accurately predict the near field energy (re)distribution even for wave-numbers and frequencies where no propagating waves are present. This is possible only because a significant amount of waves are retained in the analysis which is again only possible when we apply the bi-orthogonality conditions to solve the equation system and express the amplitudes and power flow analytically. Notice here that even though no waves are propagating along the shell (there are no lasting vibrations in the shell at this mode) the interchanging between transmissions paths may still be governing for the sound radiated from the pipe.

As a final remark it is seen directly in the figures that the power flow/symmetry conditions are converged confer to [Ledet et al., 2015] by including 25 waves as the structural transmission paths depart from zero.

Similar observations are found at higher frequencies, however, the transition phase terminates faster at higher frequencies and for the power flow shown in figure 3.14 for $m = 2$ at 1760Hz the redistribution ceases in approximately 400mm.

Again the energy interchange between the different transmission paths in the near field and is carried in the structure in the far field. For other frequencies and wave-numbers the distribution of the power flow is basically identical to the cases shown and the deviations are found in the magnitude of the power flow and in the characteristic length over which the transmission paths settle.

In the spectrum defined by the CFD-data there is only one propagating wave in the coupled system i.e. $m \neq 0$ and phenomenons such as beating, continuous interchanging of energy

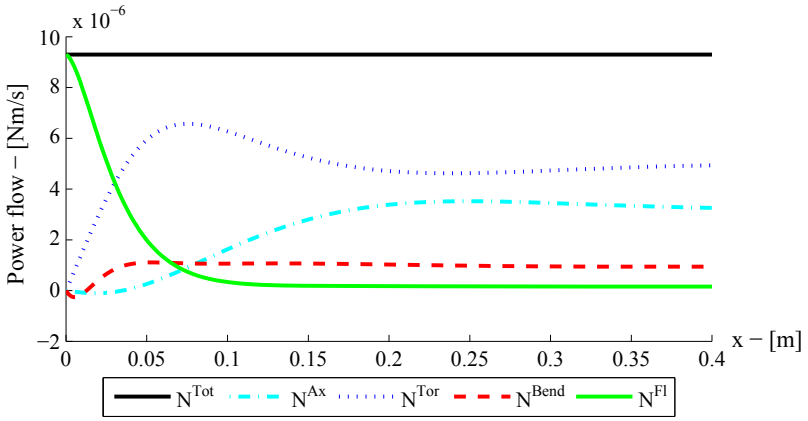

Figure 3.14. Power flow through the shell at 1760Hz and $m = 2$ when the source is applied in the velocity field by the radial distribution for c_m obtained in the modal decomposition.

between transmissions paths etc. are therefore not present in the far field. Thus the energy redistribution must settle at some point and be constant in the far field.

Through the study of the pressure profiles and the data for 5% nominal load, $Q5$, the observations are more or less identical to those found in the velocity study and therefore it is redundant to present these here. However, it is interesting to notice that for the two sources the distributions are closely related and in both cases the far field power is carried in the structure primarily as torsion and longitudinal vibrations. Thus improvements to accommodate with vibrational demands can be adopted to the pipe wall e.g. in terms of adding damping material or by altering the rigidity in segments of the pipe.

Finally, the power flow analysis can be conducted for the different modal decompositions discussed in section 3.2.4 based on the two Fourier representations. The acoustic load can therefore be introduced through either a_m or b_m rather than c_m and effectively the modal response changes. However, through this study it was found that the power flow is highly insensitive to the source distribution and in fact the applied source seems to govern only the magnitude of the power flow. This is on the other hand also what can be expected as the power flow is an integral representation why the power flow is an integral average of the acoustic power flow across the orifice. On the other hand in the study of the acoustic response (pressure and velocity) the source distribution is essential for the validity of the acoustical field variables, especially in the very near field. The study of source distribution are treated in detail the following.

3.3.2 Source distribution from modal decomposition

Through the power flow study of the previous section the source distribution was introduced by means of the exponential decomposition. In this section it is of interest to discuss whether or not the assumptions related to the exponential decomposition method are correct for the available CFD-data.

As discussed in the previous section there are in general two approaches to decompose the CFD-data. One is based on the trigonometric Fourier formulation and the other on the exponential formulation. This extents to, in general, three decomposition methods, that is, either sine, cosine or exponential Galerkin orthogonalisation. Which of the methods should be applied to get the correct decomposition is therefore depended on the actual distribution of the CFD-data

as the Galerkin orthogonalisation must be conducted with an orthogonalisation weighting of similar shape. As this distribution is not completely known qualified assumptions regarding the distribution need to be taken and dependent on the quality of the assumption it will affect the decomposed result.

If we assume that the circumferential distribution of the CFD-data is distributed by either a sine or a cosine the modal amplitudes are derived by means of similar shaped orthogonalisations and terminates as shown in equation (3.9) where the orthogonal properties of the trigonometric functions are applied to reduce the equation. For a more detailed derivation and description of Galerkin's orthogonalisation method see appendix E.

$$\begin{aligned} &\int_0^{2\pi} \vartheta^{\mathrm{CFD}} \cos(n\theta)\mathrm{d}\theta = \int_0^{2\pi} \sum_{m=0}^{\infty} \vartheta_m^{cos} \cos(m\theta)\cos(n\theta)\mathrm{d}\theta \\ &\Downarrow \\ &\vartheta_m^{cos} = \frac{1}{\varepsilon_m \pi} \int_0^{2\pi} \vartheta^{\mathrm{CFD}} \cos(m\theta)\mathrm{d}\theta \end{aligned} \tag{3.8}$$

where ^{cos} indicates the orthogonalisation procedure used and in the cosine orthogonalisation $\varepsilon_{m=0} = 2$ and $\varepsilon_{m\neq 0} = 1$. In the sine orthogonalisation *cos* is substituted by *sin* and ε_m is 1 for every m. ϑ^{CFD} is the CFD-data and ϑ_m the modal contribution to the CFD response. Notice here that this equation is obviously identical to the equation for the coefficients of the Fourier series shown in (3.7) as it was discussed that the model decomposition is exactly based on its Fourier series representation.

If, on the other hand, a complex exponential distribution is assumed the orthogonalisation look as follows.

$$w_m^{exp} = \frac{1}{2\pi} \int_0^{2\pi} w^{\mathrm{CFD}} \exp(-im\theta)\mathrm{d}\theta \tag{3.9}$$

What may be clear to the reader is that the decomposed amplitudes may differ in phase and in magnitude by a factor of 2 if our assumption regarding the source distribution is wrong. This is an interesting point which to the authors knowledge has never been discussed before and therefore this issue is addressed through a thorough investigation in section 4.5.2.

In the latter derivations of the different decompositions we have only considered continuous functions in θ, however, as the CFD data is discrete in θ the integral can be expressed as a sum just as shown in equation (3.7).

If the velocity field is decomposed at 50Hz for $m = 1$ by means of the three methods we get the radial source distributions as illustrated in figure 3.15 where the imaginary and real part is illustrated separately.

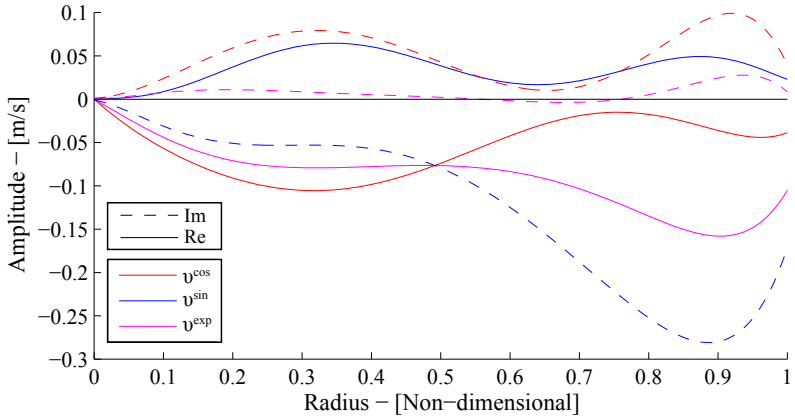

Figure 3.15. Modal decomposition for the velocity field at 50Hz for $m = 1$. Both the imaginary and real part of the cosine (red), sine (blue) and exponential (magna) decomposition is shown.

The task is now to determine which of the distributions that would reflect the actual CFD-data best (or more specifically the actual characteristic of the pump) and apply this in the vibro-acoustic model for further analysis. In this case the conclusion seem straight forward as it is seen that when decomposed by cosine and sine individually both decompositions are non-zero. This immediate imply that the CFD-data is dispersed by an exponential function rather than by an individual cosine/sine function. In fact, it can be seen from the figure that the distribution between sine and cosine term is not uniform hence the distribution is profiled as

$$\vartheta = \sum_{m=0}^{\infty} \left[\vartheta_m^{cos} \cos(n\theta) + \vartheta_m^{sin} \sin(n\theta) \right] \tag{3.10}$$

In this case great advantages can be obtained by applying the exponential decomposition over cosine and sine individually which will be evident from the discussion on modal decomposition in section 4.5.2. Based on the different decompositions Eulers identity reveals a convenient relation between these and for complex valued amplitudes the relation reformulates to the right in equation (3.11).

$$\vartheta_m^{exp} = \frac{\vartheta_m^{cos} - i\vartheta_m^{sin}}{2} \qquad \Leftrightarrow \qquad \vartheta_m^{exp} = \frac{\Re(\vartheta_m^{cos}) + \Im(\vartheta_m^{sin})}{2} + i\frac{\Im(\vartheta_m^{cos}) - \Re(\vartheta_m^{sin})}{2} \tag{3.11}$$

If the distributions shown in figure 3.15 are summed according to (3.11) we arrive exactly at the coefficients found directly by the exponential decomposition. Thus definite consistencies in the decompositions of the CFD-data are observed and it is therefore concluded that the decomposition should, in general, be conducted by means of the exponential decomposition as the CFD-data does not disperse as pure sine or cosine but as a combination. And as just shown this is fully captured by the exponential decomposition because of Euler's identity. In conclusion the radial distribution should be based on ϑ_m^{exp} rather than ϑ_m^{cos} and ϑ_m^{sin} individually as this would provide spurious amplitude and phase information for the vibro-acoustic model which may distort the image and interpretation of the response. Effectively, the velocity potential does not distribute as a pure cosine and the exponential distribution should therefore be adopted. Notice that changing this assumption does not affect the governing equations, only the distribution of the field variables. Nonetheless this conclusion is not final as there might be cases in which caution should be taken confer to the discussion in section 4.5.2.

If this source (magna in figure 3.15) is applied in the vibro-acoustic model we arrive at the power flow graphs shown in the latter figure 3.12. In the following figures 3.16 and 3.17 the acoustic profiles from the model at the excited cross section are shown.

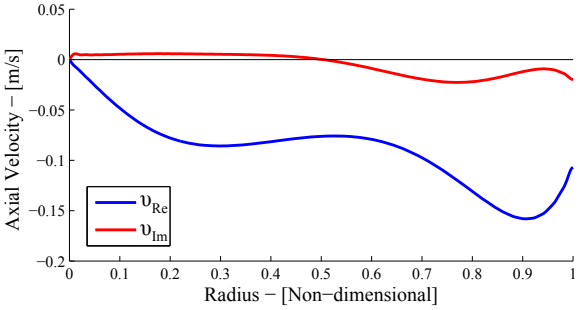

Figure 3.16. Velocity distribution at the excited cross section when loaded by the decomposed velocity source for $f = 50$Hz at $m = 1$ and 100 waves included.

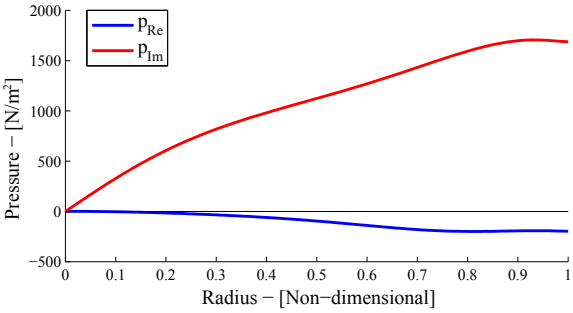

Figure 3.17. Pressure distribution at the excited cross section when loaded by the decomposed velocity source for $f = 50$Hz at $m = 1$ and 100 waves included.

In the figure it is seen that the applied load resembles the velocity profile as expected and for the pressure profile it is seen that the pressure peaks at the shell wall in almost complete anti phase with the velocity source. If the source is on the other hand applied through the decomposed pressure field at the same frequency and circumferential wave-number the acoustic profiles at the excitation cross section distributed as shown in figure 3.18 and 3.19.

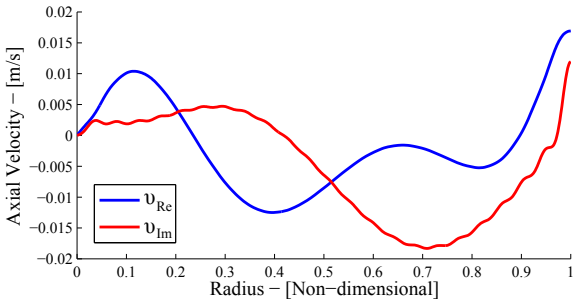

Figure 3.18. Velocity distribution at the excited cross section when loaded by the decomposed pressure source for $f = 50$Hz at $m = 1$ and 50 waves included.

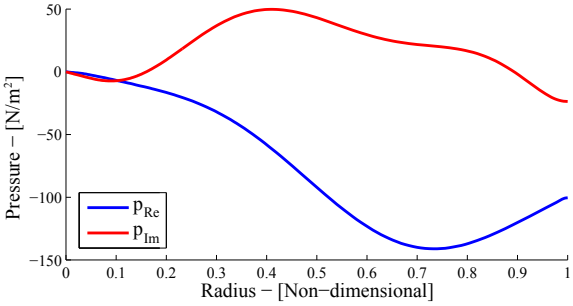

Figure 3.19. Pressure distribution at the excited cross section when loaded by the decomposed pressure source for $f = 50$Hz at $m = 1$ and 50 waves included.

In the right figure it is seen that the pressure distribution does not peak at the shell wall but at approximately $0.75R$ and further that the velocity and pressure field are not in anti-phase in this case. The differences seen when applying a pressure field versus a velocity field imply that there are some inconsistencies between the vibro-acoustic model and the data retrieved from CFD-analysis. If no inconsistencies where present the distributions would have been independent on which source that was applied as both cases would have been identical. On the other hand pitfalls in the modal decomposition could possibly affect the inconsistencies as well however as will be evident through section 4.5.2 this will not be the primary cause. To locate the pitfalls measurements need to be conducted and supposedly inverse method applied as direct measurements are not possible.

3.3.3 Studies for a specific industrial case

Besides the study of the vibro-acoustic performance when subjected to the CFD-data it is interesting from the view point of e.g. product improvements and developments, wave-propagation, wave-reflection etc. to study other things in the available model. This immediately suggest a specific industrial case with a well-defined purpose in mind as the model enables a wide range of possible investigation areas. As the scope of this project is to analyse the vibro-acoustic performance of a pipe when subjected to CFD characteristics and at the moment not to apply the model to improve products thorough investigations are not initiated in this thesis. However, this section serves as a teaser to highlight some of the possibilities enabled by the improvements made on the theory of vibro-acoustic shell theory in this thesis.

First of all it is interesting to study the effect of multiple sources to conclude on the consequences of a phase shift between two or more sources. This is evaluated by adding Green matrix from different source locations and evaluate power flow etc. based on the superposed response. This is made possible by facilitating the bi-orthogonality conditions which allows for explicit formulation of Green's matrix.

Another interesting case is to study the effect of different source locations to conclude on these effects on the total power flow, response, phase between velocity and pressure etc. Based on this study it is possible to determine locations where peak values in the CFD-data are critical and in principle make suggestions to redesigns where peaks at these locations are avoided. This study can be conducted by evaluating e.g. the total power flow at each circumferential wave-number when a unit ring source is applied at several locations along the radius. This study is shown for $f = 1760$Hz in figure 3.20 and for $f = 20$kHz in figure 3.21.

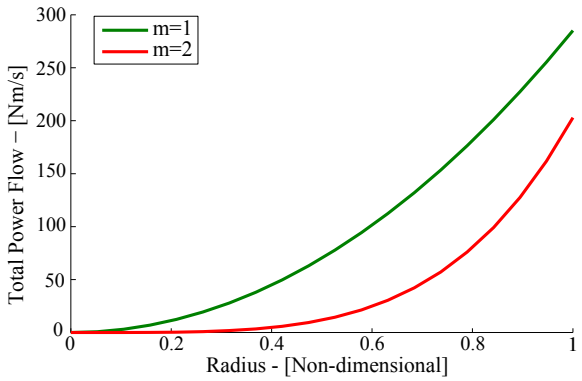

Figure 3.20. Total power flow as a function of source location for different circumferential wave-numbers at $f = 1760$Hz.

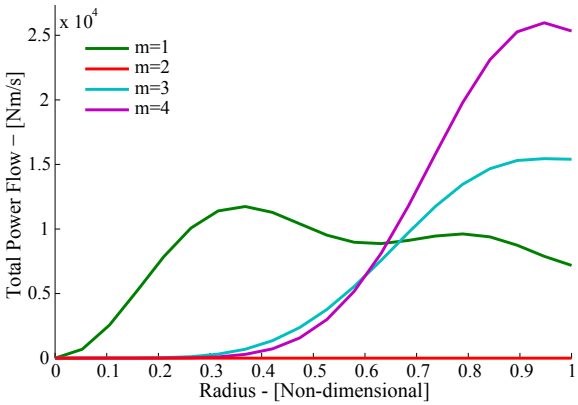

Figure 3.21. Total power flow as a function of source location for different circumferential wave-numbers at $f = 20$kHz.

In this study it is seen that at low frequencies, $f = 1760$Hz, this analysis is trivial as the total power flow is highest for unit sources at the the shell wall. This is also what to expect as the source is profiled as a ring source and as the radius increase the input energy increase. However, as seen at higher frequencies, $f = 20$kHz, this analysis is not trivial as the the low order circumferential wave-numbers starts to deviate and provide higher total power flow for ring sources located at intermediate radii's. Nevertheless, the findings at one frequency might be in total contradiction with the findings at another frequency and as could be imagined this is a very cumbersome task.

Finally, the effects of a boundary layer might also provide important knowledge on e.g. sound emission and the analysis could favorably be extended to include advanced modelling of boundary layer effects e.g. by implementing viscosity effects etc. Similarly, the investigation of differences between applying a pressure source and a velocity source examined in [Ledet et al., 2015] could easily be extended to a more thorough study for a well-defined industrial case.

Experimental approach 4

In this chapter the experimental set-up, the results and the comparison to the vibro-acoustic model is of primary interest. The purpose of conducting experiments on a series of pipes is two fold: 1) It is of great interest to validate the vibro-acoutic model against high quality measurements on pipes used in industrial applications to determine the accuracy and quality of the model. 2) It is the hypothesis that it is possible to determine the shape and intensity of the source by applying an inverse methodology to characterise the source. The idea of the source characterisation is to correct the vibro-acoustic model in comparison with the experimental data.

To keep the attention on validating the model, the experiments are kept as simple as possible and are thus confined to experiments on a finite hollow shell/pipe. When the acoustic medium is included in the experiments the consumed time related to the experimental set-up etc. increase drastically as the sources of error are much more pronounced in such experiments. Similarly, the introduction of acoustical loads, anechoic terminations etc. calls for much more care than if a hollow finite shell is analysed, hence such experiments, given the time frame of this project, will lead the focus away from validating of the model.

4.1 Experimental setup

The experiments are as mentioned conducted on hollow shells and further to avoid possible errors in relation to an anechoic termination it was in collaboration with Grundfos decided to focus on finite shells to ensure a high quality of the results and reduce possible sources of error. In relation the model is improved by means of introducing the Boundary Integral Equation Method (BIEM) to cope with finite cylindrical shells described in section 2.4.

4.1.1 Test specimens

The experiments are conducted for two different pipes of finite length where one pipe is considered thick and the other thin. The geometry and material data for these pipes are shown in table 4.1.

As seen from the table the thick beam-like shell exceeds the thickness-to-radius ratio threshold of $\zeta \leq 0.05$ for an error less than 5% prescribed by the Novozhilov-Gol'denveiser thin shell theory. Effectively this introduce slight complications in relation to the model, however the intend is simply to reduce the complexity by choosing a pipe that will be governed by beam vibration which correspond to the flexural mode, $m = 1$ in the vibro-acoustic shell model. In addition it can also be compared to the simple BE-beam model. Thus for the thick pipe it is only necessary to consider the flexural mode in the comparison with the model and similar this simplification hold several great advantages in simplifying the prove-of-concept of the inverse

	Variable name	Thick shell/ beam	Thin shell	Unit
Geometry				
Radius - Median	R_m	23.15	68.30	mm
Thickness	h	2	1.6	mm
Ratio	$\zeta = \frac{h}{R}$	0.0864	0.02343	-
Length	L	1284.00	743.50	mm
Material - Stainless steel				
Young's modulus	E	~ 180	~ 180	GPa
Poisson's ratio	ν	~ 0.30	~ 0.30	-
Mass	m	2749.50	4067.10	g
Density	ρ_{str}	7360.85	7966.79	kg/m^3
Analysis parameters				
Frequency range	-	0 - 1600	0 - 1600	Hz

Table 4.1. Geometry and material data of the two pipes used throughout the experiments. The density is calculated based on the volume and mass.

source characterisation treated in the upcoming chapter.

4.1.2 Test set-up

For the two pipes tested in this thesis the experimental set-up is illustrated and documented in appendix D. The boundary conditions for the pipes are chosen as free-free conditions are these are relatively easy to mimic in reality. The test set-up is sketched in figure 4.1 and as seen the measurements are conducted with 1.5g accelerometers and the excitation introduced via a modal hammer to measure the input force. Furthermore initial experiments are conducted with a microphone and no accelerometers to evaluate the effects of mass loadings.

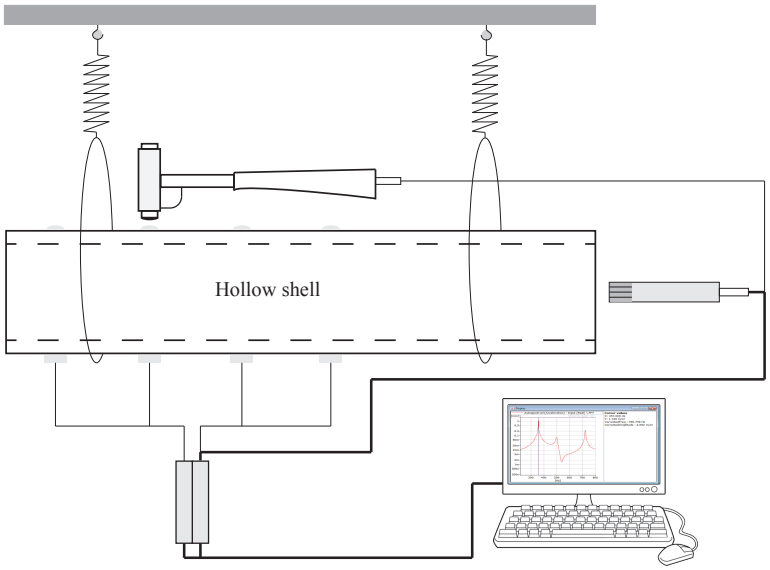

Figure 4.1. Sketch of the test set-up. Figures from [Brüel & Kjær, 2015; Imagbuddy, 2015].

The chosen acceleometer placemetns, excitation and suspension points for the different pipes are illustrated in appendix D.2 in figure D.2 for the thick shell and in figure D.5 for the thin shell. Further a list of components utilised in the experiments are shown in table D.1.
As a final remark recall that the thick shell is expected to vibrate purely in flexural mode and several measurements around the circumference is therefore not needed as decomposition is

trivial. For the thin shell on the other hand this is a necessity.

4.2 Experimental results and interpretation

Through this section chosen results from the experiments are presented for both the thick and thin shell. To verify the other experiments the attention should be drawn to appendix A.5

4.2.1 Thick shell results

The results based on the experiments on the thick shell are shown in figure 4.2 for all five accelerometers with the excitation placed at e_3 according to table D.2. As is seen from the figure all accelerometers capture the same resonance frequency. On the other hand the response in-between the resonances and what is known as the anti-resonances are quite different from accelerometers.

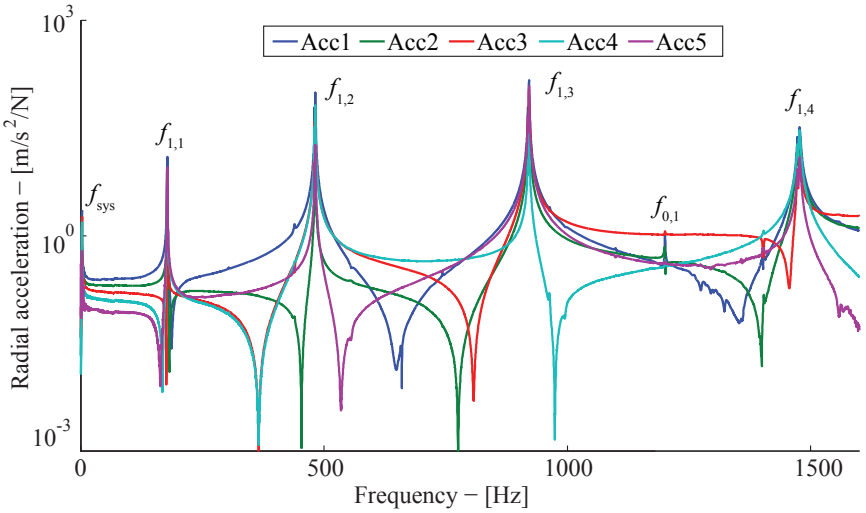

Figure 4.2. Response of all five accelerometers of the thick shell when excited at e_3. The resonances are found at the same locations however with different magnitude.

Notice that at other excitation points (illustrated in appendix A.5) these graphs are slightly different as some modes are excited better at these points, however, in general, throughout all experiments all modes at $m = 1$ are excited sufficiently and the resonance frequencies are found to be the same within no more than ± 0.25Hz between different accelerometers.

If the five measurements at the five locations are averaged the resonances becomes more distinct as seen in figure 4.3. In this case we can locate at least five distinct resonances where one is the system resonance, f_{sys}. Through validation of the mode shapes from the measurements it is confirmed that the remaining four distinct resonances are in fact flexural bending modes; referred to as $f_{m,n}$ where n is the resonance numbering. Similarly this can also be verified through the simple beam model presented in section 4.2.3.

Remark that between $f_{1,3}$ and $f_{1,4}$ there is a slight peak which is difficult from the view point of experiments alone to exclusively characterise as a resonance. However, through a FE-analyse and analysis by the shell model it can be concluded that there is in fact a torsional breathing mode ($m = 0$) resonance in this range. Remark that the accelerometers are not placed for sufficient measurement on this mode and the quality of the experiments are not sufficient to

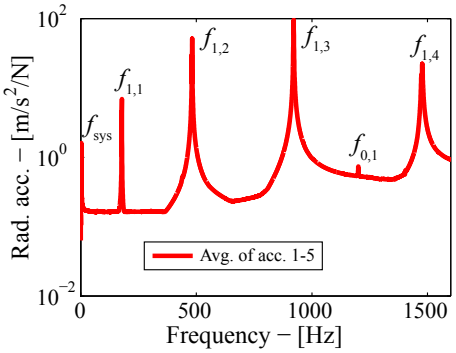

Figure 4.3. Response as an average of all accelerometers when excited at e_3.

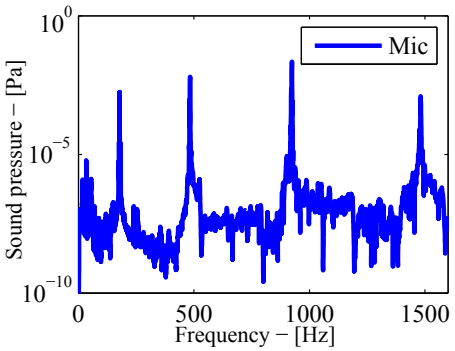

Figure 4.4. Sound pressure measured by the microphone placed at the termination of the pipe when loaded at e_3.

compare with the resonance found in the models. Thus this resonance are not utilized or discussed further in the following.

In figure 4.4 the results from a purely acoustic measurement are shown to determine the effect of mass loading when masses in terms of accelerometers are attached. In comparison of the resonances from the two measurements (with and without accelerometers), shown in table 4.2, it is seen that the mass loading have very little effect on the resonances and thus it is concluded that for this pipe mass loadings are negligible. Based on the non-mass loaded resonances found in figure 4.4 the mass effect when the accelerometers are attached can be approximated as a percentage of the resonances of the non-mass loaded system as shown in equation (4.1).

$$\omega_n^{mass} \approx \sqrt{\frac{m}{m+m_{acc}}}\omega_n = C_{mass}\omega_n \tag{4.1}$$

where C_{mass} is given as below

$$\begin{aligned} &\text{Thick shell - 5 acc.:} && C_{mass} = 0.9986 \approx 0.14\% \\ &\text{Thin shell - 10 acc.:} && C_{mass} = 0.9982 \approx 0.18\% \end{aligned}$$

As mentioned the resonance of the complete experimental set-up can be located in the measurements in the very low frequency range. By analyzing a confined region in the low frequency range as seen in figure 4.5 it is possible to locate this system resonance and in all measurements it is found to $f_{sys} = 2.5$Hz, which is in good agreement with what is estimated in equation (4.2).

$$f_n = \frac{\omega_n}{2\pi} = \frac{1}{2\pi}\sqrt{\frac{k_{eq}}{m}} = \frac{\sqrt{2}}{2\pi}\sqrt{\frac{k}{m}} = \begin{cases} 2.68\text{Hz} & \text{for } f_n^{\text{Thick}} \\ 2.20\text{Hz} & \text{for } f_n^{\text{Thin}} \end{cases} \tag{4.2}$$

In figure 4.6 on the other hand the confined region surrounding the third resonance is shown.

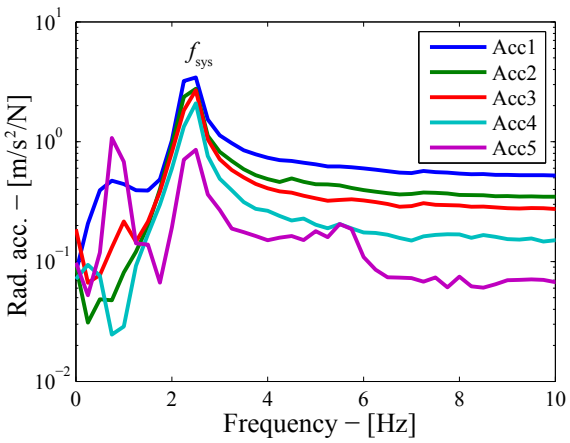

Figure 4.5. Close-up in the low frequency range to locate the system resonance.

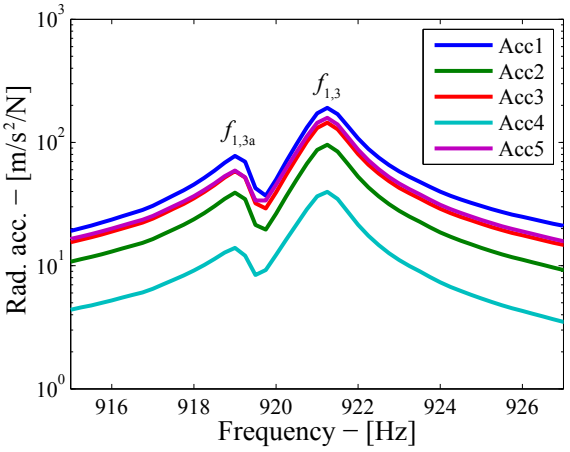

Figure 4.6. Close-up around the third resonance. Two resonances are located here i.e. the pipe is not perfectly symmetric - it contains a seam.

What is seen in the figure is that the measurements capture two very closely located resonances in the same close range. These two resonances has a straightforward interpretation as it is simply a matter of lag of symmetry in the test specimen (the pipe has a seam), i.e. if the pipe has been perfectly symmetric there would still be two resonances, however they would be fully coincident.
To verify this one can simply conduct two simple analysis by any FE-analysis tool; one with a mapped/structured mesh in the circumference and another with a random/free/unstructured mesh. In the latter cases it would be evident that the resonances are not identical to the decimal due to the uneven distribution of the elements.

With the latter discussion in mind every frequency indicated in figure 4.2 does in fact have two non-identical closely located resonances presented in table 4.2. The resonances from the measurements are averaged over all five accelerometers at all excitation locations. The table also presents the microphone measurements without (w/o) accelerometers attached and the resonances calculated from three different models.

	Unit	Vari. bet. acc. 1-5	Average	Micro. w/o acc	BE-model E=174.52 [GPa]	Shell-model E=188.49 [GPa]	ANSYS E=188.49 [GPa]
$f_{0,1}$	Hz	0	(1200.50)	-	-	1223.50	1222.10
$f_{1,1}$	Hz	0	178.00	178.50	172.31	177.50	177.56
$f_{1,1a}$	Hz	0	177.25	177.75			
$f_{1,2}$	Hz	-0.25	482.00	483.50	474.99	481.00	481.33
$f_{1,2a}$	Hz	0	480.50	481.75			
$f_{1,3}$	Hz	0	921.25	924.50	931.16	921.00	921.48
$f_{1,3a}$	Hz	0	919.00	921.25			
$f_{1,4}$	Hz	±0.25	1477.50	1481.50	1539.26	1477.50	1478.30
$f_{1,4a}$	Hz	0	1473.25	1476.50			
f_{sys}	Hz	0	2.50	-	-	-	-

Table 4.2. Resonances measured through experiments and resonances calculated from three different models. Column 3 indicate the maximum deviation between measurements and the average resonances. Young's modulus used in the different models are fitted by a least square method described further in section 4.2.3.

In the table the third column indicate the maximum deviation magnitude in Hz between the different measurements and the average value i.e. 0 means that the resonances from all accelerometers and all excitations point are identical. Furthermore Young's modulus are fitted for the individual models to achieve the best possible match between measurements and model resonances. This procedure, its validity and justifications are described further in section 4.2.3.

4.2.2 Thin shell results

For the thin shell the response measured for accelerometer 1 to 5 at the first circumference, c_1, when excited on top of accelerometer 1 at the same circumference (accelerometer 1 is attached inside the pipe - see figure D.7) is shown in figure 4.7. Notice that this is the complete response hence corresponding to the summation of all modes.

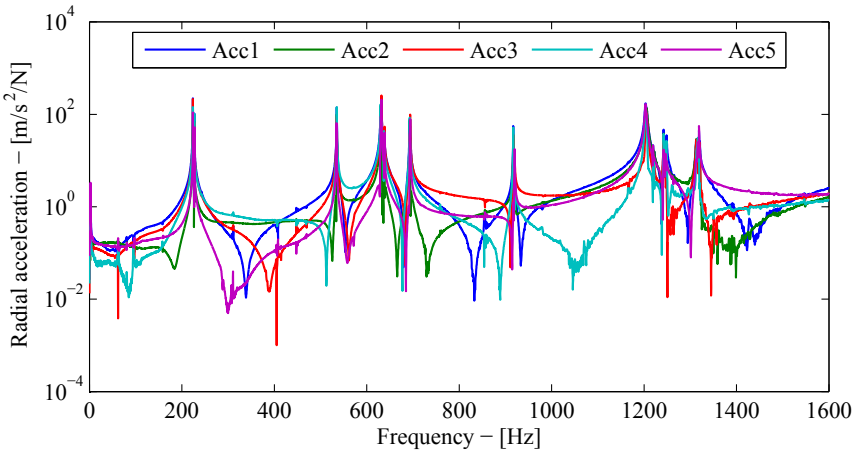

Figure 4.7. Response of accelerometer 1 to 5 at the first circumference, c_1 when excited at accelerometer 1. By further investigation it is found that many of the resonances in the figure contains several closely located modal resonances. Furthermore this cross section does not capture flexural resonances well.

Similar the results for accelerometer 1-5 at the second circumference is shown in 4.8.

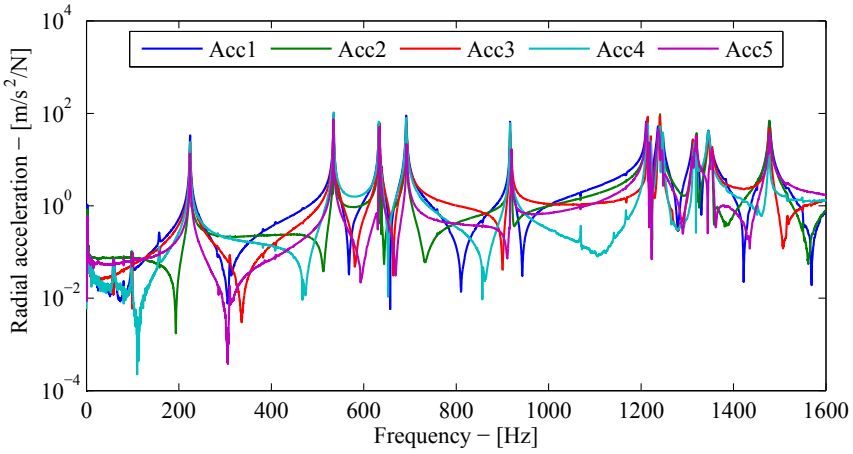

Figure 4.8. Response of accelerometer 1 to 5 at the second circumference, c_2 when excited at accelerometer 1. This cross section is generally better for measurements than c_1 as the modes are excited and measured better here. However a single $m = 2$ mode is missed at this location.

The on the above figures it is seen that the second cross section is generally better for measured the response and resonances as the modes are better excited and measured at this located over

the first cross section. This is clearly seen in the frequency range 1200-1600Hz where the first figure does not capture all resonances primarily the higher order modes of $m = 3$ and 4. Unfortunately the location of this cross section collide with the stationary points of the fifth mode of $m = 3$ and 4 and the specific resonances are thus not captured. For the second cross section on the other hand the second resonance of mode $m = 2$ are not captured which is then captured at the first cross section.

This may be even more pronounced when considering the average response of all 10 accelerometers in the circumference. In figure 4.9 the average is shown for c_1 and in figure 4.10 for c_2.

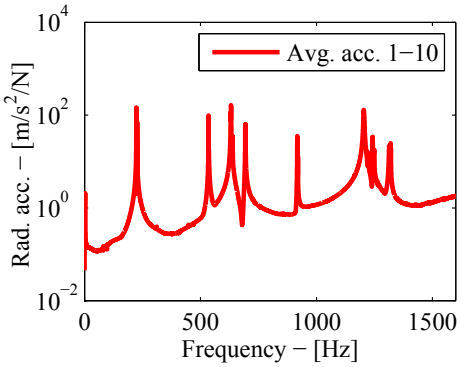

Figure 4.9. Average of the 10 accelerometers for measurements at the first circumference, c_1.

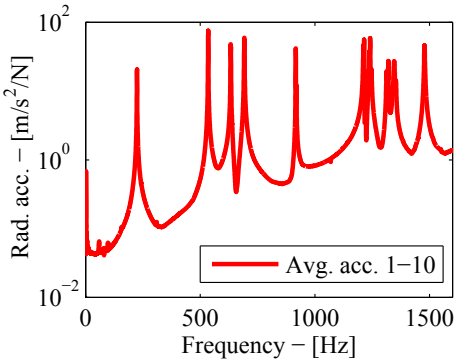

Figure 4.10. Average of the 10 accelerometers for measurements at the second circumference, c_2.

Again it is clear that the first circumference does not capture the higher order modes and resonances and from the figures it is missing at least three branches of resonances. However, by further inspection of the resonance peaks and the in comparison with the an ANSYS and the vibro-acoustic model it is found that the branches shown the latter figures include several modal resonances and in fact there are 15 resonances in the specified frequency range but only 10 peaks are visible in the figures. To visualize the deformation shape of the different resonances at different modes these are animated in appendix A.2 for selected resonances.

The experimental measured resonances can be distinguished into modal resonances by means of model decomposition of the experimental data. This procedure is described in section 4.3 and the results and spotted modal resonances are shown in table 4.3 together with the predictions from ANSYS and the vibro-acoustic model. Notice that similar to the thick shell Young's modulus has been fitted in a least square optimisation for the best fit on all resonances. As seen from the table the coherence between the experimental results and the predictions from the models are indeed very good with a maximum relative error between the shell model and the experiments of only 0.77%. Thus it can be concluded that the model does reflect the physical behaviour of the vibrating hollow shell very well.

Regarding the fitting procedure it would obviously be favourable to verify the value of the modulus through experiments but it is nevertheless expected that the findings would be similar to those fitting for the to test specimens as, according to the table above, all the resonances are fitted very well and all within the same order of accuracy. Further it also seems reasonable based on the density differences presented in table 4.1 that Young's modulus would be slightly larger for thin shell. As a concluding remark it is also worth mentioning that for increasing mesh densities in the ANSYS model the resonances converges towards the resonances of the

	Unit	Exp. Circ2 1 acc.	Exp. Circ2 10 acc.	Shell-model E=205.11 [GPa]	ANSYS E=205.11 [GPa]	Rel. Err. wrt. Shell-model (1 acc.)
$f_{1,1}$	Hz	1315.25	1312.50	1325.50	1325.60	0.77%
$f_{2,1}$	Hz	224.50	224.50	224.50	224.66	0%
$f_{2,2}$	Hz	(c_1) 227.25	(c_1) 227.25	227.75	227.67	0.11%
$f_{2,3}$	Hz	536.00	535.00	537.50	537.64	0.28%
$f_{2,4}$	Hz	1247.00	1246.25	1255.50	1255.50	0.68%
$f_{3,1}$	Hz	635.50	634.50	635.25	635.13	-0.04%
$f_{3,2}$	Hz	638.25	638.25	639.00	638.84	0.12%
$f_{3,3}$	Hz	693.50	692.75	695.25	694.88	0.25%
$f_{3,4}$	Hz	920.75	920.00	921.75	921.45	0.11%
$f_{3,5}$	Hz	1358.25	1353.50	1361.00	1360.90	0.20%
$f_{4,1}$	Hz	1216.00	1214.50	1218.00	1217.00	0.16%
$f_{4,2}$	Hz	1221.75	1221.50	1221.75	1220.70	0%
$f_{4,3}$	Hz	1245.50	1241.00	1247.25	1246.00	0.14%
$f_{4,4}$	Hz	1321.50	1320.25	1322.00	1320.80	0.04%
$f_{4,5}$	Hz	1482.00	1479.50	1485.75	1484.50	0.25%
f_{sys}	Hz	2.50	2.50	-	-	

Table 4.3. Resonances measured through experiments and resonances calculated from two different models. Young's modulus are fitted by a least square method described further in section 4.2.3 and the resonances are determined based on the modal decomposition method described in section 4.3. (c_1) indicates that the resonances are found at the first circumference instead.

vibro-acoustic model which suggests that the shell-model can be considered the exact solution.

Finally, it should be noted that both the system resonance and the asymmetric properties of the pipe are present in the measurements for the thin shell as well and are analysed in the same manner as for the thick shell. This is nonetheless not presented in figures or table in the thesis as it is of no further interest at the moment.

4.2.3 Interpretation of experimental data

The interest of this section deals with how to apply data handling to adjust the model to the experimental data and similar how to adjust the experimental data to cope with the model assumptions of decomposed modes. Initially, we treat how to fit the model to the experiments here by means of fitting Young's modulus in the model to increase the coherence between model and experiments and further how to distinguish resonances caused by an imperfect test specimen to the resonances of the perfect specimen. Finally, the experimental data is fitted to cope with the assumption of the shell model here by means of modal decomposition.

Determining Young's modulus

In comparison between experiments and models several parameters are involved and in general their uncertainties will affect the coherence between the model and experiments. Thus in principle all material and geometry parameters of the test specimens should be determined through experiments as well. However, to avoid needless laboratory hours standard values are often used. As can be imagined this may lead to spurious aggravated coherence between model and experiments hence extensive uncertainty or sensitivity studies may be needed to draw any final conclusions.

To reduce the uncertainties on the material parameters in these experiments a simple inverse methodology is adapted. The idea of this methodology is simply to fit uncertain model parameters such that the coherence between the model and the experiments are improved. In this case it is obvious that the fitting parameters cannot be chosen arbitrary as the fitted results should still retain its solid physical content. Thus fitting all parameters outside of manufacturing tolerances is prohibited. On the other hand it is good practice to fit parameters that are not directly available e.g. parameters such as; Young's modulus and Poisson's ratio and not parameters that are readily available such as; radius, wall thickness, length or weight that can be measured fairly accurate by simple remedies.

For the vibro-acoustic model and the test specimens used in this project the fitting is based solely on Young's modulus as Poisson's ratio has minimal effect on the placement of the resonances. Through this inverse methodology the bounds for the modulus are chosen as $\pm 10\%$ of the standard Young's modulus of 193GPa for stainless steel, [AK Steel, 2015]; making the fitting interval 174GPa$\leq E \leq$212GPa.

The fitting is based on a least square optimisation solve by the pre-implemented optimisation algorithm *fmincon* in MATLAB. The fitting procedure is conducted for both shell and on all resonances present in the experimental data in the frequency spectrum of interest. For the thick shell fitting is furthermore conducted for a simple Bernoulli-Euler (BE) beam model and for the vibro-acoustic shell-model.

The objective formulations for both models are seen in equation (4.3) and the results from the fitting procedure are used in the comparison tables 4.2 and 4.3 and are shown in the header. Remark likewise that the results from ANSYS are based on the modulus fitted from the shell-model.

$$\begin{aligned} \textbf{BE-model:} \quad & \min_E \sum_{n=1}^{N} \left(\frac{f_n^{exp} - f_n^{BE}(E)}{f_n^{exp}} \right)_{m=1}^2 \quad \text{for} \quad 174\text{GPa} \leq E \leq 212\text{GPa} \\ & \qquad\qquad\qquad\qquad\qquad\qquad\qquad\qquad\qquad\qquad\qquad\qquad \wedge \\ \textbf{Shell-model:} \quad & \min_E \sum_{n=1}^{N} \det \left[\mathbf{B_{IEM}}(f_n^{exp}) \right]_{m=0,\ldots,\infty}^2 \quad\qquad\qquad\qquad\qquad 0\text{Hz} \leq f \leq 1600\text{Hz} \end{aligned} \tag{4.3}$$

where f_n^{exp} and f_n^{BE} are the n^{th} resonance of the experiments and the BE-model, N is the number of resonances present in the chosen frequency spectrum and the $\mathbf{B_{IEM}}$ is the E-dependent force/displacement coefficient matrix derived from Somigliana's identities and the boundary conditions as presented section 2.4.

Notice that the BE-model is fitted by means of minimizing the relative error. Alternatively this can be done by minimizing the residual (the classical least-square formulation), however in this case Young's modulus would more or less be chosen to that making the two largest resonances identical as this residual will obviously be larger than between the lowest resonances for a constant relative error. Thus it does not make sense to fit by means of the classical least square formulation.

As a concluding remark it should be strongly emphasized that this inverse methodology makes sense if and only if we are confident that our model will reflect the results of the experiments sufficiently, meaning that even though good results may be obtained by fitting poor models we lose the physical content of the model, why generalising or reusing the fitted parameters in more complex models may have fatal consequences. In conclusion it is of crucial importance

that the physical content is kept and that the fitting parameters are carefully chosen when we wish to generalise results retrieved from inverse methods.

Through this fitting by a single material parameter it is indeed confirmed from the results in the comparison tables that the models reflect the actual behavior of the hollow shell very well for all resonances and the used of an inverse methodology can therefore be fully justified.

Locating the resonances for the perfect pipe

As discussed in section 4.2.1 the lag of symmetry causes two coincident resonances to split into two individual resonances located close to each other. The idea of this section is thus to determine which of the resonances that will be closest to those for a perfectly symmetric pipe and which are governed by the missing symmetry of the pipe. During this brief investigation it is assumed that one of the two resonances will correspond to that of a perfect pipe such that the missing symmetry is assumed to be fully represented by either one of the two closely located resonances.

The idea of this investigation is rather straightforward and is once again based on the principle of inverse modelling. Thus it is assumed that given the correct physical parameters the model will give the exact resonances for a perfect pipe. Now, by conducting the same least square fit as formulated in the bottom equation of (4.3) for every possible combination of the resonances presented in table 4.2 the resonances corresponding to those of the perfect pipe are found as the combination for which the minimised function value is lowest. Thus the combination from which the fit solely based on Young's modulus is closest to the resonances of the model must be the resonances which are closest to the those of a perfect pipe.

Through this investigation the combination which gives the lowest minimized function values is shown in equation (4.4) and these resonances are thus interpreted as those closest to those for a perfect pipe.

$$f = \lfloor 177.25 \quad 480.50 \quad 921.25 \quad 1477.50 \rfloor \tag{4.4}$$

If these experimental resonances are compared to those predicted by the shell or ANSYS model it is seen that the coherence is indeed good and for the shell model all resonances are captured within an accuracy of ± 0.25Hz for the thick shell and within 0.77% for the thin shell. For the BE-model on the other hand the results are slightly off with an increasing relative error as the resonance frequency increases. Similarly this investigation is also conducted for the thin shell and the result is the resonances shown in table 4.3.

4.3 Source characterisation of experimental data by modal decomposition

As mentioned earlier different proposals for conducting the modal decomposition exists but in general they are all based on the same mathematical formulation. In this thesis three methods are compared to investigate the deviation when applying the experimentally simpler methods and likewise to conclude which assumptions are easiest to cope with from an experimental view point. The methods used in the modal decomposition of this thesis are completely analogue to the modal decomposition of CFD-data, why several details will be left out in the following description of the methods.

The different methods are obviously treated in different papers however in the thesis by Brian O. Olsen [Olsen, 2001] a brief overview of three methods are given. In the thesis by Brian the decomposition is conducted by measuring at evenly distributed point around the circumference by the same accelerometer i.e. $2(\widetilde{m}+1)$ experiments must be conducted at each circumference. In this thesis measurements are in one case done in real time through a single experiment by placing 10 accelerometers evenly in the circumference at a given cross section excited at a given point and in another case with one accelerometer fixed and the excitation point moved around the circumference. In the latter case $2(\widetilde{m}+1)$ experiments are necessary as well. Obviously these methods contains individual pros and cons such as increased mass loading effects in the first case and measurement/excitation deviations in the second, why the intend of this investigation is to conclude on which method is best with respect to sources of error in the experimental set-up.

The governing assumption in the modal decomposition is similar to that for the CFD-data decomposition and likewise similar to that for the governing equations, namely that the complete response can be represented as a periodic summation of the individual circumferential modes - a Fourier series - exactly as it was introduced when deriving the governing equation for the Novozhilov Gol'denveiser thin shell theory. Effectively, this leads to a very simple decomposition namely a simple FFT in the circumferential direction exactly as it is done for each circumferential grid-line in section 3.2.4. Recall then that the discrete amplitudes retrieved from the FFT corresponds to the discrete amplitudes of the Fourier series.

The latter methodologies are thus based on evenly distributed measurement points in the circumference and furthermore a minimum number of measurement points of $2(\widetilde{m}+1)$ to cope with Nyquists sampling theorem and avoid aliasing. This methodology is adapted to the real time measurement of 10 accelerometers evenly distributed in the circumference and is referred to as method 1 (**MD1**). Again this methodology is adapted for the 10 measurements with only one accelerometer at a fixed location and a moving excitation point and is referred to as method 3 (**MD3**). For an elaborated view on this modal Fourier representation of the experimental data the attention is to be directed towards the literature, [Olsen, 2001]. However, it is nonetheless suggested to introduce the decomposition as a complex summation of exponentials rather than by a summation of trigonometric functions as in (4.5), as this will cause errors in the sign of the complex amplitudes even though the modules will be similar.

To extract an additional method we can on the other hand make use of the symmetric and anti-symmetric properties governing the circumferential modal deformation of a vibrating shell. This has three immediate advantages; 1) the number of necessary measurement points are reduced by a factor of two, 2) no aliasing will occur and 3) the decomposition is by no means different from that proposed above if the measured pipe is in fact perfectly symmetric and in effect this method depends on the symmetry properties of the test specimen. This method was proposed by [Feng, 1996] and is again done by representing the modes as a periodic summation such that

$$H_i = \sum_{m=0}^{N-1} A_m \cos(m\theta_i) \qquad \text{with} \quad \theta_i = \frac{\pi i}{N} \tag{4.5}$$

where H_i is the measured mobility function at point i, A_m the modal amplitudes and N the number of measurement (or excitation) points around the circumference.

Now, carrying out the summation and utilising symmetry and anti-symmetry the equation

system is split up into even and odd modes simple by alternately adding and subtracting symmetrically placed measurements as shown in equation (4.6).

$$\begin{Bmatrix} H_0 + H_5 \\ H_1 + H_4 \\ H_2 + H_3 \end{Bmatrix} = \begin{bmatrix} 2 & 2 & 2 \\ 2 & 2\cos\left(\frac{2\pi}{5}\right) & 2\cos\left(\frac{4\pi}{5}\right) \\ 2 & 2\cos\left(\frac{4\pi}{5}\right) & 2\cos\left(\frac{8\pi}{5}\right) \end{bmatrix} \begin{Bmatrix} A_0 \\ A_2 \\ A_4 \end{Bmatrix}$$
$$\begin{Bmatrix} H_0 - H_5 \\ H_1 - H_4 \\ H_2 - H_3 \end{Bmatrix} = \begin{bmatrix} 2 & 2 & 2 \\ 2\cos\left(\frac{\pi}{5}\right) & 2\cos\left(\frac{3\pi}{5}\right) & -2 \\ 2\cos\left(\frac{2\pi}{5}\right) & 2\cos\left(\frac{6\pi}{5}\right) & 2 \end{bmatrix} \begin{Bmatrix} A_1 \\ A_3 \\ A_5 \end{Bmatrix} \tag{4.6}$$

This methodology can also be adapted for the sine part to get complex amplitudes with phase information included. This method involving the symmetry considerations are referred to as method 2 (**MD2**) when the mobility functions are taken from the experiments with all 10 accelerometers attached.
In fact a fourth method can be constructed again by adapting the symmetry considerations but instead with the mobility functions from the one accelerometer measurements. This fourth method is however not treated further in the following as the conclusions will effectively be similar to those of MD1 and MD2.

Finally, it is important to note that if the sine part of the modal decomposed experimental data is non-zero it indicates that the radial displacement is not dispersed according to the assumption in the derivation of the governing equation. Thus the ansatz could advantageously have be chosen as $w(\theta) = \sum_{m=0}^{\widetilde{m}} W_m \exp(im\theta)$ rather than $w(\theta) = \sum_{m=0}^{\widetilde{m}} W_m \cos(m\theta)$ to improve the model further.

In conclusion the three proposed methods are theoretically identical but holds different pros and cons from the view point of practical application. It is therefore of great interest to investigate if one method is better than the others as it is expected that the quality of the decomposition is highly important for the quality of the further conclusions on validation and source characterisation. This will be treated in the following.

4.3.1 Comparison of modal decomposition methods

In the following comparison of the modal decomposition methods the comparison is limited to cross section 2 (as the modes are measured best here) excited at the location of accelerometer 1 (for MD1 and MD3) which is taken as the reference point, $\theta = 0$. Similarly to avoid possible aliasing issues only the first 5 circumferential modes are considered, $m = 0, \ldots, 4$.

In figure 4.11 the decomposition for all three methods are shown for the fifth decomposed mode, $m = 4$.

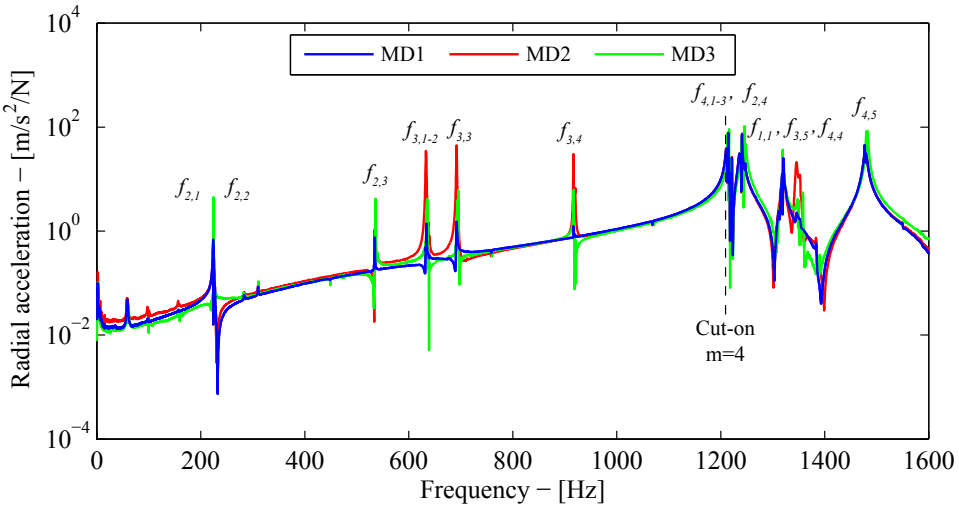

Figure 4.11. The experimental data decomposed into the response at $m = 4$ for the second circumference by means of the three methods. As illustrated the decomposed data suffers from modal leakage or spurious response caused by e.g. lag of symmetry in the shell and experimental error sources.

Based on this figure several interesting things should be noticed.

1. The first cut-on frequency for $m = 4$ is located at approximately $f = 1200$Hz which indicate that the modal decomposition illustrated in the figure is rather poor as it contains quite a few spurious resonances at low frequencies below cut-on where no resonances can be present. Similarly, spurious resonances are also present for frequencies above cut-on.

   These spurious resonances are a consequence of modal leakage in the modal decomposition which is an issue related to the number of governing mode in the measured response (elaobrated later) and experimental error sources e.g. accelerometer and excitation placement, accelerometer noise, surface measures rather than point measures etc.
2. The modal decomposition from MD1 seems to be best as the amplitudes of the spurious resonances are smallest and are thus easier to distinguish from the actual resonances.
3. In principle it is "impossible" to distinguish the modal resonances without having a comparable model as the modal leakage introduce spurious responses with such large amplitudes that it is difficult to judge the modal nature of these resonances.

If the decomposed data is viewed in the confined frequency spectrum near the cut-on frequency shown in figure 4.12 it is known through analysis that this spectrum includes two resonance related to $m = 4$. Again several interesting things should be noticed in this spectrum.

1. In MD1 and MD2 the experiments are conducted with 10 accelerometers attached and in MD3 with only one accelerometer attached which causes the resonances of MD3 to be shifted by approximately 1-2Hz to the right of MD1 and MD2 as a consequence of the added mass. This is in good agreement with the predictions shown in equation (4.1) where the shift is estimated to approximately 2.2Hz.
2. MD1 and MD2 are almost identical which suggests that at the resonances at low frequencies and lower order modes the lag of symmetry is not captured in the measurements as this specific mode will indeed govern the response at this frequency.
3. The double resonances caused by the lag of symmetry from the longitudinal seam in the pipe appears clearly in the figure as well.

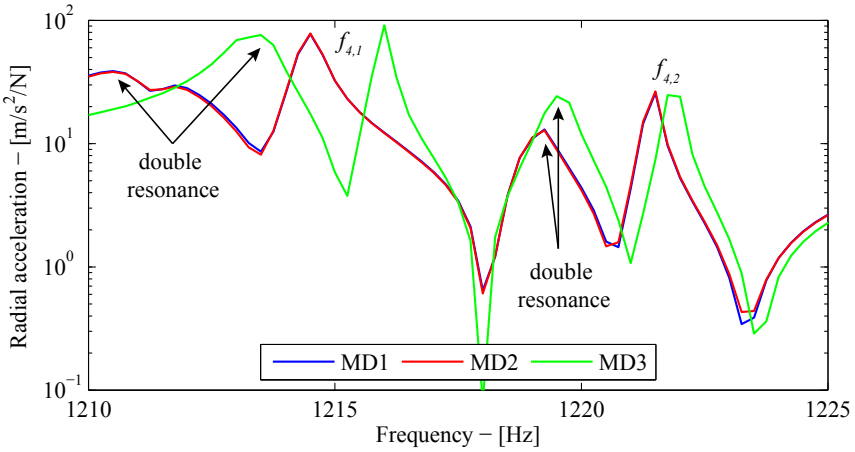

Figure 4.12. Confined frequency spectrum of figure 4.11 near the cut-on frequency. As illustrated MD1 and MD2 coincide at the resonances which indicate that these are in fact modal resonances of $m = 4$. Furthermore they are slightly shifted from MD3 which is a consequence of the additional mass from the 10 accelerometers. Notice also the double resonances caused by lag of symmetry.

The task for the modal decomposed data is now first of all to sort out the spurious resonances such that the individual modal resonances can be properly distinguished. This tasks is however not as straightforward as expected because the modal decomposition has proven to be much more impaired than expected. Fortunately in most cases good models that can predict these behaviours are available and we may be able to distinguish the resonances by help of these. On the other hand if models are not available or as in this case the resonances of individual and different circumferential modes are very closely located it is still difficult to determine which resonance belongs to which circumferential mode.

However, within the specific modal resonances it is well-known that the response will be governed by the response of that specific mode and in the ideal case this would be fully caught by the modal decomposition. Nevertheless errors in the set-up, measurements, placements etc. causes the presence of modal leakage in the decomposed modes and the division of resonances into specific modes becomes difficult. A way to overcome this and accurately categorize the resonances is to compare the results from two different methods where one facilitates the symmetry properties of the shell vibration.

When such two methods are applied to the same set of data there will be good coherence between the methods where specific modes are governing the response while the coherence is compromised elsewhere due to assumption violations. Thus by demanding the symmetric properties of the vibrations in the modal decomposition it becomes clear which of the resonances that in fact belongs to the specific modes. This is illustrated in figure 4.12 for $m = 4$ from which it is clear that the amplitudes of the two methods are more or less identical when the resonance belongs to the fourth mode while in figure 4.13 at a spurious resonances of the fourth mode the coherence of the decomposed amplitudes for the two methods are controversial even though the shape characteristics are similar. This phenomenon is observed for every mode in the desired range, $m = 0, \ldots, 4$.

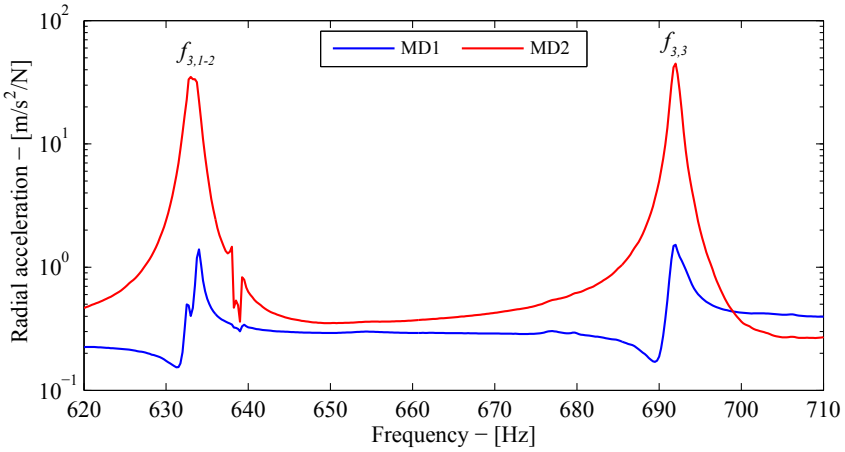

Figure 4.13. Spurious resonances from figure 4.11 caused by modal leakage. When amplitudes of the decomposed data from MD1 and MD2 are not similar the resonances are spurious and does not belong to this mode.

As seen from the above figure in comparison with figure 4.12 it is indeed very easy to distinguish the modal resonances simply by facilitating two similar methods based on the same mathematical formulations but different assumptions. The idea is simply that for MD1 imperfect pipes are somewhat accounted for while in MD2 perfectly symmetry pipes are assumed and consequently the results does only match at the resonances where a single mode is governing. Further it should be noticed that no additional experiments are needed as it is just a matter of applying different assumptions to the same data and search for their similarities. Notice also that this methodology can be applied for MD3 (and MD4) as well by adopting symmetry in the exact same way.

Thus in conclusion this proposed method will be completely valid as long as the pipe holds the slightest imperfections whether it is the pipe itself or caused by uncertainties in accelerometer placements, noise, excitation points etc. If the pipe and set-up on the other hand is completely perfect the modal decomposition can be conducted without any concerns and independent of the method used the results would be identical.

4.4 Comparison between experimental and model reponse

In this section it is intended to compare the modal response calculated in the vibro-acoustic model with the response obtained through modal decomposition of the experiments. Initially, the thick shell comparison is conducted and subsequently the thin shell comparison.

Through this comparison the results for different scalings are presented. Typically, the scaling between the model and experimental results is unique, however as different approaches and assumptions can be applied the scaling will differ according to the assumption. The discussion related to the different scaling procedures are saved for section 4.5.1 and only the results from the different approaches are presented in the following.

4.4.1 Thick shell comparison

As mentioned the experiments are conducted for two different pipes chosen to cope with different purposes. The thick pipe violates the assumption for a thin shell and the vibro-acoustic model is therefore not completely tuned to assess this response in detail. Nonetheless

this pipe is chosen because it resembles more or less a free-free beam, why the experimental results are also directly comparable to the simple BE-beam model. Furthermore this allow us to reduce the shell model to only consider the flexural mode, $m = 1$, in the comparison and modal decomposition is avoided. Thus confer to these simplifications the shell model at $m = 1$ is expected to exhibit good results with respect to the raw data from the experiments.

In the following comparison between the thick shell only the results are illustrated when both the model and experiments are excited and measured at point 5, see appendix D.2 for locations. The comparison for three different scalings of the thick shell model are illustrated in the following. In figure 4.14 the comparison is shown with the scaling in the model given as: $\frac{R}{\pi}$.

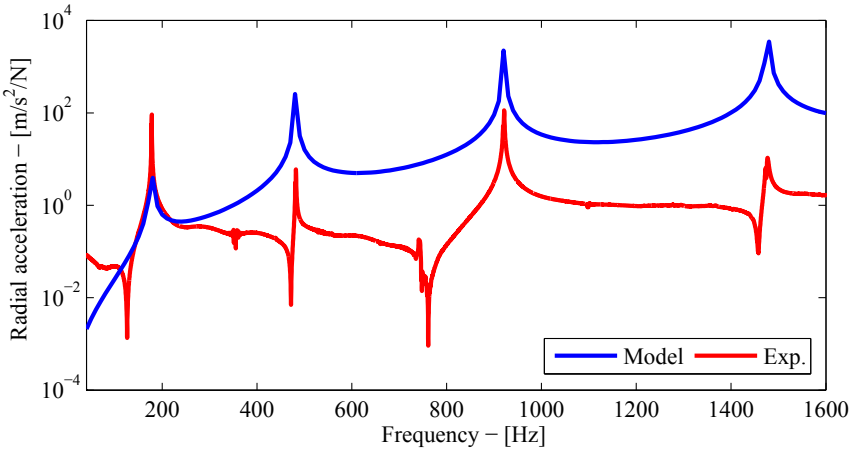

Figure 4.14. Comparison between the raw experimental data and the model for the thick shell at $m = 1$ and a model-scaling of $\frac{R}{\pi}$. Measurement and excitation in the model and experiment is located at point 5 according to table D.2. Resolution in Exp. is 0.25Hz and 1Hz in the model.

As seen from the figure the characteristics of the graphs are indeed similar however the model seems to produce a larger response at the higher frequencies. Nonetheless in the low frequency range up to approximately 300Hz the resemblance between the model and experiments is excellent. Furthermore it should be noted that the resonances predicted in the model for $m = 1$ predicts all the measured resonances and the purely flexural vibration assumption is therefore confirmed.

If the model is further scaled by the force spectrum at each frequency such that the scaling is $\sqrt{P_{inp}}\frac{R}{\pi}$ where P_{inp} is the power spectrum, [N^2] (the force spectrum measured in the experiments is printed to a text file as power, N^2) the coherence between the model and experiments improve significantly as shown in figure 4.15 and if scaled only with the power spectrum P_{inp} the resemblances is as seen in figure 4.16.

In general it is seen from the latter figures that the resemblance is excellent when the model is scaled with the force spectrum is some way. It is thus concluded that for this thick shell the model does indeed reflect the physical behavior of the thick pipe very well even though there are still some unresolved scaling issues present. Furthermore it is concluded that the scaling used in figure 4.15 provide the best results when compared to the results from other locations and excitations points.

Finally, it should be noted that as no damping is introduced in terms of an imaginary part of Young's modulus the amplitudes at the resonances are singular which is easily verified by

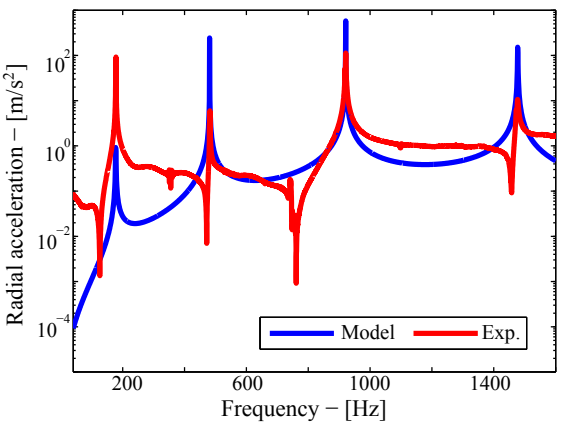

Figure 4.15. Comparison between the raw experimental data and the model for the thick shell at $m = 1$ and a model scaling of $\sqrt{P_{inp}}\frac{R}{\pi}$. Resolution in Exp. is 0.25Hz and 1Hz in the model.

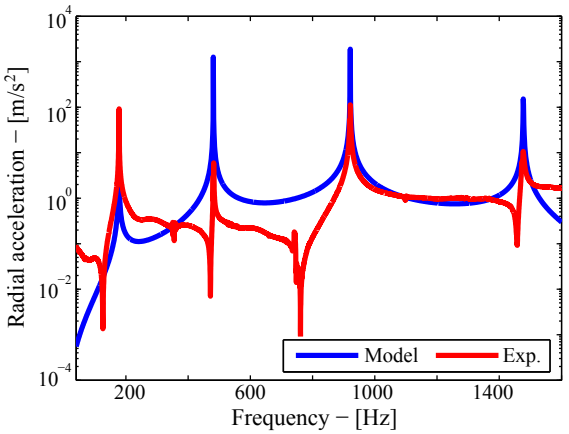

Figure 4.16. Comparison between the raw experimental data and the model for the thick shell at $m = 1$ and a model scaling of P_{Inp}. Resolution in Exp. is 0.25Hz and 1Hz in the model.

decreasing the frequency resolution in the model.

4.4.2 Thin shell results

In the comparison of the results for the thin shell the response is decomposed into the modal response according to the methods proposed in section 4.3. In the following comparison we only consider the results obtained from measurements at the second circumference as the modes are excited best at this cross section. Further, as for the thick shell different scalings of the model are compared to the experimental data. The discussion and justification for the different scalings are discussed further in section 4.5.1.

In figure 4.17 the decomposed data for $m = 1$ decomposed by method MD1 is compared to the response calculated in the vibro-acoustic model when scaled similar to those presented for the thick shell.

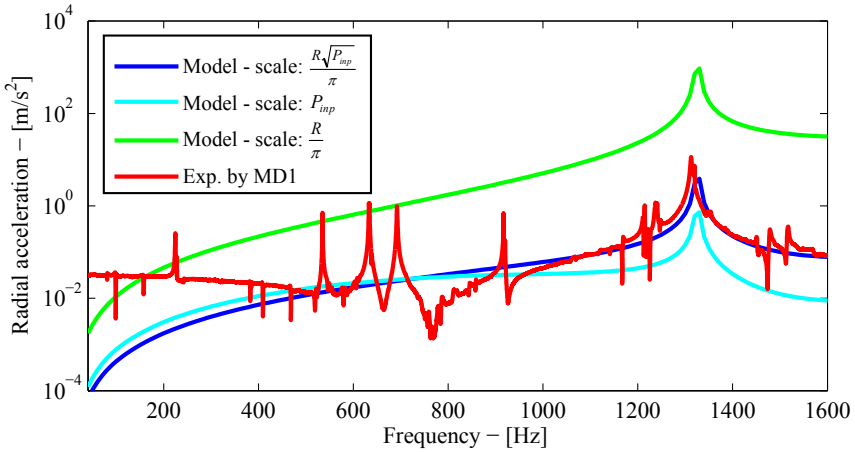

Figure 4.17. Comparison between the modal decomposed experimental data decomposed by MD1 and the model for the thin shell at $m = 1$ with different scalings applied.

From this figure it is evident that the scaling with: $\frac{R\sqrt{P_{inp}}}{\pi}$ provide the best results just as for the thick shell. However, it is clearly seen that the decomposition suffers from modal leakage as peaks from other modal resonances are present in the data despite it is decomposed. How

to improve the modal decomposition and the observed pitfalls of the method found through a thorough investigation is further discussed in section 4.5. Nonetheless the results are considered adequate as the primary cause for deviations is suspected to originate from poor decomposition properties.

If we on the other hand facilitate the force spectrum retrieved from MD3 (where the measurements are conducted at one fixed point and the excitation is moved around the circumference) to decompose the force spectrum into unique modal force spectrum's for each mode and scale the model with this modal spectrum the coherence between the model and experiments improve significantly as seen in figure 4.18 and 4.19.

In these figures the model with a scaling of $\sqrt{P_{modal}}\frac{R}{\pi}$ and $\sqrt{P_{modal}}\frac{h}{\pi}$, respectively, is compared to the experimental data decomposed by MD2 and scaled by its modal force spectrum, $\sqrt{P_{modal}}$ to get $\frac{m}{s^2}$ instead of $\frac{m}{s^2 N}$ for the amplitudes.

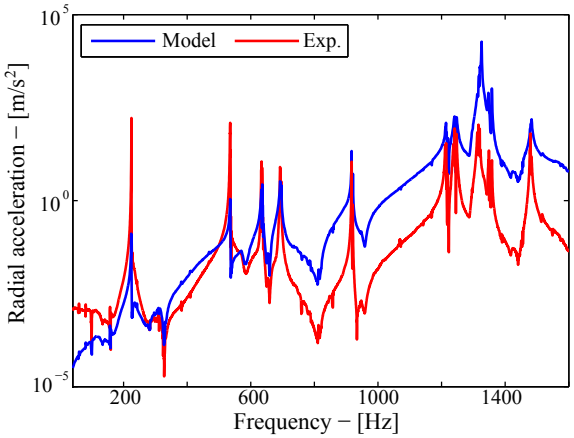

Figure 4.18. Comparison between the modal MD2-decomposed experimental data scaled with $\sqrt{P_{modal}}$ and the model for the thin shell at $m = 1$ with a model scaling of $\sqrt{P_{modal}}\frac{R}{\pi}$.

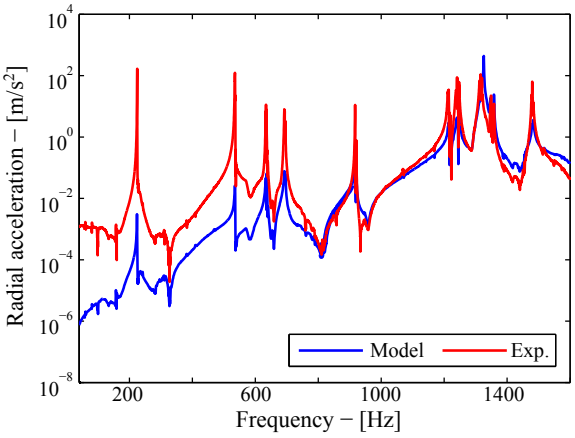

Figure 4.19. Comparison between the modal MD2-decomposed experimental data scaled with $\sqrt{P_{modal}}$ and the model for the thin shell at $m = 1$ with a model scaling of $\sqrt{P_{modal}}\frac{h}{\pi}$.

Notice in the figures that by this modal scaling the decomposition of the experimental data is obviously not improved and modal leakage is therefore still present in the response. However, as the force spectrum applied in the vibro-acoustic model is decompose by the same "poor" decomposition this spectrum contains similar modal leakage which is then transferred and thus accounted when used as scaling in the vibro-acoustic model.

This scaling approach seems to be very promising compared to those presented in figure 4.17 but is nevertheless not treated in either the thesis by Brian, [Olsen, 2001], nor in any other papers accessed in this thesis. It is nonetheless slightly uncertain whether this approach is in fact considered in these references or not, but judging from the comparison in [Olsen, 2001] it seems that a decomposed force spectrum has not been facilitated. This approach holds great potential and can possibly solve the issues related to poor modal decomposition. This is also discussed in the upcoming section.

Furthermore it is also seen from the figures the distribution of the two results are more or less identical and resemblance between the model and experiments are therefore considered excellent even though there might still be some unresolved scaling issues.

4.5 Reflections on comparison

Throughout this section the focus is on discussing the coherence between the model and the experimental data. This includes a discussion on why different scalings can be justified, the pitfalls observed in the modal decomposition.

4.5.1 Scaling between model and experiments

To determine the scaling of between the model and experiments we can extract this from the chosen ansatz by stating that the radial force summed over all modes should equilibrate the applied force just as stated in equation (4.7).

$$\sum_{m=0}^{\infty} q_{3m} \cos(m\theta) = P_0 \delta(\theta - \theta_0) R \tag{4.7}$$

where q_{3m} is the modal force amplitude, P_0 the intensity of the applied load and $\delta(\theta - \theta_0)R$ the circumferential "area" over which the load is distributed.

Now, applying Galerkin's orthogonalisation as in section 3.3.2 and integrate along the circumference the modal amplitudes appear as

$$q_{3m} = \frac{P_0}{\varepsilon_m \pi} R \cos(\theta_0) \qquad \varepsilon_m = \begin{cases} 2 & m = 0 \\ 1 & m \neq 0 \end{cases} \tag{4.8}$$

Thus as the experimental data is normalised with the force spectrum and that we apply a unit force in terms of a delta-function in the vibro-acoustic model it can be argued that the scaling between the model and experiments is $\frac{R}{\pi}$ as scaling with the force spectrum and successively normalising with it, is trivial. This scaling is applied in figure 4.14 and 4.17 for both shells and are found to overestimate the response.

On the other hand if the data retrieved from the experiments is not normalised with the force spectrum the scaling should be applied as in figure 4.15 and 4.17 i.e. as $\frac{\sqrt{P_{inp}}R}{\pi}$ where the square root appears as the force spectrum is provided as the power spectrum, N^2. Notice here that confer to the latter equation the scaling spectrum, P_{inp}, is based on the raw spectrum i.e. not the modal spectrum.

The final scaling for the thick shell shown in figure 4.16 is given as: P_{inp}. This scale is found empirically and does not contribute with any physical content. Nonetheless the overall coherence is good with this scaling for the thick shell, but when applied to the thin shell the coherence in the individual modes are compromised. Thus this scaling only seems to apply for the raw data.

The scaling for the thin shell in figure 4.18 and 4.19 is based on applying modal decomposition to the force spectrum and apply it in the scaling. Confer to the previous comparison this approach has shown to be the scaling which provides the best results, and the reason is in fact rather straight forward. Nonetheless if we considered the actual scaling the procedure seems at first hand trivial when it is expressed as illustrated in equation (4.9).

$$\sqrt{P_{modal}} w^{exp} \approx \frac{R}{\pi} \sqrt{P_{modal}} w^{shell} \qquad \Rightarrow \qquad w^{exp} \approx \frac{R}{\pi} w^{shell} \tag{4.9}$$

This equation is at first identical to the approach presented initially, however, if we compare the experiments and the model before the reduction we can obviate most of the errors present

in the modal decomposition. Thus in this approach we wish to compare the actual modal response measured by the accelerometers in the experiments i.e. not the normalised responses. Hence the modal experimental data is multiplied by the decomposed force spectrum to get the actual amplitudes. Likewise, the vibro-acoustic model is multiplied by the decomposed force spectrum to get the associated response calculated from the model when the same force input is applied.

Now, as the force spectrum and experimental data is decomposed by the same "poor" method we account for this when the same force spectrum is applied in the model as it contains flaws similar to those in the decomposed experimental data. Notice that this method is based on a sound physical principle and that this method allows us to visualise the actual coherence between the model and experiments and not the distorted pictures of figure 4.14 and 4.17 which they effectively are. It can therefore be concluded that this simple, but neat trick, is very important for the conclusions in a comparison between model and experiments when decomposition is necessary for the comparison. Thus this method can be viewed as a solution to the pitfalls in the modal decomposition discussed in the upcoming section. However, in this method we therefore need equally many measurement points and excitations points around a circumference to be able to conduct the decomposition of the force spectrum as well.

Finally, in figure 4.20 four different scalings are compared. The magna and cyan scaling is based on the exact same approach as just described, however the cyan is scaled by h instead of R. The green and red is scaled further by a $\sqrt{P_{modal}}$ such that it corresponds to the scaling in figure 4.15 where it is assumed that experimental data is not normalised by the force spectrum.

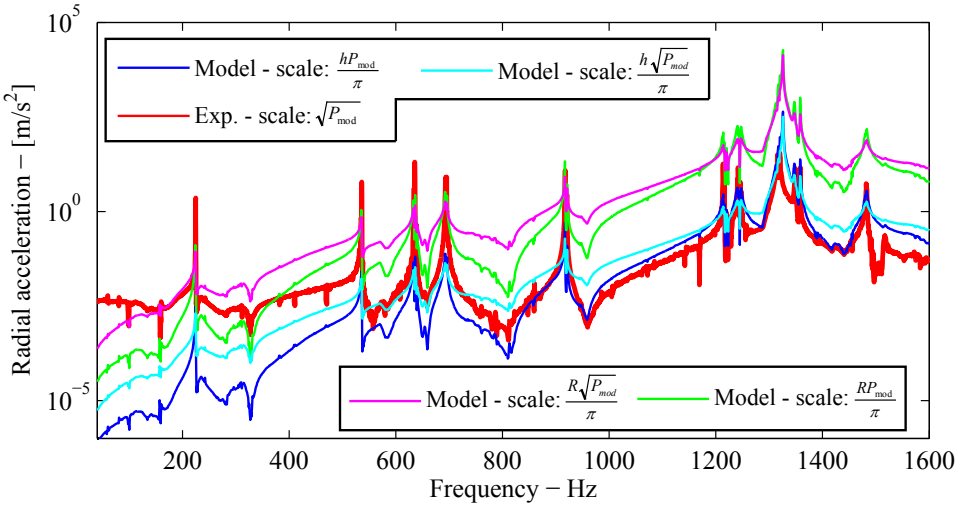

Figure 4.20. Comparison between four different scalings; all based on the proposed method by multiplying by the modal force spectrum and the experimental data at $m = 1$. The experimental data is decomposed by method MD3.

From this comparison it generally seems that the coherence is best when scaled by h rather than R and further that imposing the $\sqrt{P_{modal}}$ scaling improves the coherence. This may imply that the experimental data is not normalised. However, despite the good results obtained from this method it is nonetheless expected that it still contains some unresolved issues. For example it is seen from the latter comparison in figure 4.20 that by scaling with h rather than R the results are improved in the high frequency range but is nonetheless compromised in the low frequency range and vice versa. This scaling issue is expected to be related to either lack of experimental caution or the loss of phase information as the force spectrum is provided as

power, N^2. Furthermore it could also be caused by scaling the data and model linearly with the decomposed force spectrum when the decompositions are conducted separately.

Due to time constraint it has unfortunately not been possible to investigate this further in this thesis, but with the final issues solved this method is indeed considered essential in the comparison between model and experiments as it accounts for modal leakage in the decomposition of the experimental data.

4.5.2 Discussion of modal decomposition

Through this section we discuss some of the issues and inconsistencies observed during the modal decomposition of experiments and CFD-data. This discussion has come to be rather extensive as the issues cannot be explained with simple considerations. During this thorough study several very interesting things have been found which to the authors knowledge has not been addressed before. The study is initiated by considering general continuous functions represented by means of the Fourier method and their corresponding decompositions

Modal decomposition of continuous functions represented by the Fourier method

In this section we, initially, study the three general distributions of the Fourier method. Thus we study continuous functions represented as; either a periodic summation of sines, a periodic summation of cosines or as a combination of the two i.e. a periodic summation of complex exponentials. These three general cases are of significant interest in the vibrational shell theory as these functions are applied extensively in the ansatz' used for solving the system of linear differential equations that governs the complete nature of the shell vibrations and effectively the vibro-acoustic model. Consequently, the vibro-acoustic model implicitly assumes specific distributions of e.g. the shell displacements, force, pressure, velocity etc. This lead to a well-defined decomposition of both CFD and experimental data to adjust the data to the assumptions pre-implemented in the shell model. However, if the given data set (CFD or experimental) does not meet the requirements defined by the chosen ansatz would this introduce errors in decomposition and if so would it be significant errors.

For this specific study we consider a velocity source distributed by the three cases shown in equation (4.10) which in general represents all possible ansatz functions.

$$\begin{aligned} &\textbf{Case 1:} && \vartheta^{\cos} = \sum_{n=0}^{\infty} \vartheta_n \cos(n\theta) \\ &\textbf{Case 2:} && \vartheta^{\sin} = \sum_{n=0}^{\infty} \vartheta_n \sin(n\theta) \\ &\textbf{Case 3:} && \vartheta^{\exp} = \sum_{n=0}^{\infty} \vartheta_n \exp(in\theta) \end{aligned} \tag{4.10}$$

To decompose these sources properly by Galerkin's orthogonalisation method the orthogonalisation needs to be chosen with a similar distribution e.g. Case 1 i decomposed by a cosine, Case 2 by a sine and Case 3 by the conjugated complex exponential. However, when considering experimental data, CFD-data or any other empirical data the distribution of the data set is unknown.

The purpose of this study is then to investigate the errors we introduce if our initial assumption (from the ansatz) is wrong. Thus every Case in (4.10) is attempted decomposed by the three

available orthogonalisations corresponding to employing fault assumptions. The results from the different decompositions are presented in table 4.4 and the derivation for the different cases by each of the three orthogonalisations can be seen in appendix 4.5.2. In the table the diagonal corresponds to the proper choice of orthogonalisation parameters and thus these provide the actual amplitudes, ϑ_m.

	Orthogonalisations		
	$\cos(m\theta)$	$\sin(m\theta)$	$\exp(-im\theta)$
Case 1	ϑ_m	0	$\frac{1}{2}\vartheta_m$
Case 2	0	ϑ_m	$\frac{i}{2}\vartheta_m$
Case 3	ϑ_m	$-i\vartheta_m$	ϑ_m

Table 4.4. Results obtained when applying three different orthogonalisations to the three cases presented in equation (4.10).

From the table it is seen that if we assume that the data is distributed by a complex exponential function but the data is in fact distributed by a sine or a cosine the amplitudes retrieved from the decomposition will be only a half of the authentic amplitudes. Moreover the sine decomposition will also be in anti phase with the authentic amplitudes. On the other hand the decomposition of e.g. Case 1 by a sine function is useless and provides zero amplitudes. However, from the view point of post-processing and application of experimental data this is not as critical as this is immediately spotted by the user and the decomposition is changed.

From the latter cases a fourth case is constructed as a non uniform combination of trigonometric functions as seen in equation (4.11) which is in fact the most common case. Based on this case it is easily seen that cosine and sine decomposition alone is insufficient but combining the two according to (3.11) will provide the complete decomposition.

$$\textbf{Case 4:} \qquad \vartheta^{\text{Comb}} = \sum_{n=0}^{\infty} [\vartheta_n^c \cos(n\theta) + \vartheta_n^s \cos(n\theta)] \tag{4.11}$$

Again it can be verified from Galerkin's orthogonalisation that decomposing this by the complex exponential will directly provide the correct amplitudes and phase information needed. Thus the conclusion related to the decomposition is clear: It is of crucial importance to analyse the data thoroughly e.g. by different decomposition methods to determine the distribution of the actual data as this may cause either a factor 2 error in the amplitudes or an error in the phase information. As mentioned earlier this decomposition is equivalent to the amplitudes of the FFT, however in this case it is not possible to determine if the data is pure sine/cosine or exponential i.e. it is not possible to conclude on the factor 2 issue.

Another interesting thing in the FFT approach is that in most commercial software the $\exp(-im\theta)$-definition is adopted in the transformation thus if the data distributes as in complex conjugated of Case 3 the decomposition will tend towards zero (or small values) whereas the IFFT (Inverse FFT) will provide the correct decomposition. Hence if the FFT approach is taken it is important to verify both FFT and IFFT to verify the phase of the data and retrieve the correct amplitudes.

In fact the latter statements can easily be verified in a brief study where artificial response based on Case 1, Case 2, Case 3 and the complex conjugated of Case 3 are created and successively attempted decomposed by the FFT. Here it is noticed that the FFT data for Case 1 and Case 2 would be wrong by the factor of 2. For Case 3 we would extract the correct amplitudes and

the complex conjugated of Case 3 would provide zeros amplitudes (or due to numerical issues small amplitudes which for vibrations can be confused with actual amplitudes).

Thus in conclusion, as we do not know the distribution of our data beforehand, this needs to be studied very carefully before the Galerkin orthogonalisation is chosen or before attempting the quick and dirty assessment - the incautious FFT. Typically, (for both the CFD and experimental data) it has been relatively easy to conclude that both sine and cosine parts are present and effectively the decomposition is conducted with the exponential function. Nonetheless there might be cases where incautious attempts of decomposition will produce errors by a factor of two.

Finally, it can also be concluded based on the previous equations that the decomposition proposed by Brian in [Olsen, 2001] impair the phase information in the amplitudes as the modal amplitudes are here defined as the square-root of the cosine and sine contributions instead of the obvious relation derived by Euler's identity, shown in equation (3.11).

Modal decomposition for discrete data sets

With interest in the latter continuous decomposition we extent the equations to discrete data by representing the integral through a summation. In the discrete formulations the aforementioned orthogonalisations issues are obviously still present and in addition the discrete formulations does also introduce aliasing which can nevertheless be avoided by application of Nyquist's sampling theorem, in which it is stated that the sampling frequency need to be twice the desired spectrum to avoid aliasing. Translated to modal decomposition we need 10 measurement point to retrieve 5 modes, $m = 0, \ldots, 4$.

Through the study conducted in the following it has actually been possible to circumvent Nyquist's sampling theorem in some way to extract more modes from a confined number of measurement points. Furthermore it is observed that when truncating to a finite number of sampling points the infinite number of modes are divided in a specific order into the modal amplitudes we wish to decompose where this ordered summation have been located through this study. Effectively, the decomposed modes would always be affected by aliasing.

If we now consider the cosine and the exponential decomposition in the discrete domain the following decompositions appear.

$$\vartheta_m^c = \frac{2}{\varepsilon_m^c N} \sum_{n=0}^{N-1} \vartheta_n \cos\left(\frac{2\pi n}{N} m\right)$$

$$\vartheta_m^e = \frac{1}{N} \sum_{n=0}^{N-1} \vartheta_n \exp\left(-i\frac{2\pi n}{N} m\right) \tag{4.12}$$

where ^{e} and ^{c} indicates the orthogonalisations applied in the decomposition and N is the number of circumferential measurement points.

To, once again, verify the decomposition by these two method when the actual experimental data distributes with the exponential function including all infinite modes i.e. $m = 0, \ldots, \infty$ the summation of Case 3 is substituted into the latter equations and the decompositions expands

to equation (4.13).

$$\vartheta_m^c = \frac{2}{\varepsilon_m^c N} \sum_{n=0}^{N-1} \sum_{k=0}^{\infty} \bar{\vartheta}_k \exp\left(i\frac{2\pi n}{N}k\right) \cos\left(\frac{2\pi n}{N}m\right)$$
$$\vartheta_m^e = \frac{1}{N} \sum_{n=0}^{N-1} \sum_{k=0}^{\infty} \bar{\vartheta}_k \exp\left(i\frac{2\pi n}{N}k\right) \exp\left(-i\frac{2\pi n}{N}m\right) \tag{4.13}$$

For the continuous functions this would be trivial as the orthogonality properties of the trigonometric function would reduce the equations to $\vartheta_m^c = \bar{\vartheta}_m$ and similar for the exponential decomposition. However, as the discrete formulas are further confined by their discrete symmetry properties even though discrete orthogonality also applies these summations can then be conveniently reduced by applying the discrete orthogonality and symmetry properties of the trigonometric functions. Thus we arrive at

$$\vartheta_m^c = \varepsilon_m^c \bar{\vartheta}_m + \sum_{k=1}^{\infty} \left[\bar{\vartheta}_{(kN-m)} + \bar{\vartheta}_{(kN+m)}\right] \tag{4.14}$$

$$\vartheta_m^e = \sum_{k=0}^{\infty} \bar{\vartheta}_{(kN+m)} \tag{4.15}$$

which for the continuous function was trivial as discussed.

The latter equations, has to the authors knowledge, never be addressed before and by investigation of these they are actually essential to the understanding of decomposition of, in fact, any discrete data set. The interpretation of the latter equations does in fact enlighten us, as it was stated initially, that when we introduce a finite number of measurement points to represent the integral of a periodic summation of trigonometric functions by means of a summation aliasing occurs but not necessarily according to Nyquist's sampling theorem. Thus the latter equation, whether cosine or exponential, does in fact explicitly state that aliasing will always occur if the actual spectrum is expressed as an infinite periodic sum of trigonometric functions. Furthermore the convenient formulation allow us to not only conclude that aliasing is always present but also to determine each individual aliasing term present in the decomposed amplitudes but not to explicitly derive them. This immediately raises the essential question:

Is it possible to decompose the summation of equation (4.15) *even further to derive each individual mode?*

This question is however not easily answered and in this thesis the time would not allow for further investigation into this area. If it is however possible to derive these individual modes from the summation above its significance to general decomposition of sampled data would be extrodanary.

Through this thesis the time does however "only" allow for the following practically important question:

How many sampling points should be included to avoid significant spurious modes to be included in the modes of interest?

The answer to this question is on the other hand straightforward and can be answered simply by investigating the significance of the modal response through the model and when the modal response is found insignificant in relation to the previous modal response in the summation of equation (4.15) then the number of sampling points can be determined. This statement is easier explained through an example. Consider therefore the cosine summation of equation (4.15) written out in (4.16) for $N = 10$ sampling points, in our case, around the circumference.

$$\begin{aligned}
\vartheta_0^c &= 2\bar{\vartheta}_0 + 2\bar{\vartheta}_{10} + 2\bar{\vartheta}_{20} + \dots \\
\vartheta_1^c &= \bar{\vartheta}_1 + \bar{\vartheta}_9 + \bar{\vartheta}_{11} + \bar{\vartheta}_{19} + \bar{\vartheta}_{21} + \dots \\
\vartheta_2^c &= \bar{\vartheta}_2 + \bar{\vartheta}_8 + \bar{\vartheta}_{12} + \bar{\vartheta}_{18} + \bar{\vartheta}_{22} + \dots \\
\vartheta_3^c &= \bar{\vartheta}_3 + \bar{\vartheta}_7 + \bar{\vartheta}_{13} + \bar{\vartheta}_{17} + \bar{\vartheta}_{23} + \dots \\
\vartheta_4^c &= \bar{\vartheta}_4 + \bar{\vartheta}_6 + \bar{\vartheta}_{14} + \bar{\vartheta}_{16} + \bar{\vartheta}_{24} + \dots \\
\vartheta_5^c &= 2\bar{\vartheta}_5 + 2\bar{\vartheta}_{15} + 2\bar{\vartheta}_{25} + \dots \\
&\wr \\
\vartheta_6^c &= \bar{\vartheta}_6 + \bar{\vartheta}_4 + \bar{\vartheta}_{16} + \bar{\vartheta}_{14} + \bar{\vartheta}_{26} + \bar{\vartheta}_{24} + \dots
\end{aligned} \tag{4.16}$$

From this expanded summation it is first of all evident that for 10 samplings point we can only recover 6 modes, $m = 0, \dots, 5$ as the sixth mode, $m = 6$ is identical to the fourth mode, $m = 4$, and the seventh equal to the third etc. This is on the other hand also well-know from FFT analysis where the amplitudes are symmetric. Thus in relation to aliasing in decomposed amplitudes aliasing occurs, not according to Nyquist's sampling theorem, but as $\frac{N}{2} + 1$ i.e. we get an additional mode for free. Further it is interesting to notice that if the data that is decomposed only includes 6 significant modes (starting from $m = 0$) the decomposition by 10 samplings point provide the exact amplitudes whereas if the data contains 8 significant modes only the first 3 modes are decomposed exact and for an even number of sampling points so is the fifth mode $m = 5$. Thus in summary; for increasing significant modes included in the data the decomposed amplitudes deviate from the correct starting at $m = \frac{N}{2} - 1$ with $m = \frac{N}{2}$ being the last for even N. For odd N they deviate from the highest mode towards the lowest.

This summation does also apply for an odd number of sampling points. In this case the number of extracted modes without occurrence of decomposed aliasing is half the sampling points and rounded up. Thus for $N = 9$ the number of extracted modes is 5.

If we on the other hand consider the exponential summation from equation (4.15) a very interesting point is found.

$$\begin{aligned}
\vartheta_0^e &= \bar{\vartheta}_0 + \bar{\vartheta}_{10} + \bar{\vartheta}_{20} + \dots \\
\vartheta_1^e &= \bar{\vartheta}_1 + \bar{\vartheta}_{11} + \bar{\vartheta}_{21} + \dots \\
\vartheta_2^e &= \bar{\vartheta}_2 + \bar{\vartheta}_{12} + \bar{\vartheta}_{22} + \dots \\
&\vdots \\
\vartheta_9^e &= \bar{\vartheta}_9 + \bar{\vartheta}_{19} + \bar{\vartheta}_{29} + \dots
\end{aligned} \tag{4.17}$$

(4.18)

From this equation it is immediately seen that for 10 sampling points we are able to recover 10 modes without introducing aliasing. This is a very interesting observation as it enlighten us that if the data distribute with an exponential function we can recover as many modes as we have sampling points around the circumference. Further it is also seen that we are able to

capture the 10 modes exact if there are only 10 significant modes present in the data. Thus in this case we get $\tilde{m} = N$ and we completely circumvent the sampling theorem stated by Nyquist. As a final remark it is worth noticing that for an increasing number of significant waves in the data the amplitudes are, in this cases, compromised from $m = 0$ towards $m = N$. Thus in conclusion the imprint by an Euler distribution is more unique and we can therefore decompose more modes.

Through this study an interest discovery has been made and in fact it has lead to the important conclusion that the number of measurement points around the circumference are not determined by the desired number of modes to be analysed and Nyquist's sampling theorem but in fact it is governed by the number of modes which are significant in the overall response. As a guidance it is recommended to include all modes which has a cut-on within the frequency spectrum of interest.

The future task in improving the modal decomposition method for test results is how to collect the modal response for the higher order modes such that this contribution is separable from the lower order modes. This is indeed an interesting area from a research point of view as the modal decomposition is a widely used method and usually the pitfalls in the decomposition are blamed on the sources of error related to the experiments. Nevertheless the latter discussion may suggest otherwise and the pitfalls might instead be governed by the decomposition assumption/truncation. The purpose of the following uncertainty study is exactly to investigate the actual cause of the pitfalls.

4.5.3 Uncertainty study in modal decomposition

The following uncertainty study is based on a toy case where an artificial radial response is constructed in accordance with the ansatz used in the governing equation i.e the response is constructed as shown in equation (4.19).

$$w(\theta) = \sum_{m=0}^{\widetilde{m}} W_m \cos(m\theta) \tag{4.19}$$

where the modal amplitudes, W_m are generated randomly as complex numbers within a range of $\pm 5\%$ of the radii.

In the study two random deformation shapes are investigated. These are shown in figure 4.21 for Case 1 and in figure 4.22 for Case 2 illustrating both the deformed and original shape.

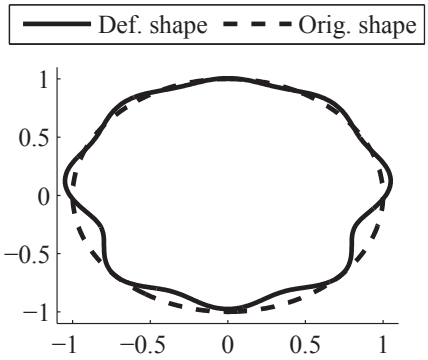

Figure 4.21. Case 1: Deformed shape created according to equation (4.19) with $\widetilde{m} = 9$ and the modal amplitudes generated randomly within a range of $\pm 5\%$ of the radii.

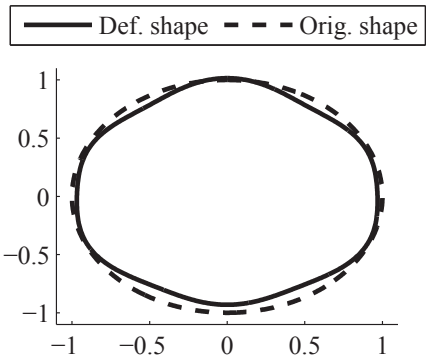

Figure 4.22. Case 2: Deformed shape created according to equation (4.19) with $\widetilde{m} = 9$ and the modal amplitudes generated randomly within a range of $\pm 5\%$ of the radii.

The study of different modal decomposition methods are thus based on the attempt of recovering the exact same modal amplitudes that was used in the construction of the artificial response. This attempt is met by sampling at $N = 10$ evenly distributed points around the circumference as this is equivalent to the experimental procedure. What is trivial here is that under certain conditions the artificial response can be fully recovered by either of the modal decomposition methods described above namely when $N \geq 2\widetilde{m}$.

The direct purpose of this uncertain study is thus to investigate how the amplitudes are recovered if $N < 2\widetilde{m}$ or if the sampling points are slightly misplaced i.e. if the accelerometers are not evenly distributed. The uncertainty study with respect to these two parameters are conducted first by gradually increasing the number of significant modes in the response from 5 to 10 modes with the number of sampling points fixed at $N = 10$. In this case the included modal responses are all within the same order of magnitude (it is generated randomly within the ±5%) i.e. the modal contribution does not drop gradually in this study.

Secondly, 5 modes are included and each measurement point is perturbed individually again through a random generation. Here the two cases are investigated when the maximum perturbations are allowed a variance of ±1%, ±5% and ±10%. This corresponds to a misplacement of ±4.34mm, ±21.70mm and ±43.39mm for the thin shell and it is expected that the variance in the conducted experiments are within the ±1%. Finally a study including both cases are conducted.

Chosen results, in terms of the relative error to the actual amplitudes, are shown for Case 2 in table 4.5 and the complete set of results for both cases are found in appendix A.7.

Case 2	m=0 Rel. Err. [%]	m=1 Rel. Err. [%]	m=2 Rel. Err. [%]	m=3 Rel. Err. [%]	m=4 Rel. Err. [%]
7 modes	0	0	0	0	215.76
8 modes	0	0	0	91.62	215.76
9 modes	0	0	60.85	91.62	215.76
10 modes	0	34.89	60.85	91.62	215.76
±1%	1.20	10.12	2.73	4.84	5.87
±5%	1.65	10.77	23.05	10.14	20.84
±10%	18.31	45.02	7.49	34.54	76.33

Table 4.5. Results from uncertainty study for Case 2. Elaborated results for Case 2 and results for Case 1 can be found in appendix A.7.

Based on the results from the table it is easily observed that the number of governing modes are definitely the most influential part for the quality of the modal decomposition. The results presented here are in most cases exaggerated as the modal response tends to gradually decrease in amplitude for higher modes. Nonetheless it is still important to verify the cut-on frequencies in the spectrum as resonances will have large amplitudes and therefore cause extensive modal leakage, especially for modes close to $N/2 - 1$ (can be verified by extension of the summation in (4.14)).

For the misplacement study alone the maximum error for the ±1% deviation (remember it is generated randomly and is therefore not a worst case study) is 10% at $m = 1$ for Case 2 as seen in the table. This result is of course relative as it depends on the misplacement generation

and similar on the deformation shape. In effect this might cause for a more comprehensive uncertainty study which is however omitted here.
To compensate for the misplacements the decomposition can be done by means of a DTFT as this represents the frequency-continuous periodic summation from which the Fourier coefficients are sampled. However, while this is a way to overcome the issues related to misplacements it may be difficult to quantify the misplacements as it is assumed that the accelerometers where placed by best effort in the beginning and misplacements are therefore not necessarily obvious.

In the misplacement study it has also been observed that when introducing perturbation the sine contribution in the methods are non-zero even though the response is introduced as in equation (4.19). The presence of a sine term is exactly what causes the deviations and if the experimental results are considered it is seen that the sine part is non-zero however with a magnitude 2-3 times lower than the cosine part. This is in good agreement with what was observed in the uncertainty study for $\pm 1\%$.

Thus it is concluded that the non-zero sine terms of the experimental decomposed data are primarily governed by misplacement of the accelerometers or excitation points. This leads further to the conclusion that the $\cos(m\theta)$ distribution of the radial component is in agreement with what was observed in the experimental results.

Inverse source characterisation 5

As stated initially in the thesis it is intended to apply the recent developments, improvements and aspect of novelties found through this thesis to apply inverse methods to recover the source characteristic by correcting the vibro-acoustic model according to the measurements retreived through experiments.

For the experiments conducted in this thesis inverse source characterisation is actually rather trivial as the shape, location and intensity is well-defined in these experiments as the pipe is excited by a modal hammer (a point source) which measure the input source and normalise the spectrum with the force spectrum (intensity is unity) and the source is applied at the same location in which we measure (the location is known). Thus there are in fact no unknown parameters to be fitted.

On the other hand in measurements on fluid-filled shells loaded in the acoustic field the aforementioned parameters are difficult to accurately predict which effectively introduce significant uncertainties in the comparison between model and experiments. Typically, an acoustic source is introduced through a hydrophone in reverse mode and even though this source is somewhat well-defined it is nonetheless still with some uncertainties that may affect the coherence between model and experiments.

Through this chapter we are devoted to apply inverse source characterisation to the rather trivial case of a shell model for a finite hollow pipe. This attempt then serves as a prove of concept to investigate if the measured imprint are sufficiently unique to characterise the source when loaded with a given source, location and intensity. Furthermore the following investigation is solely related to study and discuss the sensitivity parameters affecting the optimisation, how they can be improved to decrease the significance of the initial guess and suggestions to improvements for tailored experimental work to enhance the source characterisation method. Thus the scope of this thesis is at this stage not to study the effects of different optimisation algorithms but rather to apply optimisation to draw conclusions on whether or not source characterisation can be achieved by inverse methods. This chapter is therefore confined to only applying the standard optimisation algorithms in Matlab.

5.1 Formulation of the optimisation

In general inverse modelling are based on either inversion of the problem or on inverse optimisation. In this thesis only the optimisation approach is treated and the formulation applied here is based on a least square objective function.

The design variables, x, with the source characterisation scope in mind, is generally confined

to: location, shape and intensity of the source. In general these design variables can enclose individual design variables e.g. in the definition of the shape. For the optimisation algorithm used in the inverse source characterisation the objective function is as mentioned formulated as a least square between the experimental data and the model as indicated in equation (5.1). Furthermore in this formulation the design variables are unconstrained.

$$f^{obj} = \min_{x} \Psi(x)\Psi^{T}(x) \tag{5.1}$$

where x includes the design variables and Ψ is the residual defined as

$$\Psi = \psi^{exp} - \psi^{model} \tag{5.2}$$

where ψ^{exp} is a vector including the selected experimental data and ψ^{model} a vector including data "measured" in the model at points identical to those from the experiments.

Now, the final step before the optimisation is to determine what should be included in ψ to get the best solution. Thus the issue here is how to chose proper segments of the data to get a fast optimisation and a confined number of local minimums inside the optimisation domain such that the sensitivity to initial guesses are decreased. Furthermore the number of design variables should also be defined as this in general varies dependent on the complexity of the specimen (with or without fluid) and on what is unknown or severely affected by uncertainties in the experiments. These issues are discussed in the following discussion.

5.1.1 Discussion on representative data for the residual

The following discussion is divided into the following three branches; *Proper choice of representative data, Number of measurement points, Proper choice of design variables.*

Proper choice of representative data

To chose the proper data and create a residual that is representative for the shell the attention is lead towards the distribution of the experimental data. As can be seen from these figures e.g. 4.2 the measured response is accelerations decomposed into amplitudes at given frequencies and as is seen the response is varying significantly in magnitude. Consequently comparing the full data set at every frequency with the model would be both computational expensive and in fact trivial as the residual in-between the resonances would be insignificant in the least square measure. Thus the data in the residual might as well be reduced to only include the resonances as almost any other data would be insignificant in the least square measure. This does however immediately introduce an issue in the model as it is singular at the resonances. To comprehend this we introduce damping to the system by means of an imaginary part to Young's modulus such that

$$E \sim E + i\tilde{E} \tag{5.3}$$

In this case $\tilde{E}$ is unknown and can either be used as a design variable in the optimisation or estimated in comparison with the experimental data. The damping part to Young's modulus is usually taken as 10^{-4} or in the same order of magnitude.

Number of measurement points

Similarly the results will also be affected by the number of measurement points included in the least square. The effect of the number of measurement points need to be investigated during

the optimisation study as the effect is not known beforehand. Thus by starting with a single measurement point and increasing to 2, 3 or 10 it should be possible to conclude on whether the initial guess sensitivity decreases or increases. Notice likewise that from a practical point of view it is favorable to use as few measurement points as possible.

Proper choice of design variables

As mentioned the design variables are in general; the location, the shape and the intensity of the source. However, it is also possible to incorporate the damping part of Young's modulus and other possible material parameters. Similarly the shape of the source may not necessarily be sought as a delta-function or a summation of trigonometric functions but may be sought as discrete data along the pipe which is then subsequently interpolated into a continuous function. Thus the possible design variables can actually incorporate more than the three variables stated initially and the choice of design variables is therefore related to the assumption regarding the source distribution and likewise to what can be considered as unknown or uncertain parameters in the experiments.

5.2 Results from optimisation

With interest in the previous discussion it has been attempted to achieve optimisation results for a cases were the number of local minimums is expected to be low. This study was based on the thick pipe as no decomposition is necessary for this here according to section 4.2.1. Furthermore the results where sought on a straight line along the pipe and the shape of the source is therefore pre-specificed to a delta-function with a corresponding intensity. However due to the issues found in relation to scaling and modal decomposition the results found here was useless and too sensitive to the initial guess. Thus, unfortunately, no valid results are available in this section as it was decided to put the effort in solving the issues found in scaling and modal decomposition first.

This is chosen as it can be concluded that these issues are essential to the quality of the inverse source characterisation method and these issues does therefore need to be solve before attempting further inverse methods. However, proposals on how to circumvent the unresolved issues to prove the concept of inverse source characterisation is discussed in the following section.

5.3 Interpretation of results

As mentioned the comparison between the model and experiments are compromised by the scaling issues discussed in section 4.5.1 and consequently the inverse modelling is put on hold for now.

However, with interest in the studies done in the attempt of solving the modal decomposition issues as well as the scaling issues it has been found that we can circumvent these issues and prove the concept through a purely mathematical study. Furthermore this allows for studies on possible uncertainties from which we can tailor the experiments to inverse source characterisation and thereby decrease sources of error that may dispute the results obtain from inverse source characterisation.

This study is based on applying a source (random or a simple delta-function) in the vibro-acoustic model and "measure" the response at chosen locations on the infinite fluid-filled shell (structured or random). The "measured" response and their associated locations are then saved and is subsequently imported into the optimisation workspace where it is treated as experimental data measured in the associated points. The idea is now simply to study if and how accurate we can recover the original source, the location and the intensity by the "measurements" available. To add complexity and possible issues gradually as well as enhance the understanding of the sensitive parameters the procedure is proposed to apply different source in the following chronological order:

1. A delta-source at a specific frequency and circumferential wave-number
2. An arbitrary acoustic source at a specific frequency and circumferential wave-number
3. A delta-source "divided" into 5, 10 or more modes
4. An arbitrary acoustic source "divided" into 5, 10 or more modes
5. Decomposed CFD-data

Following this procedure it is supposed that possible issues will be added gradually and can then be solved accordingly such that it can be accounted for when tailoring the experiments. Furthermore the latter procedure should be straightforward for the first two sources but as modal decomposition is incorporated in the following there might originate some issues to be solved here. However as this is all based on a case study we can investigate this in detail with no addiational costs and when these issues are solved for the case study it can be generalised to the experimental data and the modal decomposition and/or scaling issues may therefore also be solved.

The final case with CFD-data does in fact represent the final scope of the inverse source characterisation as the CFD-data is considered as the actual source and in principle (in the study) we do not care for its physical representation of the pump. Effectively, this is the ultimate test of the inverse source characterisation and if it is possible to recover the CFD-data by this method this tool is becomes indispensable to Grundfos as it allows for a much better representation of their pump characteristic than what can be achieved by CFD simulations.

Furthermore from the knowledge gained through the uncertainty and modal decomposition study we know exactly how to create response without aliasing and how to incorporate aliasing such that we introduce issues similar to those present in actual experimental data. Thus we can create response resembling the actual data quite well and thus introduce the issues found in the experiments but avoid the noise from the experiments. Then when the case study is investigated in depth the method can be validated through experiments.

In conclusion it is proposed that the inverse source characterisation is handled in detail through the proposed case study until "all" issues are solved and we are able to recover the CFD data by means of this inverse method. Nonetheless the author is optimistic that given the right time frame it is possible to solve the inverse source characterisation problem and provide the an indispensable tool for Grundfos. With this statement we conclude this chapter of inverse source characterisation and move to the final conclusion of the thesis.

Conclusion 6

Throughout this thesis several issues to novelty as well as practical issues have been addressed within the area of vibration in elastic cylindrical fluid-filled shells considered a multi-modal waveguides. As it was discussed in the introduction the general scope is divided into three main areas and two additional areas. In the overall scope of Grundfos it is indented to damp the pulsations and effectively the vibrations and sound radiated from piping systems. This has lead to the derivation of a vibro-acoustic model that accounts for the fluid-structure interaction phenomenons.

This model is fully developed and discussed in the associated conference paper, [Ledet et al., 2015], where it was found that by facilitating the recent bi-orthogonality properties (derived on 9. semester for the first time for a fluid-filled shell) in solving the system of linear equations it is possible to derive a solid explicit and analytical algebraic equation which allows for direct evaluation of the modal amplitudes.

Furthermore the paper is extended to prove the validity of the recent developments within fluid-filled vibrational shell theory. The model is first validated through a benchmarking to the existing results in [Sorokin et al., 2004] where it was found that the enhanced model of this thesis provides identical results for the mechanical loadings presented in the reference model. However, to ensure the models validity when loaded in the acoustic medium it is validated through a convergence study.

In the convergence study it was found that the convergence of this proposed method is related to the symmetry conditions and effectively this has lead to another and indeed very important property of the proposed method over the conventional method namely that a distinct convergence study is not necessary as all the convergence parameters are readily available and visible in our final graphs of interest. This convenient property originates as the value of convergence in the proposed method is known i.e. symmetry conditions needs to be zero whereas in the conventional approach the convergence is addressed by evaluating the convergence of the amplitudes as more waves are included.

Unfortunately, no converged models exist for acoustically loaded fluid-filled shells when applying the conventional approach for solving the equation system as only 8-10 waves can be included in the analysis. For acoustical loadings it has nevertheless been shown in the paper that for the waveguide treated here 25 waves are needed to achieve convergence. In conclusion the proposed method is much stronger than the conventional approach both from the view point of computational efficiency and from the view point of accuracy as each modal contribution is known explicitly but certainly also from the view point of convenience as we are always enlightened about the convergence.

The initial part of the present thesis treats further improvements necessary to cope the overall

scopes of this thesis. Therefore this chapter can be viewed as a theoretical chapter including independent sections of improvements. Initially, improvements for calculating the dispersion curves are treated with the scope of improving the models possibility for inverse source characterisation and optimisation in general. Through this investigation an approximation based on a linear combination of the zeros of the Bessel-function to approximate the real roots of the dispersion equation is proposed. This method was found to be in good agreement with the authentic roots and the approximation even captures the "phase" transition in the root. For the remaining roots it is proposed to calculate these based on the initial parameters and in iterations with changing physical parameters correct the roots by a simple and efficient Newton-Raphson scheme.

Subsequently, the power flow equation for the fluid term i reformulated from an integral into its equivalent analytical expression and effectively this allow us for reduce the integral from M^2 independent integrals to $\frac{M^2+M}{2}$ simple function evaluations. Further the model as been extended to directly incorporate arbitrary forces to cope with the scope of analysing the vibro-acoustic performance of the piping system. To ensure a correct derivation of the equations for arbitrary sources this has been validated for an acoustic velocity source by means of applying a probability function source and compare the power flow to that for a delta-function while gradually penalizing the probability function towards the delta-function. Finally, this chapter introduce the Boundary Integral Equation Method for hollow shells to extend the vibro-acoustic model to a finite pipe such as to cope with the experimental set-up designed to reduce sources of error in the experiments.

With the improvements to the model derived we draw the attention to the CFD-data provided by Grundfos where we by means of modal decomposition deduce the acoustical sources present in this response. This decomposition is done with basis in Fourier transformations and terminated in continuous acoustical source distribution across the radii for each circumferential wave-number and frequency. Subsequently, the acoustical sources are applied in the model to assess the vibro-acoustic performance of the waveguide when subjected to the acoustic sources deduced from CFD modelling of an operating pump. In this study it has been found that even though no traveling waves are present at a given circumferential wave-number there is still an exchange of energy in the near field. This has come to be surprising as the general understanding of decaying and attenuating waves is that they convey no energy. Nonetheless the latter study indicates that the energy exchange is present and energy in individual transmission paths is therefore transported, however with the total energy conveyed being zero. In conclusion the power flow seems to be insensitive to the source distribution and is in fact governed by the intensity. Furthermore inconsistencies are found between the CFD model and the vibro-acoustic model when comparing the source distribution at the excitation point.

Through the experiments the scope was to validate the model and therefore the focus here is put on reducing the sources of error in the experiments to improve the results obtained from the experiments. Thus the experiments are conducted for two finite hollow pipes confined by free-free boundary conditions. Initially, the material parameters, in this case Young's modulus, for the test specimens are determined through and inverse method and subsequently the symmetry of the pipe is assessed from which it was found that due to the seam in the pipe the resonances originate in pairs of closely related resonances. Furthermore the coherence between the resonances are found very good and for the thick shell they are all within ± 0.25Hz and for the thin shell within 0.77%. Subsequently the decomposed experimental data is

compared to the model. Here there are found several issues related to the proper scaling between shell model and experiments however by accounting for modal leakage in the model the actual coherence between models reveals and excellent coherence is found for both the thin and thick pipe. Finally, the experimental chapter discuss the different scaling issues and the modal decomposition used for the experimental and CFD data. This latter investigation contains great potential and addresses several interesting topic which has not been explored before. It was here found that the number of necessary measurement points to achieve proper decomposition of the data is determined by the number of significant modes in the response and the distribution of the data that is to be decomposed. Thus the conventional understanding where the number of measurement points is chosen based on the maximum circumferential mode desired and Nyquist's sampling theorem is not valid. Finally, it can be concluded that care should be taken when applying decomposition and if the data is not investigated properly errors may and will occur in the decomposed data.

Finally, the possibilities in relation to inverse source characterisation is addressed and it is here found that due to the unresolved issues regarding scaling and modal decomposition the comparison between the model and the experiments is compromised. This obviously affect the results obtained in the inverse source characterisation and the results is therefore considered in-feasible . Nonetheless a method that comprehends these issues are proposed. The idea is simply to create and arbitrary source, apply it in the shell model and measure at chosen points on the shell. These "measured" point are then treated as experimental data in the inverse source characterisation. This allows for uncertainty and parameter studies which lead to important knowledge before this is attempted on experiments including fluid.

As a final conclusion on the thesis the three-folded initial scopes have been addressed successfully and a sustainable method has been developed to assess the vibro-acoustic performance of any waveguide and any acoustic source. Similar the two extended scope have been treated successfully, nonetheless with a lack of results with respect to inverse source characterisation. With regards to the author personal experience the academic level of the project has really been acknowledged and similar the possibility of coupling the academic studies with practical experiments are greatly acknowledged. In conclusion this thesis includes many aspects of novelty and in addition another month would have been favourable to sort out the issues that are left unresolved in the thesis due to time constraints. Likewise this would also have lead to an increased quality on the documentation of the section *Reflection on comparison* and the latter chapter on *Inverse source characterisation* as these would not have had to be written in a hurry.

Future work 7

As mentioned this thesis includes several aspects of novelty and these novelties has lead to great possibilities within the area of fluid-filled cylindrical shell vibration. As the model derived here is much stronger from a computational and accuracy point of view it has revealed quite a few novel aspect to be analysed. Some of these are listed below.

- Enhancing the complexity of the model for example by including mean flow and pressure
- Consider composed pipe segments. Steel-steel or steel-flexible hose
- Calculate transmitted and reflected waves in composed segments
- Calculate the radiated sound power in e.g. transitions between composed pipe segments, in the transition below cut-on as indicated in figure 3.13
- Introduce a boundary layer to account for the viscosity and the reduced sound speed in the boundary layer between the fluid and shell wall
- Introduce Lighthill's acoustic analogue to account for cavitation, turbulent flow and other non-linearities
- Model uncertainties e.g. in relation to experiments
- Sensitivity analysis/parameter study
- Improvements on the modal decomposition method e.g. by DTFT
- Fully developed inverse source characterisation method for the case study and generalise into a tool for correcting existing CFD models
- Use model as a design tool to design a revolutionary pulsation dampener fitted to the characteristic of the pump
- And more...

Bibliography

AK Steel, **2015**. AK Steel. *Data sheet for Stainless Steel - 316/316L - via Google.com.* www.aksteel.com/pdf/markets_products/stainless/austenitic/316_316l_data_sheet.pdf, 2015. [Online; accessed 12-May-2015].

Brüel & Kjær, **2015**. Brüel & Kjær. *Data sheet access.* www.bksv.com, 2015. [Online; accessed 27-April-2015].

Chapman and Sorokin, **2009**. C. J. Chapman and S. V. Sorokin. *The finite-product method in the theory of waves and stability.* Proceedings of the Royal Society A, 466, 471–491, 2009.

Feng, **1996**. L. Feng. *Experimental Studies of the Acoustic Properties of a Finite Elastic Pipe Filled with Water/Air.* Journal of Sound and Vibration, 189, 511–524, 1996.

Fuller and Fahy, **1982**. C. R. Fuller and F. J. Fahy. *Characteristics of wave propagation and energy distributions in cylindrical elastic shells filled with fluid.* J. Sound Vibration, 81, 501–518, 1982.

Grundfos Holding A/S, **2014-2015**. Sound and Vibration Centre Dept. 3930 - Grundfos Holding A/S. *Material provided by Grundfos*, 2014-2015. Contact persons: Jan B. Larsen and Martin M. Lauridsen.

Huffington Post, **2015**. Huffington Post. *Picture of pipeline.* www.huffingtonpost.ca/2013/10/01/pipelines-likely-to-stay-_n_4026400.html, 2015. [Online; accessed 26-May-2015].

Imagbuddy, **2015**. Imagbuddy. *Picture - via Google.com.* imgbuddy.com/computer-monitor-drawing.asp, 2015. [Online; accessed 28-April-2015].

Kreyszig, **2011**. Erwin Kreyszig. *Advanced Engineering Mathematics.* John Wiley & sons inc., 2011. ISBN 978-0-470-64613-7.

Landau, **1999**. L. J. Landau. *Ratios of Bessel Functions and Roots of* $\alpha J_\nu(x) + xJ'_\nu(x) = 0$. Journal of Mathematical Analysis and Applications - JMAA, 240, 174–204, 1999.

Ledet, Sorokin, Larsen, and Lauridsen, **2015**. L. S. Ledet, S. V. Sorokin, J. B. Larsen, and M. M. Lauridsen. *Bi-orthogonality Conditions for Power Flow Analysis in Fluid-Loaded Elastic Cylindrical Shells: Theory and Applications.* NOVEM - Conference paper, pages 5606–5617, 2015.

Novozhilov, **1959**. V. V. Novozhilov. *The theory of thin shells.* P. Noordhoff, Ltd. Groningen, 1959. English version translated by P. G. Lowe.

Brian Ottar Olsen. Vibroacoustic power flow in infinite compliant pipes excited by mechanical forces and internal acoustic sources. PhD thesis, University of Southampton, 2001.

Omaspec Global Ltd., **2015**. Omaspec Global Ltd. *Picture oil and gas industry.* www.omaspecglobal.com, 2015. [Online; accessed 26-May-2015].

Pavić, **1990**. G. Pavić. *Vibrational energy flow in elastic circular cylindrical shells.* J. Sound Vibration, 142, 293–310, 1990.

Rawlins, **2011**. Anthony D. Rawlins. *The method of Finite-Product Extraction and an application to Weiner-Hopf theory.* Journal of Applied Mathematics - IMA, pages 1–13, 2011.

Sorokin and Terentiev, **2006**. S. V. Sorokin and A. V. Terentiev. *Flow-induced vibrations of an elastic cylindrical shell conveying a compressible fluid.* Journal of Sound and Vibration, 296, 777–796, 2006.

Sorokin, Nielsen, and Olhoff, **2004**. S. V. Sorokin, J. B. Nielsen, and N. Olhoff. *Green's matrix and the boundary integral equation mothod for the analysis of vibration and energy flow in cylindrical shells with and without internal fluid.* Journal of Sound and Vibration, 271, 815–847, 2004.

Appendix CD A

In this appendix the table of content for the files included on the CD is presented. Notice that each section in the appendix table of content refers to a folder on the CD with a similar name. Again the sub-sections refer to either the program/file or a sub-folder.

A.1 Animations of CFD-data

Animations of the pressure and velocity in x, y and z direction for one revolution of the impeller. Animations shown for both nominal load, $Q100$, and 5% of nominal load, $Q5$.

A.2 Animation of modeshapes for thin shell

Animations of the modeshapes of a cylindrical finite shell subjected to free-free boundary conditions. Animations are shown for $m = 1,2,3,4$ at the corresponding frequencies $f = 1326$, 1256, 1360, 1485Hz.

A.3 Pipe model - Ansys

Input model for Ansys APDL used to extract the resonances from Ansys in the comparison between models. The boundary conditions are chosen as free-free.

A.4 Experimental set-up

Pictures for documentation and verification of the experimental set-up. Includes pictures for both thick and thin shell experiments.

A.5 Experimental results

Results for the thick shell. Raw data from all experiments provided as .png and .pdf pictures. Raw data for the thick shell corresponds to flexural vibration, $m = 1$.

A.6 Brüel & Kjær - Components

Data sheets for components used through out the experiments. Includes detailed specifications for accelerometers, modal hammer microphone etc.

A.7 Results from uncertainty study in modal decomposition

Complete set of data retrieved from the uncertainty study presented in section 4.5.3.

A.8 Report

The report in digital form as Portable Document Format i.e. pdf-format.

Details to improvements of the vibro-acoustic model

B

B.1 Notes on calculating the dispersion curves

This section includes supporting and elaborated discussions related to the existing discussion in the thesis.

B.1.1 Introduction to the problem

To introduce the issues that makes the convergence rate of the roots and the convergence itself a challenging problem the distribution of the two formulations of the dispersion equation are discussed briefly in the following; distinguished by the distribution in the real and complex domain. Notice that these issues are solely related to introducing an acoustic medium inside the shell as this medium carries and infinite number of waves, nonetheless with the vast majority being decaying waves.

Coefficients of the dispersion equation

Entries of the system matrix for the governing linear system of equations are seen in (B.1).

$$\begin{aligned}
d_{11} &= -k^2 + \frac{1-\nu}{2}m^2 - \Omega^2 \qquad d_{12} = -\frac{1+\nu}{2}km \qquad d_{13} = -\nu k \\
d_{22} &= -\frac{1-\nu}{2}k^2 + m^2 - \Omega^2 + \frac{h^2}{12R^2}\left[m^2 - 2(1-\nu)k^2\right] \\
d_{23} &= m + \frac{h^2}{12R^2}\left[m^3 - (2-\nu)mk^2\right] \\
d_{33} &= 1 + \frac{h^2}{12R^2}\left(k^2 - m^2\right)^2 - \Omega^2 - \widetilde{\rho}\Omega^2\frac{R}{h}J_m(\kappa)\left[\frac{\mathrm{d}J_m(\kappa\widetilde{r})}{\mathrm{d}\widetilde{r}}\bigg|_{\widetilde{r}=1}\right]^{-1}
\end{aligned} \tag{B.1}$$

The associated non-dimensional parameters are in this thesis defined as in equation (B.2).

$$\Omega^2 = \frac{\rho_{str}(1-\nu^2)\omega^2R^2}{E} \qquad \wedge \qquad \kappa^2 = k^2 + \Omega^2\widetilde{\gamma}^2 \qquad \wedge \qquad k = k_{dim}R \tag{B.2}$$

$$\widetilde{r} = \frac{r}{R} \qquad \wedge \qquad \widetilde{\rho} = \frac{\rho_{fl}}{\rho_{str}} \qquad \wedge \qquad \widetilde{\gamma} = \frac{c_{str}}{c_{fl}} \qquad \wedge \qquad c_{str}^2 \equiv \frac{E}{\rho_{str}(1-\nu^2)}$$

Distribution of real roots

As outlined in [Ledet et al., 2015] the real roots are decaying waves thus they contribute to the distribution in the transition phase between the near and far field response and they are governed by the presence of the fluid. Mathematically, the real roots are governed by the

oscillating behaviour of the Bessel-functions as indicated in figure B.4.
The effect of f_1 and f_2 are on the other hand insignificant to the real roots at large wave-numbers as they in general contain non or few real roots and solely at small wave-numbers after which they increase rapidly in $\mathbb{R}$. This is illustrated for an arbitrary Ω within the relevant frequency range in figure B.1 and B.2.

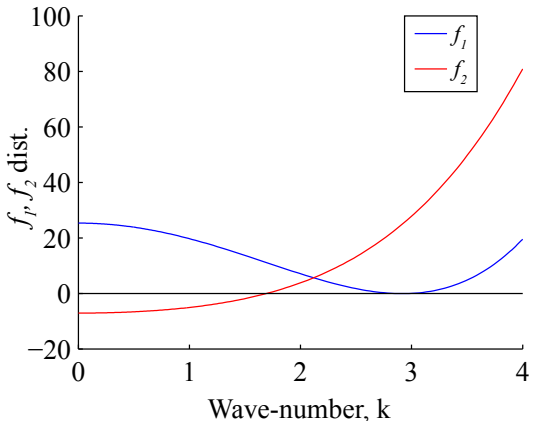

Figure B.1. Distribution of f_1 (blue) and f_2 (red) in k at an arbitrary frequency in the range of interest. As seen there are only few real roots and only at low wave-numbers.

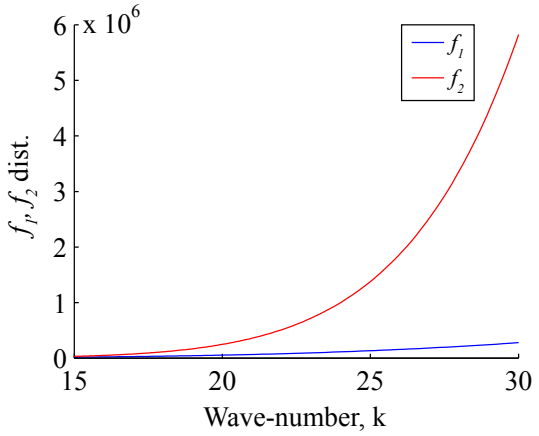

Figure B.2. Distribution of f_1 (blue) and f_2 (red) in k at an arbitrary frequency in the range of interest. The functions grows rapidly at relatively low wave-number and f_2 significantly more than f_1, which immediately suggests that the roots of the derivative of the Bessel-function will govern the real roots of the dispersion equation.

As seen in the left figure the terms f_1 and f_2 at this arbitrary frequency contains few real roots and as seen at a low wave-number. In the right figure it is seen that the magnitude of both terms are large at relatively small wave-numbers. As the magnitude of f_2 is significantly larger than f_1 the term associated with f_2 (the derivative of the Bessel-function) will govern the higher order wave-numbers. On the other hand, as this rapid increase takes place just after the roots of f_1 and f_2 (if there are any) only the first root of the Bessel-functions is affected by these roots whereas the second root of the derivative of the Bessel-function will govern the root of the dispersion equation as f_2 at this point is substantially larger than f_1.

As a final remark the real root of the terms presented in the figure travel along k with increasing frequency i.e. the Bessel-functions will govern the real roots completely at low frequencies as f_1 and f_2 have no real roots at low frequencies. This seems to be a generic property and the real roots of f_1 and f_2 will therefore contribute more and more to the distribution of the first real root of the dispersion equation for increasing frequencies. Finally, notice that the distribution of f_1 and f_2 changes depending on the circumferential wave-number of interest but equally generic properties can be observed for these.

Based on figure B.3 the discontinuity is indeed evident (blue) and as might be obvious to the reader the real roots are more or less impossible to retrieve from the original dispersion equations due the poor conditions created by the discontinuity.

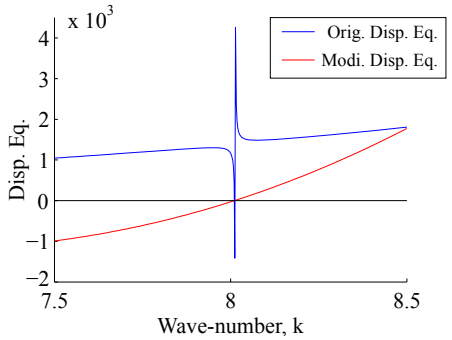

Figure B.3. Distribution of the original (blue) and modified (red) dispersion equation. Notice that the root and the pole of the original dispersion equation are almost coincident.

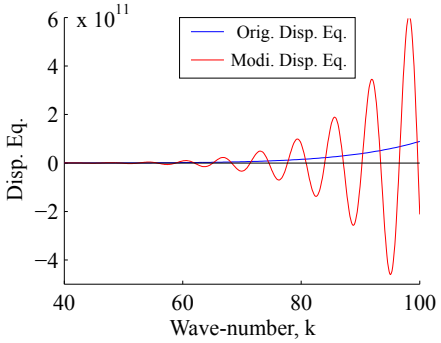

Figure B.4. Distribution of the original (blue) and modified (red) dispersion equation. The modified dispersion equation is unfortunately growing rapidly caused by f_2; thus creating an ill-conditioned system.

For example consider the case when $\Omega \to 0$. This reduces the original and the modified dispersion equation to

$$\begin{aligned} \text{Original:} \quad & f_2(m,k,\Omega \to 0) = 0 \\ \text{Modified:} \quad & f_2(m,k,\Omega \to 0) k \frac{\mathrm{d}J_m(k)}{\mathrm{d}k} = 0 \end{aligned} \tag{B.3}$$

In these equations it is obvious that the original formulation of the dispersion equation does not capture the real roots related to the derivative of the Bessel-function and according to the original formulation there exist a finite number of roots in the vicinity of $\Omega = 0$. The modified dispersion does on the other hand capture the real roots as the derivative of the Bessel-function. This example may be the simplest possible, however this is generic throughout the span of Ω and therefore the real roots are nearly impossible to retrieve from the original formulation.

To be more precise the mathematical difficulties of finding the roots is actually not related to the discontinuities as much as it is related to colliding zeros and poles. On the other hand this knowledge provides us with a powerful tool for approximating the real roots which is skipped for now as it is treated in detail in the upcoming section.

Physically, this collision enlighten us that the shell is considered rigid compared to the fluid and the shell does thereby act as an acoustic duct (the dispersion equation for an acoustic duct is given as: $J'_m(\kappa)\kappa = 0$), meaning that the large decay rate of the wave-numbers is not felt by the slow oscillations of the shell.

The real roots in the modified dispersion equation are on the other hand much more pronounced as seen from figure B.3 and B.4. However, as the amplitudes are increasing rapidly and the oscillation frequency decreasing towards 2π with increasing wave-number the gradients in the vicinity of the roots turn towards infinity and thus creates an ill-conditioned system that will be affected by numerical accuracy.
Given this knowledge it immediately suggests that the convergence of the roots are to be measured in the step-size-tolerance of the roots rather than in the function-value-tolerance since root tolerances in the order of 10^{-6} will provide very large function values at large roots. This should also be evident from figure B.4.

Alternatively the rapidly increasing amplitude can be avoided by multiplying the modified dispersion equation of (2.3) by $[f_2(m,k,\Omega)\kappa]^{-1}$. This does however introduce a discontinuity

at frequencies where f_2 or κ contains real roots and will tend to hide the first real root at these frequencies.

Distribution of purely imaginary roots

As again outlined in several references including [Ledet et al., 2015] the purely imaginary roots represent the propagating waves that carries the vibro-acoustic energy in the far field.

The discussion related to the complex roots is slightly more advanced than for the real roots as the complex roots are generally not related to specific terms of the formulation of either equation (2.2) nor (2.3) as is the case for the real roots. That is; the complex roots are much more sensitive to the physical parameters and the frequency of interest. On the other hand it might be possible to locate the governing terms by application of Rouche Theorem. This is nonetheless found out of scope at the time and the discussion regarding the distribution of the complex roots will thereby be limited.

In general the complex roots belong to f_1, f_2 and κ as the Bessel-function of first kind, J_m, does not contain complex roots on its own i.e. there is a confined number of roots in $\mathbb{C}$ at a given frequency and not an infinite number as in $\mathbb{R}$. On the other hand it can be argued that there also exist an infinite number of purely imaginary roots which is, however, only true at $\Omega \to \infty$. This statement is easily be supported by equation (B.4), illustrating the wave-numbers for an acoustic duct.

$$k^2 = \kappa^2 - \tilde{\gamma}^2\Omega^2 \qquad \Rightarrow \qquad k_n^2 = (j'_{m,n})^2 - \tilde{\gamma}^2\Omega^2 \tag{B.4}$$

where the $j'_{m,n}$ is the n^{th} root of the derivative of the first Bessel-function of order m and $\tilde{\gamma}_m$ and Ω is defined as in equation (B.2).

Supported by the previous discussion of the dispersion of real roots equation (B.4) formally proves that at low frequencies the vast majority of the roots are real. However, as Ω turn towards infinity the vast majority of the roots become purely imaginary and further the equation also formulates the asymptotic cut-on frequency for the propagating waves.

As illustrated in figure B.3 it is obvious that the collision of the zeros and poles play an important role for the real roots. However, since the original dispersion equation does not contain coincident zeros and poles in $\mathbb{C}$ it does not cause problems using this equation for the complex roots. In fact it turns out to be favourable to use this equation over the modified equation and especially at large complex wave-numbers. This is caused by the fact that instead of scaling each term of the modified dispersion equation when k increases in $\mathbb{C}$ the Bessel-fraction of the original equation ensures that the equations are not scaled unintentionally as the fraction is approximately 1 at small ik and turns hyperbolic towards zero as ik increases (the discontinuities are disregarded in this discussion as the roots are not close to these). Effectively this improves the numerical accuracy and suggests that large purely imaginary roots will be governed by the imaginary roots of f_2. Likewise, this observation suggests that the imaginary roots will converge towards the imaginary roots of f_2 for increasing Ω.

Distribution of complex roots

The complex roots have properties similar to the decaying waves, however with an attenuating oscillating behaviour rather than decaying. For the complex roots it is even more difficult to generalise the distribution of the roots, however it is observed that at least one pair of

conjugated roots departs from $\Omega = 0$ and the remaining complex roots operate as transistors between real and purely imaginary roots. This observation is considered sufficient as we have already discussed the distribution of the real and purely imaginary roots.

Additional observations

In conclusion it was also found that when solving for the roots in either of the dispersion equations some roots are more pronounced than others and factorisation of the polynomial roots is therefore a necessity to achieve convergence. Based on this investigation it is suggested to only factorise out the root that is closest and in the same domain ($\mathbb{R}$ or $\mathbb{C}$) as the sought root. Factorising out all roots regularly will create a severely discontinuous/singular equation and thus an ill-conditioned system that again affect the solution time. Doing a full factorisation of the roots is thereby not recommended.

B.1.2 Approximating the roots

Now that we have acknowledged the issues of the dispersion equation the problem to be solved from the view point of inverse source characterisation or, in general, optimisation is; how to efficiently approximate the roots or at least qualified initial guesses at *arbitrary* circumferential wave-numbers and frequencies. This discussion is again distinguished by approximations for complex and real roots.

Complex roots The issue of approximating the complex roots is more extensive than that and is actually worth its own project, however supposedly at a Mathematical Department. Unfortunately, the investigation in this project has not lead to any sustainable solution, thus only experiential guidelines are given here. In the low frequency range, say $\Omega = [0; 0.5 - 1]$ depending on the physical parameters and at low circumferential wave-numbers, say $m = [0; 4]$, the complex wave-numbers may favorably be sought at the complex roots of f_1, f_2 and κ. At larger frequencies and large wave-numbers the complex roots may be sought solely at f_2 confer to the previous discussion on the distribution of the dispersion equation.

In addition, the roots found in f_1, f_2 can be corrected by a Newton-Raphson scheme or by a scheme including second order information (the derivative of the dispersion equation is readily available) to improve the initial guesses. This might nonetheless be redundant when applying stable and well-documented search-algorithms. However, by altering between the different formulations of the dispersion equation this may be a neat trick.

Real roots In approximating the real roots at arbitrary circumferential wave-numbers and frequencies several methods have been detected through this investigation from which only the two top performers are presented here.

1) The first method is simply based on approximating the roots as the roots for an acoustic duct as presented in equation (B.4). These will be referred to as the corrected roots of the derivative of the Bessel-function in the following. This approximation is very simple and converges towards the real roots of the dispersion equation, thus the error decreases for increasing roots. Nonetheless, the first real roots will be poorly approximated.

2) The second method is based on the idea of estimating the roots through a linear combination of the individual roots of the Bessel-functions as shown in equation (B.5).

$$\tilde{k}_n = w_{2n} j'_{m,n} + w_{1n} j_{m,n} \tag{B.5}$$

where w_{1n} and w_{2n} are the weighting functions for the n^{th} root and $\tilde{k}_n$ the approximated root.

The nature of this idea originates from the fact that the real roots, as mentioned previously, are governed by the Bessel-function which then implies that the actual roots of the dispersion equation must be in-between the roots of these Bessel-functions just as illustrated in figure B.5.

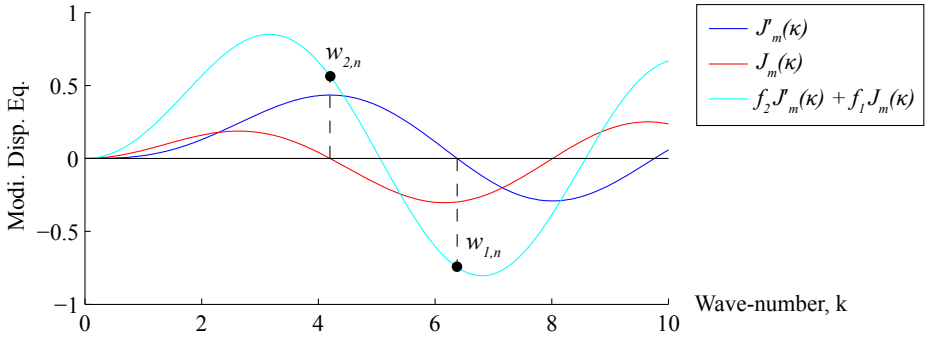

Figure B.5. Principle for calculating the weighting-functions based on the function values at the Bessel-zeros. The blue graph represent the derivative of the Bessel-function while the red represent the Bessel-function itself and the cyan the dispersion equation.

The weightings of the roots are then calculated based on the function values at each Bessel-zero i.e. the points illustrated in figure B.5.

$$\|\text{Disp}\| = f_2(m,k,\Omega)\kappa \frac{\mathrm{d}J_m(\kappa)}{\mathrm{d}\kappa}\bigg|_{k=\tilde{j}_{m,n}} + f_1(m,k,\Omega)\frac{\tilde{\rho}\Omega^2 R}{h} J_m(\kappa)\bigg|_{k=\tilde{j}'_{m,n}}$$

$$w_{2n} = \frac{f_2(m,k,\Omega)\kappa \frac{\mathrm{d}J_m(\kappa)}{\mathrm{d}\kappa}\Big|_{k=\tilde{j}_{m,n}}}{\|\text{Disp}\|} \qquad w_{1n} = \frac{f_1(m,k,\Omega)\frac{\tilde{\rho}\Omega^2 R}{h} J_m(\kappa)\Big|_{k=\tilde{j}'_{m,n}}}{\|\text{Disp}\|} \tag{B.6}$$

where $\tilde{}$ indicates corrected Bessel-zeros i.e. $\tilde{j}'_{m,n} = \sqrt{(j'_{m,n})^2 - \tilde{\gamma}^2\Omega^2}$ and $\tilde{j}_{m,n} = \sqrt{(j_{m,n})^2 - \tilde{\gamma}^2\Omega^2}$.

To validate the quality of the approximations they are validated against the actual real roots of the dispersion equation, all shown in figure B.6 for $m = 3$.

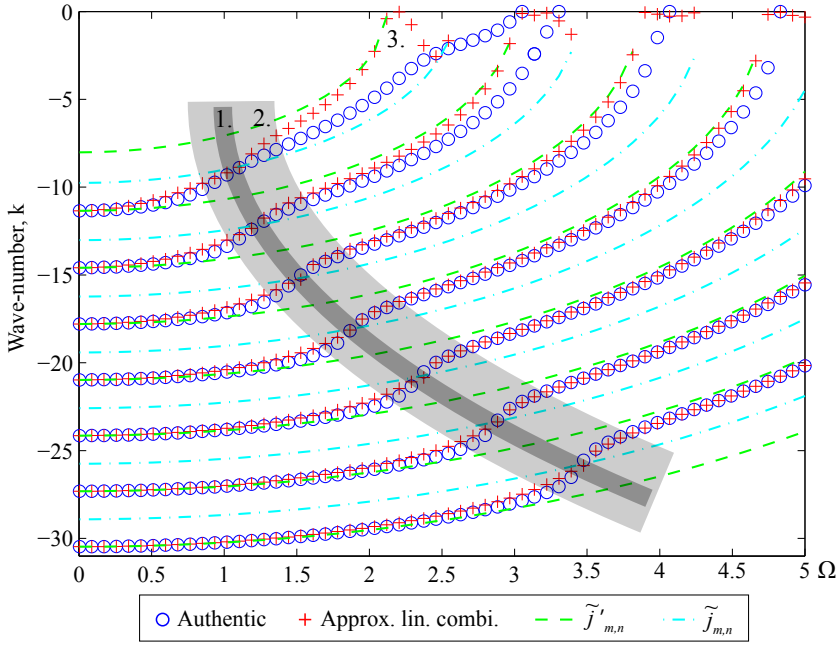

Figure B.6. Dispersion of real roots at $m = 3$. Blue o indicates the authentic roots of the dispersion equation, red + the approximation by a linear combination of the Bessel-zeros while the green – – and cyan –· are the corrected Bessel-zeros of the derivative and the Bessel-function itself.

From the figure it is seen that the simple approximation by the zeros of the derivative of the Bessel-function is a good approximation at large wave-numbers when confined by the left edge of the region indicated by 2. Through the illustration in figure B.6 it is obvious that the term "large wave-numbers" is not a uniquely defined threshold as it is determined by the frequency as well. This investigation has however lead to the following rules of thumb for using this simple approximation of the real roots at any circumferential wave-number.

$$k_n \approx \tilde{j}'_{m,n} \qquad \text{for} \quad |k| > 10\Omega \tag{B.7}$$

Inside the band indicated by 2 the simple approximation role off the authentic roots but only for approximately $0.5 - 1\Omega$ after which they once again converge towards the zeros of the derivative of the Bessel-function however with a lag of "phase" such that it drops to a zero of one order lower than before the shift. This is accounted for through the rule of thumb in equation (B.8).

$$k_n \approx \tilde{j}'_{m,n-1} \qquad \text{for} \quad 7\Omega > |k| > \max\{2m, 5\} \tag{B.8}$$

On the other hand the approximation by a linear combination is a very good and robust approximation that provides extremely good results for all circumferential wave-numbers and does in fact also capture the sudden "phase" shift with a high accuracy. In general this solution is indeed considered good in the same range as the simple solution however also including the "phase" shift region i.e.

$$k_n \approx w_{2n} j'_{m,n} + w_{1n} j_{m,n} \qquad \text{for} \quad |k| > \max\{2m, 5\} \tag{B.9}$$

and for high frequencies even substantially below 5 as well.

Notice that for waves that flatten in the transformation from real to complex waves indicated by 3. in figure B.6 the linear combination approximation is not sufficient. This is anticipated

to originate from interference of the real roots from the terms f_1 and f_2 and here the real roots are to be sought directly in the dispersion equation.

Now we direct the focus towards the "phase" shift indicated in region 2 of figure B.6. This phenomenon has come to be a surprising event in the dispersion of the waves as this enlighten us that each wave in a specific spectrum transform from seeing the waveguide as an acoustic duct to seeing the waveguide as a more compliant shell. Particularly in region 1 the waveguide can be interpreted as a shell with a pressure release boundary condition.

Comments on approximation errors

Finally, it is of interest to discuss the consequences of fault estimations of the real roots e.g. when the approximations role off the authentic values. In general at large real roots the error between the approximated and the actual roots are insignificant. First off all the absolute error will never be higher than π and thereby cause a decreasing relative error. Second of all the amplitudes of the response at these high wave-numbers are very small and usually insignificant compared to the complex and the first few real roots i.e. the accuracy of these large valued real roots does supposedly not change the picture of the power flow or response and does neither cause oscillations in the total power flow.

For the first few real roots it is of much greater importance that the approximations are acceptable as these are governing in the transition and energy re-distribution from the near field to the far field power flow. It is thereby suggested to calculate these in the modified dispersion equation with the approximations as initial guesses and then apply the approximations for the higher real roots say, from the second to third root and up.

B.1.3 Searching the roots

With reasonable approximations for the large real roots it is now of interest to efficiently calculate the complex and first few real roots. Based on the issues discussed until now the problem is twofold: 1) how do we successfully search for the roots i.e. quantify the initial guesses and 2) how are do we subsequently solve for the roots.

Given that modern commercial mathematical software contains a wide range of pre-implemented search/root-finding algorithms these are facilitated directly as solvers throughout this section and the issue, which is nonetheless be most challenging issue, reduce to retrieving qualified initial guesses. With the previous discussion on discontinuities and ill-conditioned systems in mind it is more crucial, from the view point of computational efficiency, to provide good initial guesses than advanced algorithms and in fact very basic numerically algorithms will suffice as long as the initial guess is good. This is treated further in section B.1.4.

Previous strategy for initial guesses

In the previous project conducted on 9^{th} semester the roots were sought by utilising the roots solve for in a $20^{\text{th}} - 24^{\text{th}}$ order Taylor series approximating the dispersion equation at each discrete frequency and expanded around $k = 0$. These roots were then used as initial guesses in the original dispersion equation to search for the complex roots. This terminates in 10-12 initial guesses (double roots are present) to find, at most, 5 complex roots.

Even though these guesses were rather close and the roots were factorised regularly out of the dispersion equation specific roots did not converge. Thus the Taylor approximation needed to be either moved to another expansion point (creating single roots i.e. 20-24 guesses) or increased in degree. As might be obvious this is indeed not a very computationally efficient method but is however, to the authors knowledge, a common procedure because the root are usually only to be calculated once.

Regarding the real roots the Taylor series do not span sufficiently wide to retrieve initial guesses for the real roots. These were thereby sought separately from the complex roots in the modified dispersion equation with the initial guesses of $j_{m+1,n}$ i.e. the roots of the Bessel-function of one order higher than the Bessel-function included in the dispersion equation (they converge rather fast towards the roots of the derivative of the Bessel-function). This is on the other hand a much better procedure for finding the real roots but then again searching every root in the dispersion equation is a computationally expensive procedure compared to approximations by function evaluations and weighting functions.

Proposed strategy for initial guesses

Instead of the previous strategy for calculating the initial guesses this investigation has lead to another and more sustainable method for these initial guesses. The method is based on a linear extrapolation of the roots at previous Ω to retrieve a qualified initial guess for the given frequency. Thus this method is unfortunately not valid at arbitrary frequencies as is the case for the previous strategy. Nonetheless this method holds greater potential as 1) each root is sought at only one guess not at several 2) the computational costs for calculating the initial guesses are significantly less than previously and 3) the dispersion curve is indeed continuous and smooth in Ω, as seen in figure B.7, and we can thereby ensure that every root is found by introducing simple rules.

To calculate the first set of initial guesses it is advantages to start at $\Omega = 0$ as the modified dispersion equation reduce conveniently to that shown in (B.3) and the first set of roots is thereby easily found. The second set is conveniently sought at the same initial guess; provided that the step-size in Ω is no too large.

The remaining sets of initial guesses are then sought as a linear extrapolation of roots at the latter two frequencies as indicated in (B.10).

$$\tilde{k}_n = \frac{\tilde{k}_{n-1} - \tilde{k}_{n-2}}{\Omega_{n-1} - \Omega_{n-2}} \Delta\Omega + \tilde{k}_{n-1} \tag{B.10}$$

where $\Delta\Omega$ is the current step-size.

Alternatively, the remaining guesses can also be sought at the roots of previous Ω; again provided that the step-size is not too large. On the other hand this extrapolation of the roots is complimentary from the view point of computational efficiency and might cause the solver to converge in less iterations. Finally, remember that factorising out the closest root and applying different formulations of the dispersion equation is essential for convergence to be successful.

Rules that ensures convergence

To ensure that every root at every Ω is caught we introduce a set of rules constructed to enforce convergence of the solver.

To support the understanding of the rules it is favourable to take interest in the dispersion diagram shown in figure B.7 as most of the rules are illustrated here.

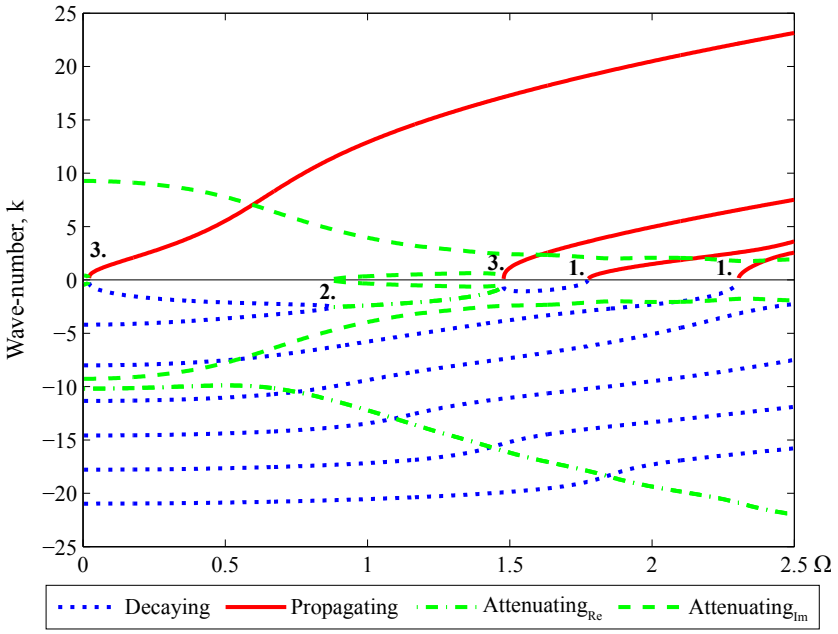

Figure B.7. Dispersion curve for $m = 3$ and the parameters of table 2.1. The blue ··· wave-numbers are decaying waves (real roots), the green – – and – · – are attenuating waves (complex roots) and the red – are propagating waves (purely imaginary).

As mentioned earlier the roots disperse smooth and continuous in Ω, why the extrapolation method presented above provides very qualified initial guesses for the roots. However, as the extrapolation does not capture the shifting between the domain $\mathbb{R}$ and $\mathbb{C}$ certain rules must be implemented to correct the initial guess when the roots change domain. Several of the transitions between the domains are directly visible in figure B.7.

The rules are constructed based on the physical understanding of the transformation between waves.

1. Whenever a real root turn to zero it transforms into a purely imaginary root which depart from zero - see figure
2. Whenever two real roots collide they transform into a pair of complex conjugated roots where the imaginary branch depart from zero and the real branch depart from the point of collision - see figure
3. Whenever both the imaginary and real branches of a pair of complex conjugated roots turn to zero simultaneously they transform into a purely imaginary root and a real root both with departure from zero - see figure
4. Whenever the imaginary branch of the paired complex conjugated roots turn to zero the roots transform into a purely imaginary root with departure from zero and a real root with departure from the real part of the complex root and vice versa - not seen in the figure
5. A purely imaginary root does not transform back

In accordance to these rules we can explicitly quantify when these roots are about to change by solving the modified dispersion equation of (2.3) for Ω at $k = 0$ and similarly introduce tolerances on when real roots collide, when branches of the complex roots turn to zero etc.

Fortunately, this allow us to predict changes between domains and thus introduce a variable Ω step-size whenever in the vicinity of these transitions phases. Likewise, it is possible to apply the transition-rules and correct the initial guess to enforce convergence of the roots.

General comments

In summary the methodology proposed based on this enhanced investigation of the dispersion equation is indeed more sustainable than the method applied on the 9^{th} semester as we employ simple rules to correct the initial guesses to the relevant domains and thus we increase the convergence markedly. In relation to these qualified initial guesses it is expected that one iteration of the simple Newton-Raphson scheme will suffice with respect to the desired accuracy if the Ω step-size is sufficiently small. Thus a commercial search algorithm is avoided. If it is on the other hand desired to use commercial search algorithms be aware of the tolerances confer to the discussion on "infinite" gradients and ill-conditioned systems caused by the oscillating, rapidly growing function as discussed in section B.1.1. If e.g. the function value tolerance is too small the computational time increase unintentionally compared to what is gained.

Finally, the proposed method is not optimal from the view point of optimisation as we need to calculate the full dispersion curve for every change in the parameters. Nonetheless, an efficient method for improving this is treated in the upcoming section such that the full dispersion curve is only to be calculated for the initial physical parameters.

B.1.4 Correcting the roots

At this point we have acceptable approximations for large valued real wave-numbers and a sustainable method for calculating qualitative initial guesses to find the complex and first few real roots of the dispersion equation. Nevertheless, a method that is not only sustainable but equally fast in an optimisation sense is sought; meaning that when the physical parameters change the influence on the roots must be approximated.

The idea is simply to correct the roots of interest by a simple Newton-Raphson scheme, as shown in (B.11), every time the physical parameters change.

$$k_{n+1} = \tilde{k}_n - \frac{f(\tilde{k}_n)}{f'(\tilde{k}_n)} \tag{B.11}$$

where $\tilde{k}_n$ is the previous root (or initial guess), $f(\tilde{k}_n)$ the dispersion equation evaluated at $\tilde{k}_n$ and $f'(\tilde{k}_n)$ the derivative of the dispersion equation evaluated at $\tilde{k}_n$ - remark that the derivative of the dispersion equation is given analytically.

This is indeed a sustainable method if the step-size in Ω is sufficiently small, the physical parameters change slowly from iteration to iteration and, from an optimisation view point, if the initial physical parameters are chosen in the same range as the optimum.

As a side comment it has been found that the correction by this Newton-Raphson scheme should be done based on the modified dispersion equation also for the complex roots, as it seems that numerical accuracy will affect the correction if the roots are close to the discontinuity.

B.1.5 Summary

If the assumptions discussed in the previous sections are satisfied the complete procedure for determining the roots can be outlined as follows:

1. Calculate the complete dispersion curve based on the procedure outlined in section B.1.3 including only the complex roots and the first 2-3 real roots according to the rule of thumbs found in section B.1.2
2. Choose the frequency of interest and find the frequency range in the dispersion curve surrounding the chosen Ω i.e. find n such that $\Omega_n \leq \Omega \leq \Omega_{n+1}$. Otherwise, define a spectrum of frequencies
3. Do a linear interpolation between Ω_n and Ω_{n+1} of the roots to estimate the roots at Ω
4. Correct the roots by a Newton-Raphson scheme (remember that the derivative of the dispersion equation can be derived explicitly). If a spectrum of frequencies are of interest correct the roots at all frequencies. This is computationally cheap if the assumptions above are fulfilled
5. Approximate the remaining desired number of real roots by either of the methods outlined in section B.1.2 at the chosen frequency(ies)
6. Save the corrected roots if the purpose is optimisation and go to step 2

A sustainable and fast method ideal for optimisation, detailed power flow analysis, parameter study, model uncertainties and inverse source characterisation has been proposed.

B.2 Arbitrary time-harmonic excitations - Additional graphs

Comparison of the power flow calculated with a delta-function, figure B.8, and with a probability function for $\sigma = 0.1$, figure B.9, applied in the acoustical velocity field at $r_0 = 0.5$.

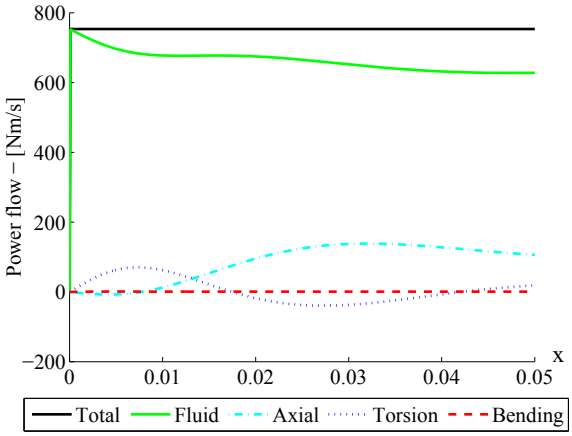

Figure B.8. Delta-function applied in the acoustical velocity field at $r_0 = 0.5$, $f = 67.8$kHz and $m = 3$ with 25 waves retained.

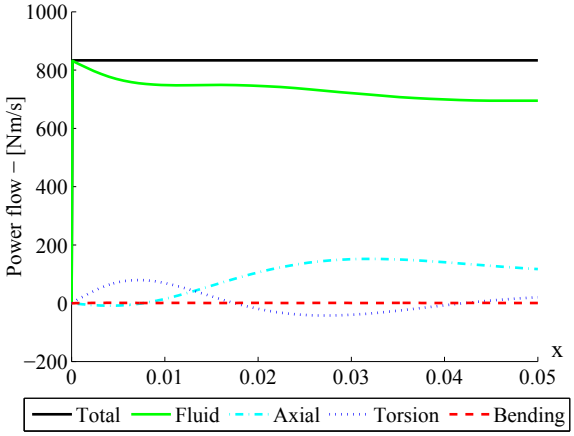

Figure B.9. Probability function with $\sigma = 0.1$ applied in the acoustical velocity field at $r_0 = 0.5$, $f = 67.8$kHz and $m = 3$ with 25 waves retained.

As seen the probability function with a low intensity has a higher total power flow than that of a delta-function. This might be unexpected at first but is actually explained through the studies in section 3.3.3.

Figure B.10 illustrates the real and imaginary part of the velocity profile evaluated at $x = 0.01$m and figure B.11 the real and imaginary part of the pressure profile also evaluated at $x = 0.01$m

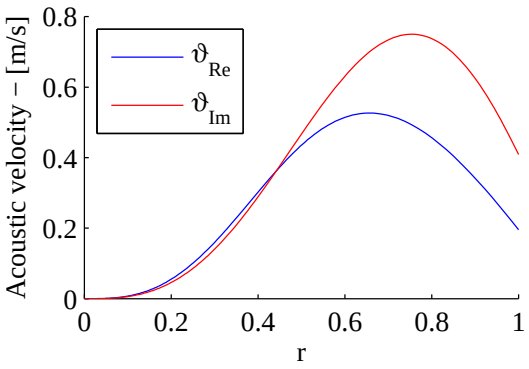

Figure B.10. Velocity profile similar to that of figure 2.7 but evaluated at $x = 0.01$.

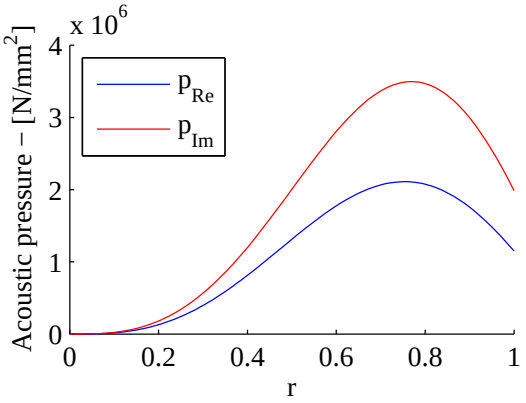

Figure B.11. Pressure profile similar to that of figure 2.8 but evaluated at $x = 0.01$.

Map quality by error estimations - Details

C

To ensure high quality of the map it is crucial that the error between the data sets are estimated such that the possibility of sorting out critical modal information during the data processing is reduced. In the following we will focus on the axial velocity as it is significantly more cumbersome to qualify the map for this field variable because it is difficult to provide qualified measures useful for final conclusions.

Comparing the mapped data directly with the FFT-data is at first not an easy task as the grid nodes and the CFD nodes are not necessarily coincident. This is however circumvented by creating an unstructured grid coincident with the original mesh of the CFD-data and map, again by a linear interpolation, the already mapped data back onto this mesh. Now we are able to compare the original FFT-data directly with the double mapped data and evaluate on the differences between the two data sets. That is; we interpret the error based on the grids ability to recreate the original data in a double mapping procedure. Both the original and double mapped data sets are illustrated in figure C.1 and C.2 for $Q100$ at $f = 25$Hz with the mapped data based on the 16x10 grid presented in figure 3.8.

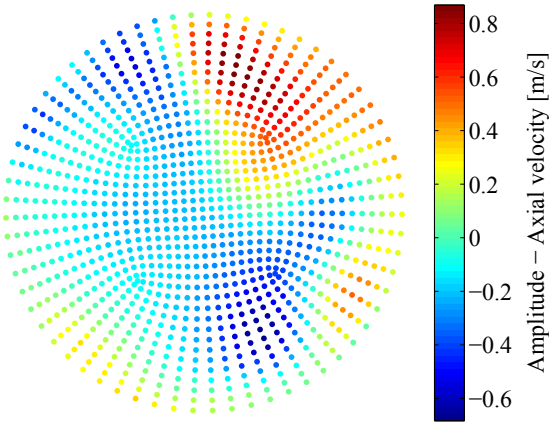

Figure C.1. Axial velocity amplitudes at $f = 25$Hz for $Q100$.

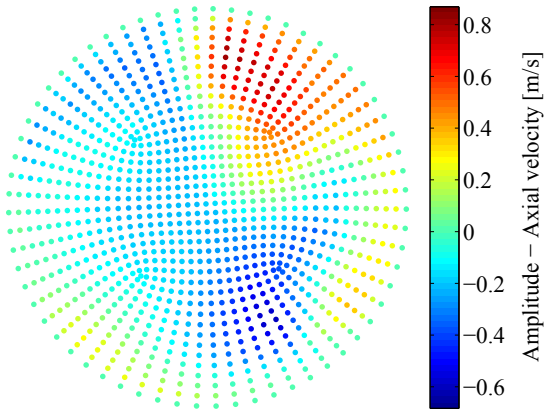

Figure C.2. Double mapped axial velocity amplitudes based on the 16x10 grid of figure 3.8 and the data shown in figure C.1.

In comparison between the two figures it is clearly difficult to distinguish the two data sets by the naked eye and it may seem that the grid data is able to fully recreate the original FFT-data. However, this only holds true if the structured grid is significantly larger then the original mesh i.e. $N_{grid} >> 1057$ and maybe not even then. Thus we need a qualified measure to highlight the error.

Notice first of all that the values of figure C.1 has a shift in the sign, which makes the relative

error a poor measure as the values approach zero. Hence the residual is instead used as an initial error estimator. Second of all notice that the data points in the outermost circumference of the double mapped data shown in figure C.2 is zero. This is pre-specified because these points are outside the domain of the structured grid and to evaluate these in the map, extrapolation is necessary. Alternatively, the outermost points can be specified as identical to the original data, however the zero definition has been adopted in every future error estimation to keep in mind that these are not mapped using this procedure.

Besides keeping the error in the mapping low it is also our intend to keep the computational time low and if possible it is therefore our interest to have a rather coarse mapping grid. Thus the following error estimation is based on the original data shown in figure C.1 and the mapped data in figure C.2 with the rather coarse 16x10 grid. The residual between these are shown in figure C.3 and in figure C.4 the residual is shown for a grid refined by doubling the grid directions i.e. a 32x20 grid.

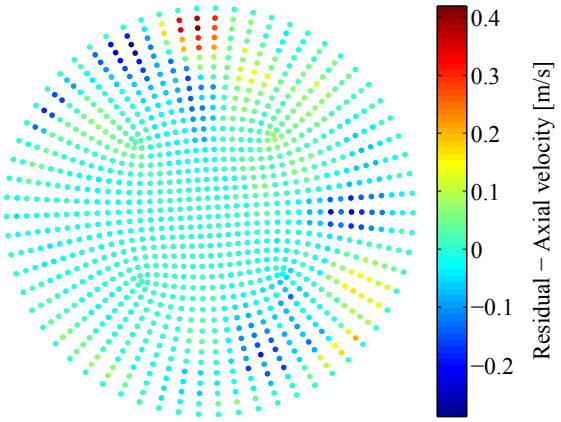

Figure C.3. Residual between the FFT data and the double mapped data. The residual is based on the data of figure C.1 and C.2.

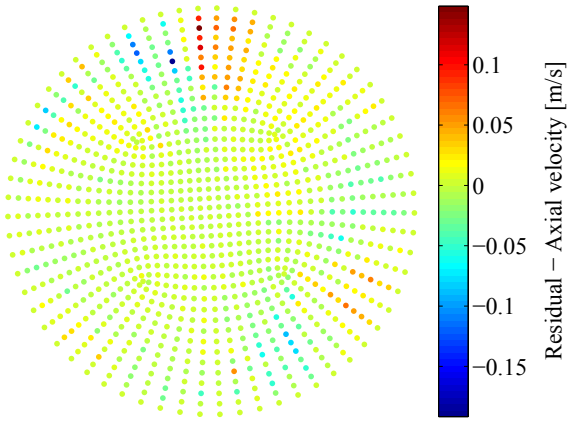

Figure C.4. Residual between the FFT data of figure C.1 and the double mapped data when the grid is refined by doubling the grid directions, hence a 32x20 grid.

In general it seems that the coarse grid contains rather high residuals compared to the actual values of the original in figure C.1 which suggests that the grid should be refined. If the grid is refined it is immediately seen that the residual drops drastically, especially the positive residuals and compared to the values in figure C.1 this grid seem more reasonable.

Notice furthermore that for both grids there is a dense area (at the top left) where both the highest positive and negative residual is placed. In this area there are a distinct change in the amplitudes from positive velocity to negative velocity which is also evident from the original FFT data in figure C.1. At points with such drastic change in the amplitudes it is difficult to fully capture the peaks when interpolation onto a grid with fewer nodes and consequently these points would contain higher errors.

Based solely on the latter residuals it is still difficult to determine the map quality and it is therefore desirable, in some way, to retrieve relative errors. A reasonable way of during this is to evaluate the nodal relative error at $f = 0$Hz, which corresponds to the data integrated over the time of one revolution and effectively it is the static mean axial velocity.

When the pump is performing at its nominal load both the flow and pressure at mean load ($f = 0$Hz) is sufficiently high and there will be no changes in the sign of neither the pressure

nor the velocity field. Consequently, the data is sufficiently far from zero and the relative error is here a qualified measure, however, at the outermost circumference the velocity is small due to the viscosity effects and may affect the quality of the relative error. The original data and the double mapped data is shown in figure C.5 and C.6 for $f = 0$Hz, where the mapped data is based on the 16x10 grid.

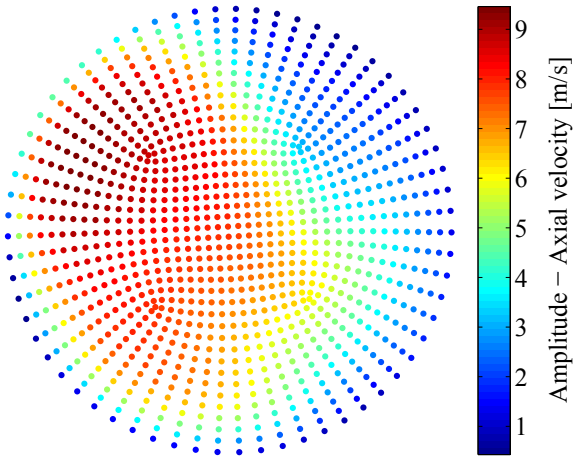

Figure C.5. Axial velocity pulsations at $f = 0$Hz for $Q100$.

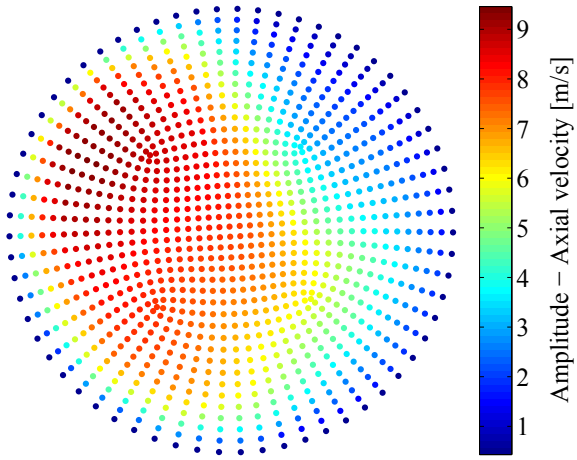

Figure C.6. Double mapped axial velocity amplitudes based on the 16x10 grid and the data shown in figure C.5.

The relative error between the two data sets are prescribed in figure C.7 and in figure C.8 the relative error for the refined 32x20 grid is shown.

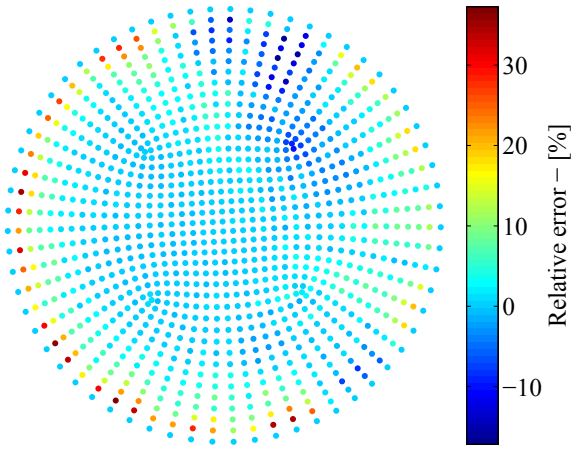

Figure C.7. Relative error between the FFT data shown in figure C.5 and the double mapped data shown in figure C.6 at $f = 0$Hz.

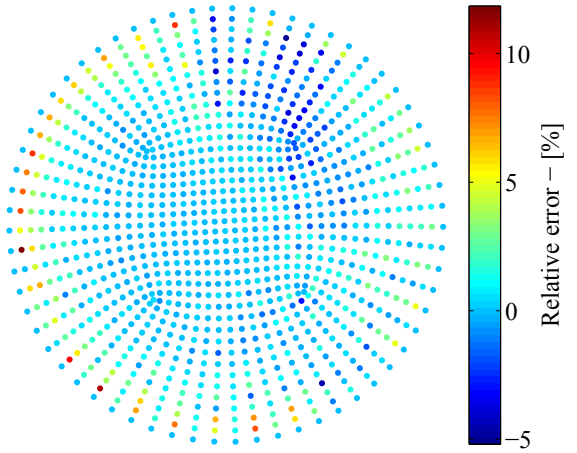

Figure C.8. Relative error at $f = 0$Hz between the FFT data shown in figure C.5 and the double mapped data when the grid is refined to a 32x20 grid (not shown).

As is seen in figure C.7 the relative errors are rather large for the coarse grid. Nonetheless, it is primarily the second nodal circumference that contains the highest positive errors and the explanation is found in the drastic change in the nature of the velocity field where the velocity suddenly drops (due to viscosity effects) from almost maximum to half the magnitude over 1-2 circumferential nodes.

Other significant errors seen in the figure are on the other hand related to the questionable relative measure as the magnitude of the velocity at these points are rather close to zero and

hence distorting the image of the relative error. In relation to the relative error of figure C.8 based on the refined grid similar issues are observed, however the errors have generally dropped to 1/3 of the errors in the 16x10 grid.

Given the recent discussion on the cause of the large relative errors and in conciliation with the residual of figure C.3 it is concluded that the grid should be refined to 32x20 for all frequencies in the axial velocity. This conclusion is supported by the fact that at $f = 25$Hz the amplitudes across the cross section spans approximately 1.4m/s, which corresponds to roughly 16% of the static velocity pulsations. Unfortunately the coarse grid does not predict these peak values sufficiently accurate due to their abrupt nature, thus in order to reduce the possibility of modal leakage in the modal decomposition of the CFD-data it is found important to capture these peak values with a heighten accuracy. Finally, the errors are summed in table C.1, where the errors in this table are based on the complete error i.e. the complete error including both the real and imaginary part.

In extension to the relative errors presented in figure C.7 and C.8 the complementary investigation for the pressure field reveals maximum errors way beyond those for the velocity field which is explained solely by the fact that the field variables are significantly larger than zero providing a qualified relative error estimations. The maximum errors of this investigation are also shown for $f = 0$Hz in table C.1, where the average relative error is the percentage error based on the average of all nodes.

	Absolute err.	Relative err.	Average relative err.
Axial velocity			
Avg. velocity 5.76 m/s		Amp. variation 9.03 m/s	
Grid: 16x10	2.30 m/s	37.34%	6.71%
Grid: 32x10	0.64 m/s	11.85%	6.71%
Pressure			
Avg. pressure 6.15 bar		Amp. variation 0.15 bar	
Grid: 16x10	778.74 N/m^2	0.13%	0.30e-02%
Grid: 32x10	380 N/m^2	0.63e-01%	0.10e-02%

Table C.1. Summary of the error estimation based on two different grid sizes at $f = 0$Hz. The table presents the absolute, relative and average relative complete error i.e. including both $\mathbb{R}$ and $\mathbb{C}$.

With basis in the table it is clear that the pressure is well represented by the coarse grid as the pressure field at $f = 0$Hz is smooth (does not include distinct peaks) and much larger then zero. The coarse grid is therefore indeed found sufficient for the static case presented in the table. Nevertheless, remark that if a given frequency of the pressure field contains distinct peaks it is suggested that the grid is refined here as well. Notice that the pressure field at $f \neq 0$Hz does include $\pm$ amplitudes just as the velocity and the relative error is again useless.

Notice that the behaviour of the velocity and pressure residual will be completely different for other frequencies and this method of error estimation should in principle be done at every frequency. However, if this is investigated in detail it should be possible to locate the most critical frequency with respect to the residual and thus specify the grid based on this frequency. This investigation is however discarded at this point.

In conclusion the structured grid is chosen based on the grids ability to recreate the original data in a double mapping procedure. This mapping raises the immediate issue of how to qualify

the grid as the relative error is a poor measure at most frequency due to sign changes in the amplitudes. The proposed method to qualify the grid size is therefore to conciliate the residual at the given frequency with the relative error at $f = 0$Hz. If the relative error at $f = 0$Hz is above 10-15% it is suggested to refine the mesh. If the relative error is below 10-15% but the span in the amplitudes over all nodes at the given frequency are above 10-15% of the amplitude span at $f = 0$Hz the mesh should be refined if the distribution is governed by peak values. Obviously this should be judged for the individual case and for this specific CFD-data it is proposed that the grid is refined to 32x20 to increase the accuracy near the peak values.

Experimental set-up - Details

D

D.1 Test set-up

The experiments for both specimens are based on measurements of the radial acceleration at chosen positions of the pipe and the boundary conditions are chosen to be free-free conditions as these are relatively easy to simulate in practice. The experimental set-up is sketched in figure D.1 with the components presented in table D.1.

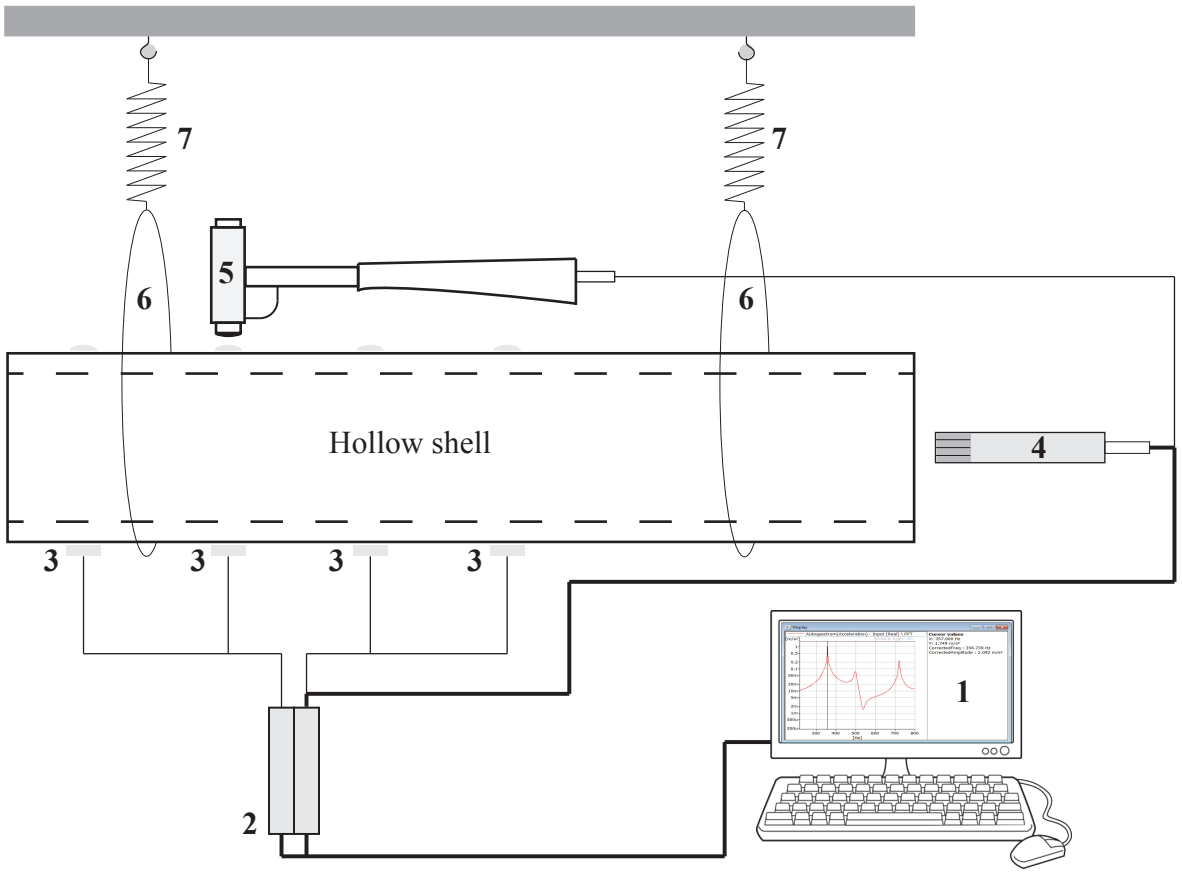

Figure D.1. Sketch of the test set-up. Figures taken from [Brüel & Kjær, 2015; Imagbuddy, 2015].

The hard-/software and other equipment used throughout the experiments are listed in table D.1.

No.	Component	Type	Quantity	Note
		Software from Brüel & Kjær		
1	Fourier analyser	PULSE LabShop		Version 18
		Hardware from Brüel & Kjær		
2	Frontend	3050-B-6/0	2 pcs.	6 Channels
3	Accelerometer	4518-003	10 pcs.	1.5g radial one way acc. (±5% circum. acc.)
4	Microphone	4189-A-021	1 pc.	20Hz to 20kHz
5	Modal hammer	8202	1 pc.	Incl. force transducer
		Other		
6	Suspension line	Fishing line		
7	Spring	Tension spring	2 pcs.	$k = 390\text{N/m}$

Table D.1. Specification of hard- and software used in the experiments. Further information and technical specifications can be found at [Brüel & Kjær, 2015].

Experimental procedure

- The free-free boundary conditions are simulated by hanging the pipes from soft springs (see the spring constant in the table) and fixated in thin fishing line making the system resonance very low in comparison with the first resonance of the free-free vibrating pipe. In fact the system resonance can be approximated by the simple spring-mass-system

$$f_n = \frac{\omega_n}{2\pi} = \frac{1}{2\pi}\sqrt{\frac{k_{eq}}{m}} = \frac{\sqrt{2}}{2\pi}\sqrt{\frac{k}{m}} = \begin{cases} 2.68\text{Hz} & \text{for } f_n^{\text{Thick}} \\ 2.20\text{Hz} & \text{for } f_n^{\text{Thin}} \end{cases} \tag{D.1}$$

- The placements of excitation, accelerometer and suspension are the marked on the pipes and the accelerometers are mounted on the opposite side of the excitation points (if it is possible). The microphone is placed at the end of the pipe close to the termination of the pipe.
- The Fourier analyser is set-up to the accelerometers, microphone and modal hammer and the internal options in the analyser are chosen e.g. frequency range, resolution of discrete frequencies in the FFT and weighting windows to reduce noise and improve quality of the FFT.
- The trigger signal is set to a force range of the modal hammer - determines a minimal and maximal force for which the measurements are started. Furthermore the number of experiments used in averaging are specified to 5.
- Calibration of hardware and initialization of the template to ensure correct connection with frontends.
- Start experiments. Conduct 5 experiments at each excitation point (the averaging is set to 5 measurements throughout all experiments). Excite the specimens at the opposite side and at the same axial location as the accelerometers if possible. If not excite as close to the accelerometers as possible. Placement of accelerometers, excitation and suspension point are shown in figure D.2 and D.5.
- Retrieve data from the Fourier analyser

In the Fourier analyser (PULSE LabShop) software from Brüel & Kjær there exist a wide range of options and specification that can be applied to reduce noise and improve the quality of the FFT. These options where chosen as default options for the impact hammer set-up.
The analyser available at Grundfos has a maximum of 6400 lines, meaning that it can handle up

to 6400 discrete frequencies in the FFT analyser. To ensure a high quality of the measurements and very detailed information of the pipe the frequency range are chosen relatively low, as seen in table 4.1 with all 6400 lines used. This will provide a resolution of 0.25Hz in the frequency range 0 - 1600Hz, which allow a very detailed view and as will be evident in the upcoming section this high resolution allows for immediate conclusions on the symmetry of the pipe and thus for conclusions on the effect of the seam in the pipe.

D.2 Accelerometer, excitation and suspension point placement

Depending on which test specimen used in the experiments the accelerometers are placed differently. For example the thick shell is suspected to vibrate primarily in $m = 1$, why several measurements along the circumference are avoided as modal decomposition is trivial for this case. For the thin shell on the other hand it is important to decompose the measured data into modal responses, thus circumferential measurements are indeed a necessity.

Placements on thick shell

Based on the latter discussion five accelerometers are placed on the thick pipe in a straight line at the reference $\theta = 180°$ as illustrated in figure D.2 with the dimensions shown in table D.2. Notice that accelerometers evenly distributed in the circumferential direction is not a necessity due to the latter assumption on only $m = 1$ modes at the frequency range of interest.

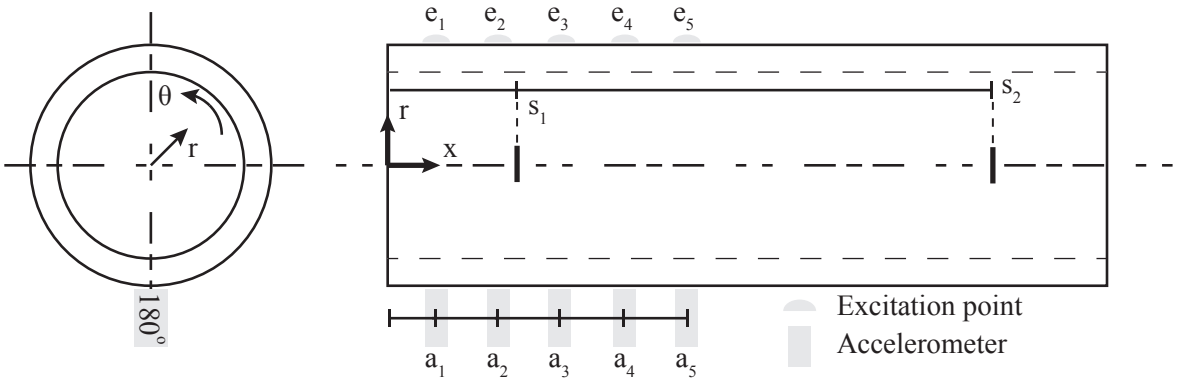

Figure D.2. Sketch of the placement of accelerometers, excitation and suspension points for the thick shell.

In the figure above the accelerometers, excitation and suspension points are all indicated by a, e and s respectively. Further the accelerometers and the excitations points are all located at the same axial distance but placed opposite each other just as illustrated in the figure. This is for the flexural modes equivalent to exciting the measured points.

	Unit	$a_1 \wedge e_1$	$a_2 \wedge e_2$	$a_3 \wedge e_3$	$a_4 \wedge e_4$	$a_5 \wedge e_5$	θ_{acc}	s_1	s_2
Thick shell	mm	16	189	314	485	680	180°	298	985

Table D.2. Dimensions for accelerometers, excitation and suspension points of the thick shell.

The actual experimental set-up can be seen in figure D.3 and D.4. For further documentation on the set-up the attention should be drawn to appendix A.4.

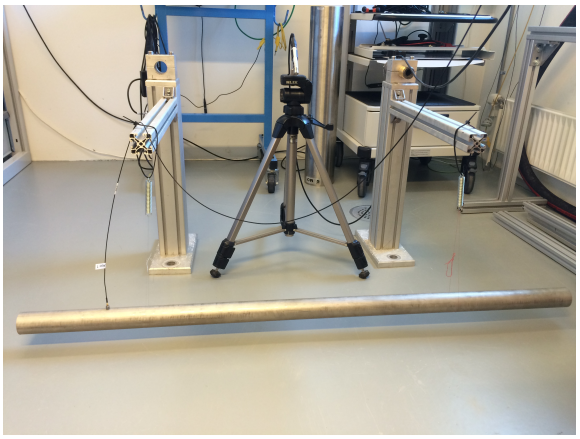

Figure D.3. Experimental set-up for thick shell with only 1 accelerometer attached. Accelerometers added gradually to control effects of mass loading.

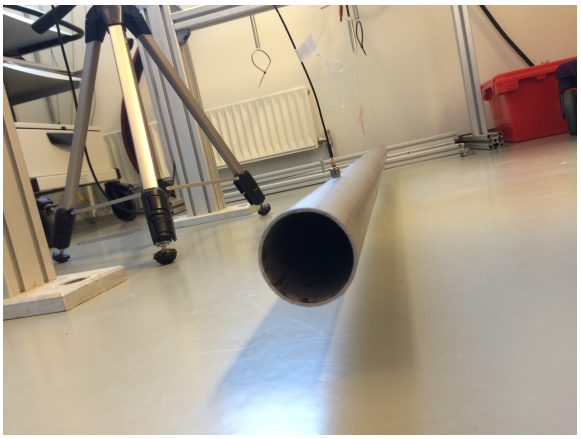

Figure D.4. Experiments for the thick shell is conducted in a standard room - no artificial acoustic damping material present.

As seen from the figures above the experiments on the thick shell are conducted in a standard room as the reflected acoustic is not sufficient to affect the structural response of the shell. Furthermore the accelerometers are attached gradually to control the effects of mass loading which is nonetheless found to be negligible.

Placements on thin shell

For the thin shell on the other hand no simplifications are adopted and as it satisfies the assumptions of the vibro-acoustic model the measurements need to be decomposed into modal response. This can be done by conducting multiple measurements at one or more cross sections of the shell and utilize a Fourier series representation to decompose the response. For this modal decomposition there exists several recognized and well-documented methods and through these experiments three different methods are compared to verify which method causes least modal leakage as this is suspected to be of major influence of on the quality of the inverse source characterisation and modal validation in general. These methods are elaborated in section 4.2.

For this thin shell quite a lot of experiments has been conducted for the purpose of having a wide range different cases that can be used as possible trials for the ISC method and similarly to ensure that at all modes are excited and measured at either the same or at different measurements. In figure D.5 the different placements of the accelerometers are indicated by gray rectangles and excitations points by gray semi-ellipsoids. Notice here that not all accelerometers are placed at these location at the same time and similarly that for different sequences of accelerometer placements not all excitations points are excited. In the figure all excitation points are indicated, however, all measurements may not necessarily be facilitated throughout the report due to lag of quality, modes not excited properly or simply because it is found insufficient to conclude on similar thing for other cases.

The dimensions associated with figure D.5 are shown in table D.3 with the excitations points excluded for simplicity. Whenever specific data from a specific excitation point are discussed or presented the co-ordinates to the associated excitation points are given.

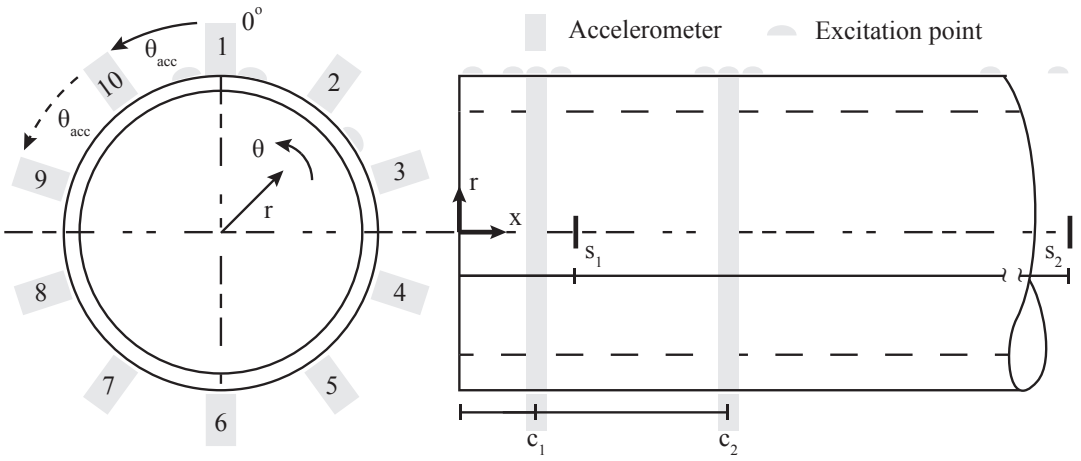

Figure D.5. Sketch of the placement of accelerometers, suspension points and cross section of interest for the thin shell.

As for the thick shell one experiment for the thin shell is also conducted with the scope of locating the flexural modes. The experimental set-up for this cases is identical to that for the thick shell, however with 10 accelerometers attached on the straight line. The location of the accelerometers are likewise indicated by a and are shown in table D.3.

	Unit	c_1	c_2	s_1	s_2	θ_{acc}
Thin shell Modal decomp.	mm	73.4	333	128	627	36°

	Unit	a_1	a_2	a_3	a_4	a_5	a_6	a_7	a_8	a_9	a_{10}
Thin shell Flexural mode	mm	22	100	177	255	333	410	488	565	643	721

Table D.3. Dimensions for accelerometers, suspension points and cross sections of the thin shell at the different experiments.

As for the thick shell the actual experimental set-up for the thin shell can be verified in figure D.6 and D.7. For further documentation on the set-up the attention is once again drawn to appendix A.4.

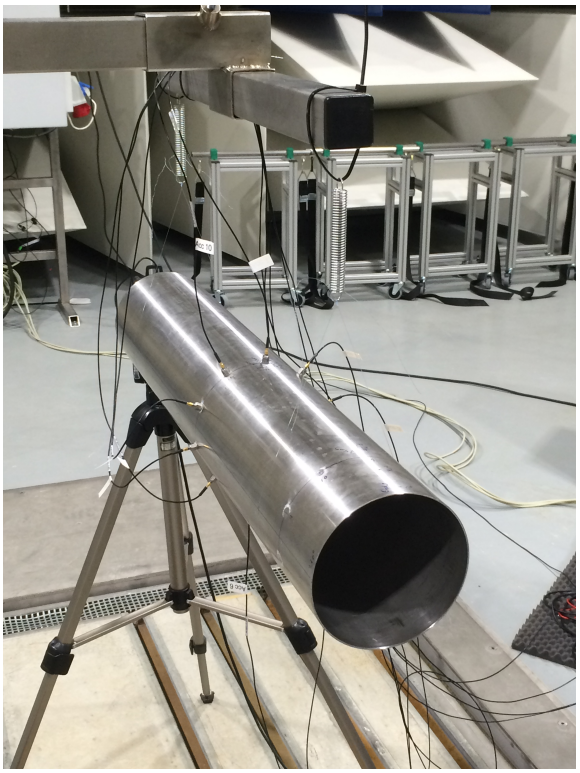

Figure D.6. Experimental set-up for the thin shell in the sound room. As seen all 10 accelerometers are placed in the circumference at the second cross section, c_2.

Figure D.7. Experimental set-up for all 10 accelerometers placed in the circumference at the first cross section, c_1, with accelerometer 1 placed on the inner radii.

From these figures it is seen that the experiments in this case are conducted in a sound room where the reflected waves are indeed at a minimum. This has been chosen to eliminate possible sources of error if the acoustic reflections should affect the structural response when the shell is thin. However, it is neither expected to be an issue for the thin shell.

Galerkin's orthogonalisation in modal decomposition

E

Through this appendix the different Galerkin orthogonalisation have been adopted to the different cases presented in section 4.5.2 and the derivation of these are shown here.

E.1 Cosine distribution

$$\vartheta^{\cos} = \sum_{n=0}^{\infty} \vartheta_n \cos(n\theta) \tag{E.1}$$

where $^{\cos}$ indicates that the function is dispersed by a **cos**ine.

Cosine orthogonalisation
To apply the Galerkin weighting the source distribution are to be known explicitly as the Galerkin orthogonalisation states that the weighting must be conducted with a function of similar shape. In equation (E.2) the orthogonalisation is conducted with a cosine simply by multiplying both sides of (E.1) with the weighting and averaging across the domain by means of an integral. In the discrete domain this considered the integral can be reformulated to e.g. a trapezoidal summation.

$$\int_0^{2\pi} \vartheta^{\cos} \cos(m\theta)\mathrm{d}\theta = \int_0^{2\pi} \sum_{n=0}^{\infty} \vartheta_n^c \cos(n\theta)\cos(m\theta)\mathrm{d}\theta \tag{E.2}$$

where ^{c} indicates that the orthogonalisation is done with a **c**osine function.

Finally, we apply the orthogonality properties of the trigonometric functions and arrive at the decomposed amplitudes

$$\int_0^{2\pi} \vartheta^{\cos} \cos(m\theta)\mathrm{d}\theta = \varepsilon_m^c \pi \vartheta_n^c$$

$$\Downarrow$$

$$\vartheta_m^c = \frac{1}{\varepsilon_m^c \pi} \int_0^{2\pi} \vartheta^{\cos} \cos(m\theta)\mathrm{d}\theta$$

where $\varepsilon_{m=0}^c = 2$ and $\varepsilon_{m\neq 0}^c = 1$.

Exponential orthogonalisation
For orthogonalisation with an exponential function the procedure is completely analogue to that of a cosine and the decomposed amplitudes terminates at

$$\vartheta_m^e = \frac{1}{\varepsilon_m^c \pi} \int_0^{2\pi} \vartheta^{\cos} \exp(-im\theta)\mathrm{d}\theta$$

Notice that confer to Galerkin's orthogonalisation for the exponential function it should be conducted with the complex conjugated as seen in the equation.

E.2 Sine distribution

$$\vartheta^{\sin} = \sum_{n=0}^{\infty} \vartheta_n \sin(n\theta) \tag{E.3}$$

Sine orthogonalisation

$$\vartheta_m^s = \frac{1}{\pi} \int_0^{2\pi} \vartheta^{\sin} \sin(m\theta) \mathrm{d}\theta$$

Exponential orthogonalisation

$$\vartheta_m^{\pm e} = \mp i \frac{\varepsilon_m^s}{\pi} \int_0^{2\pi} \vartheta^{\sin} \exp(\pm im\theta) \mathrm{d}\theta$$

where $\varepsilon_{m=0}^s = 0$ and $\varepsilon_{m\neq 0}^s = 1$.

E.3 Exponential distribution

$$\vartheta^{\exp} = \sum_{n=0}^{\infty} \vartheta_n \exp(n\theta) \tag{E.4}$$

Sine orthogonalisation

$$\vartheta_m^s = -i \frac{1}{\pi} \int_0^{2\pi} \vartheta^{\exp} \sin(m\theta) \mathrm{d}\theta$$

Cosine orthogonalisation

$$\vartheta_m^c = \frac{1}{\varepsilon_m^c \pi} \int_0^{2\pi} \vartheta^{\exp} \cos(m\theta) \mathrm{d}\theta$$

Exponential orthogonalisation

$$\vartheta_m^e = \frac{1}{2\pi} \int_0^{2\pi} \vartheta^{\exp} \exp(-im\theta) \mathrm{d}\theta$$